

EDITORIAL BOARD

Editor-in-Chief

V.P. Melnikov, Full Member of Russian Academy of Sciences

Associate chief editor

V.M. Kotlyakov, Full Member of Russian Academy of Sciences

Executive secretary

V.E. Tumskoy

Editors:

J. Brown, professor (USA); *A.V. Brouchkov*, professor; *A.A. Vasiliev*; *P. Williams*, professor (UK); *M.L. Vladov*, professor; *M.N. Grigoriev*; *D.S. Drozdov*, professor; *V.A. Istomin*, professor; *M.V. Kirov*; *I.N. Modin*, professor; *A.N. Nesterov*; *E.-M. Pfeiffer*, professor (Germany); *V.E. Romanovsky*, professor (USA); *G.L. Stenchikov*, professor (Saudi Arabia); *K. Flaate*, professor (Norway); *S. Harris*, professor (Canada); *H. Hubberten*, professor (Germany); *N.I. Shiklomanov*, professor (USA); *Yu.L. Shur*, professor (USA); *I.N. Esau*, professor (Norway)

Councilors:

V.R. Alekseev, professor; *F.E. Are*, professor; *A.D. Duchkov*, professor; *M.N. Zheleznyak*; *Yu.D. Zykov*, professor; *N.S. Kasimov*, Full Member of RAS; *I.A. Komarov*, professor; *F.M. Rivkin*; *E.M. Rivkina*; *E.A. Slagoda*; *A.V. Soromotin*; *V.T. Trofimov*, professor; *L.N. Khrustalev*, professor; *V.G. Cheverev*; *G.A. Cherkashev*

Editorial Office of *Earth's Cryosphere (Kriosfera Zemli)*
Institute of Geography, Russian Academy of Sciences
37 Vavilov str., office 22, Moscow, 117312, Russia
Editorial staff: *N.V. Arutyunyan*, *N.G. Belova*, *O.M. Lisitsyna*, *G.E. Oblogov*
Phone: 8(985) 957-10-01, e-mail: kriozem@gmail.com

Journal promoted by

Russian Academy of Sciences, Siberian Branch, Novosibirsk
Earth's Cryosphere Institute, Tyumen Scientific Centre SB RAS, Tyumen
Melnikov Permafrost Institute, SB RAS, Yakutsk

Editorial Manager *M.A. Trashkeeva*

Designed by *N.F. Suranova*

Typeset by *N.M. Raizvikh*

EARTH'S CRYOSPHERE
SCIENTIFIC JOURNAL

Founded in January 1997	6 issues per year	Vol. XXV, No. 5	September–October 2021
----------------------------	----------------------	-----------------	---------------------------

CONTENTS

FUNDAMENTAL ISSUES OF EARTH'S CRYOSPHERE

- Cheverev V.G., Brushkov A.V., Polovkov S.A., Pokrovskay E.A., Safronov E.V.** Analysis of concepts on the mechanism of cryogenic migration of water in freezing ground. 3

GEOHERMAL FIELDS AND THERMAL PROCESSES IN CRYOSPHERE

- Svetlakov A.A., Kozyreva E.A., Sergeev D.O.** Soil temperature in the contemporary natural-climatic situation of the steppe Baikal region (on the example of Olkhon Island) 11

CRYOGENIC PHENOMENA IN SEAS AND OCEANS

- Selyuzhenok V.V.** Interannual variations of maximal fast ice extent in the East Siberian Sea 19

SNOW COVER AND GLACIERS

- Rets E.P., Petrakov D.A., Belozarov E.V., Shpuntova A.M.** Mass balance modelling for the Sary-Tor glacier (the Ak-Shyrak massif, Inner Tien Shan) 23

CRYOSPHERE RESEARCH METHODS

- Elsakov V.V., Kaverin D.A., Shchanov V.M.** The study of seasonal vertical changes of ground surface in the Polar Ural foothills based on field measurements and ALOS PALSAR radar interferometry 36
- Edemskiy D.E., Tumskoy V.E., Ovsyuchenko A.N.** Ground-penetrating radar sounding of deposits within the limits of high-centered polygons in the Arctic 47

FUNDAMENTAL ISSUES OF EARTH'S CRYOSPHERE

ANALYSIS OF CONCEPTS ON THE MECHANISM
OF CRYOGENIC MIGRATION OF WATER IN FREEZING GROUNDV.G. Cheverev¹, A.V. Brushkov¹, S.A. Polovkov², E.A. Pokrovskay², E.V. Safronov¹¹ *Lomonosov Moscow State University, Faculty of Geology, Department of Geocryology, Leninskie Gory 1, Moscow, 119991, Russia; cheverev44@mail.ru*² *Scientific Research Institute of Pipeline Transport (Transneft Research Institute, LLC), Center for Monitoring and Geoinformation Systems of Pipeline Transport Facilities, Sevastopolsky pr. 47a, Moscow, 117186, Russia; PolovkovSA@nitnn.transneft.ru*

A retrospective analysis of the results of studies of the mechanism of water migration in freezing soils was carried out on the basis of an analysis of about 160 scientific publications by Russian and 100 foreign authors. For the analysis, articles, monographs, dissertations, patents, conference proceedings and scientific reports were used. The main ones are given in the list of references. Special attention is paid to the key aspects of the formation of understanding of the driving forces of cryogenic migration (moisture transfer) in freezing soils. This analysis is necessary for the correct physical formulation of the mathematical model of the process of frost heaving of soils.

Keywords: *analytical review, mechanism of cryogenic migration, frost heaving of soils.*

INTRODUCTION

Frost heaving of soils is widespread in the area of seasonal and long-term freezing in the cold regions of the Earth and is a dangerous cryogenic process for buildings and constructions. For this reason, the study of the physical nature of heaving and the development of mathematical models adequate to the physical essence of the process, methods of its prediction and management is an urgent scientific and practical problem.

In general, the mechanism of frost heaving of soils is a complex interaction and interdependence of heat transfer, mass transfer, phase transitions of water in the pores of the soil, segregation of ice and the dynamics of its stress-strain state. Heat transfer as the root cause ensures the removal of phase transition heat, capacitive and convective heat from the freezing soil. By freezing the soil, the heat transfer initiates mass transfer and segregation of ice in soils prone to frost heaving.

The dynamics of the stress-strain state of the freezing soil depends on three factors. Firstly, on the expansion of water in the pores of the frozen zone of the soil during its transition to ice *in situ* with the appearance in cramped conditions of significant solidification forces at small deformations of heaving. Secondly, due to the significant inflow of water from the melt layer of the soil into the freezing one via cryogenic migration, during freezing, this gives the main contribution to the heaving of the soil. Thirdly, the outflow of water from the melt zone into the freezing one lowers the pore pressure in it, causing shrinkage, which reduces the overall deformation of the frost heaving of the soil.

Heat transfer and cryogenic migration, in turn, are accompanied by segregation ice-separation in the form of a special layered cryogenic structure, which leads to anisotropy of the building properties of frozen soils and significant draft of the constructions during the thawing.

The analysis of the state of the study of these processes is directly related to the physical formulation of the problem of mathematical prediction of freezing and heaving of soils, taking into account the processes of heat and mass transfer, segregation of ice, deformation and forces of heaving of soils. The results of theoretical and experimental studies obtained by specialists of Lomonosov Moscow State University and The Transneft Research Institute on the problem of frosty soil heaving is a test numerical mathematical model. The presentation of these results are distributed over a number of articles. This paper briefly summarizes only the ideas about the mechanism of cryogenic migration and frost heaving of soils that are of paramount importance for the development of a mathematical model.

DRIVING FORCE
OF CRYOGENIC MIGRATION

A very significant number of works have been devoted to the development of ideas about the nature of migration processes in freezing dispersed soils and their frost heaving, there are already several hundreds of them. In the last 10–20 years, a number of other articles have appeared, but they mainly have applied character. The analysis of published works is available in a number of review articles, dissertation chapters and monographs [*Sumgin, 1929; Beskow,*

1935; Edlefsen, Anderson, 1943; Goldstein, 1948; Bazhenova, Bakulin, 1957; Orlov, 1962; Tsytoich, 1973; Brovka, 1991; Black, 1995; Cheverev et al., 1998; Cheverev, 2003a, 2004].

Nevertheless, due to the appearance of new theoretical and experimental results, including those belonging to the authors of the article, new generalizations become relevant. This allows us to hope for a significant development of the existing ideas about the heaving process and the solution of the problems of creating an adequate mathematical modeling of the freezing process of fine-grained soils in terms of physical formulation and taking into account heat and mass transfer, heaving, shrinkage and segregation of ice.

Back at the end of the XIX century, the need to find out the cause of frost heaving of soils and on this basis, new developments of means of protecting engineering structures from this dangerous process became acute in connection with the construction of roads in the districts of the Siberia and the Russian Far East. The researchers noted a significant increase in the water content (ice content) of the freezing soil and its heaving. So, G.Ya. Bliznin in his work gave data on an increase in water content in the upper horizons of the soil in winter. He suggested the possibility of transferring pore water in freezing soils *under the influence of thermal gradient*, which was logically based on general considerations [Bliznin, 1890].

In the works of our predecessors several basic theories (hypotheses) have been suggested for the clarification of the formation of the driving forces of the cryogenic migration of water and the frost heaving of soils. These theories include *capillary (meniscus) force, head pressure, compressional compaction, crystallization of water, the forces of surface adsorption, vacuum, potential double electric layer (osmosis), gradient of the thermodynamic potential*. All of them will be discussed below.

Capillary forces. The works of Russian engineers-trackmen V.I. Shtukenberg [1894] and S.G. Voislav [Cvigunov, 2018] should be attributed to the first studies of the physical essence of the process of frost heaving of soils. They laid the basic theoretic

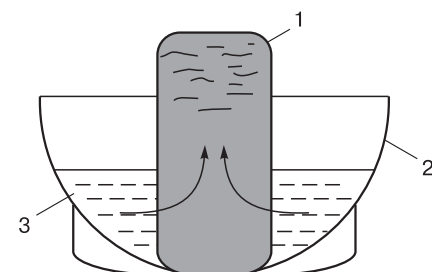


Fig. 1. Scheme of the experiment: a soil sample freezing in the frost [Cvigunov, 2018].

1 – soil sample; 2 – bowl; 3 – water.

cal prerequisites for studying the physical essence of the processes of heaving and migration of water in freezing soils.

In Fig. 1, there is a diagram of a simple experiment of S.G. Voislav, from which it follows that a sample of thawed soil placed in the frost in a bowl with water, froze with an increase in volume and the formation of ice layers. At the same time, the amount of water in the bowl decreased proportionally. As a result of the experiment, the author came to the conclusion that the deformations of the frost heaving of soils were caused by the absorption of water from the thawed layer of soil into the freezing one and the formation of ice layers from this water.

V.I. Shtukenberg put forward a physical explanation of the causes of soil heaving in the ground embankment of the railway track *by the influence of water migration in the liquid phase from the lower to the upper freezing layers* of the ground embankment. He also proposed an approximate mathematical description of the process of soil heaving. *Capillary hypothesis* of V.I. Shtukenberg [1894] was one of the first hypotheses of water migration during freezing and heaving of soils.

In 1929 and 1930, S. Teber carried out a series of laboratory experiments on freezing samples of kaolinite clay and obtained the results that became classic. Most authors have referred to these experimental works up to the present time. In Fig. 2 it is shown, as

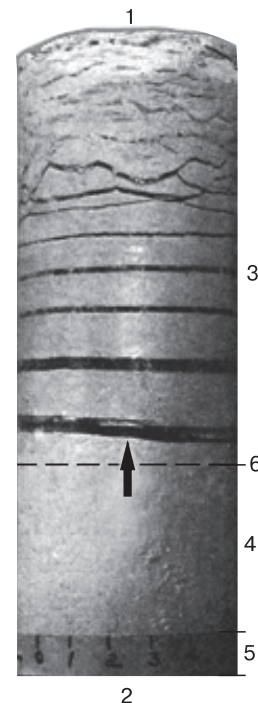


Fig. 2. Photo of a freezing sample of kaolinite clay.

1 – cold end face; 2 – warm end face; 3 – frozen layer; 4 – thawed layer; 5 – water-saturated sand layer; 6 – freezing front; *arrow* – direction of cryogenic migration [Taber, 1930].

a clear example, the result of the formation of cryostructure in a freezing kaolinite clay sample with water inflow from the outside, from the side of the warm end face of the sample. As can be seen in Fig. 2, a horizontal-wavy micro-lenticular cryostructure had firstly formed from the cold end face of the sample, and then gradually, under the influence of a decrease in the freezing rate, it has been becoming the lenticular and the sparser one. S. Teber also proposed a probable mechanism for the growth of ice lens in freezing soil based on *capillary suction* [Taber, 1930].

The capillary hypothesis has not been further confirmed. The facts of the occurrence of capillary menisci during the crystallization of water in the soil have not been obtained subsequently. The soils with full water saturation are devoid of menisci due to the absence of a water–air phase boundary. At the same time, it is known that fully water-saturated soils are the heaviest ones. Moreover, the definition “the capillary mechanism of frost heaving”, as will be revealed below, ignores the undeniable surface and osmotic forces involved in the formation of heaving.

At the same time, this does not mean that capillaries in the soil do not play a significant role in frost heaving. On the contrary, they are the medium in which the pore solution transits from the thawed to the freezing zone of the soil under the action of a pore pressure gradient initiated by the negative thermal gradient of the freezing zone [Beskow, 1935].

Pressure forces. The assumption of the water transfer under the action of “pressure forces” arising due to an increase in the specific volume of water during its transition to ice was developed in [Nikiforov, 1912; Dranitsyn, 1914; Sumgin, 1929]. According to the “theory of pressure migration”, the water transfer in the pores of the freezing soil takes place under the influence of pressure occurring during the freezing of water (which leaks down along a weakly permeable horizon) or during the freezing of a layer closed between the underlying frozen stratum and the layer of winter freezing. Further studies have revealed that the theory of pressure forces explains quite well the formation of injection frost mounds (pingo) and therefore is a special case of non-segregation heaving.

Compression compaction. V.O. Orlov [1962] assumed the presence of a compressional compaction process of the thawed layer of the freezing soil due to pressure from the weight of the overlying frozen layer, considering this to be the cause of the flow of pore water from the thawed into the freezing layer. However, this hypothesis has not been supported by experimental data. The thawed layer is compacted by the negative pore pressure occurring due to the outflow of water into the freezing layer.

Under certain conditions, the pressure of the frozen layer or of the load from the construction on the thawed layer of the freezing soil affects its heaving, but this is a second-level factor, and it is not the root

cause of cryogenic migration and heaving. On the contrary, in the conditions of an open mass transfer system the significant external load, as a rule, complicates the penetration of cryogenic migration into the freezing layer and at critical pressure stops it completely. Without a load on the freezing soil in its thawing zone, a negative pore pressure ($-P_w$) is formed due to the outflow of pore solution into the freezing zone. Pressure is measured on a relative scale, where the atmospheric pressure is taken as zero, and the compression pressure is taken as positive ($+P_w$).

The formation of segregation layers of ice, in general, is not associated with the pressure forces of the pore solution. But there may be a special case when under the unconsolidated compaction the thawed layer undergoes an external load. As a result, the negative pore pressure decreases towards neutral and can even turn into positive one, thereby accelerating the cryogenic migration and increasing the heaving of the freezing soil. This fact was first established experimentally and published in the work [Cheverev et al., 2013].

The forces of water crystallization. Along with the capillary theory, S. Teber proposed a *theory of cryogenic migration due to the forces of ice crystallization*, which, like the capillary hypothesis, proved untenable. By the forces of crystallization, he assumed the ability of ice crystals to attract water from the underlying horizons. S. Teber wrote: “The growing ice crystal is enveloped by a thin film of water similar to adsorbed water formed on many other solids coming into contact with water. When a molecule in the film moves in the direction of the ice crystal and joins it, it is replaced by another water molecule, as a result the integrity of the film is preserved” [Taber, 1930].

In the course of further researches the validity of the theory of ice crystallization forces has not been confirmed. Experiments carried out by the authors of [Bazhenova, Bakulin, 1957] have demonstrated that the hydrophobization of the mineral component of the soil, which eliminates the meniscal forces, stops its heaving due to cryogenic migration – although the phase transition of water into ice occurs in the pores of the soil, but the water freezes in place. At the same time, the reverse process – the squeezing of water from the freezing front – is possible and is realized at the favorable combination of the freezing rate and resistance to the flow of the pore solution from the front of the freezing into the thawed zone.

Surface adsorption forces. Influenced by the works of S. Teber, G. Beskow put forward *the theory of adsorption forces of the mineral component of the soil* [Beskow, 1935]. In this theory, for the first time, the idea was expressed that the film migration to the front of freezing is associated with freezing of the outer part of water films adsorbed by the mineral particles and soil aggregates. As for the effect on film water, G. Beskow considered the crystallization process

of this part of the water to be similar to the evaporation process.

Here it is appropriate to recall the results of the study of water transfer in unfrozen soils from the work [Lebedev, 1919].

The decrease of the amount of water molecules in the film due to its gradual crystallization contributes to the corresponding release of part of the surface energy of the mineral component of the soil, which causes and supports the migration of water to the freezing front. At the same time, A.F. Lebedev has rightly believed that the capillary water in the thawed zone is a source of loss of film water in the frozen zone, and the capillaries themselves are the ways of migration.

The theory of adsorption forces of the mineral component of the soil was the right direction in the development of ideas about the mechanism of cryogenic migration and heaving of soils, but not its completion. For example, this theory has not yet explained why sand are not heaving as clay and silt, although their hydraulic conductivity is higher by orders of magnitude; also, the role of a double electric layer on mineral particles in this process has not been considered.

Thus, this theory has needed further development in terms of taking into account the physico-chemical nature of the adsorption of water and ions on a solid mineral surface.

Vacuum. V.E. Borozinets and G.M. Feldman have proposed a vacuum filtration mechanism for the formation of thick ice lens. They consider that the growth of thick ice lenses occurs with periodic temperature fluctuations on the surface of the earth, which initiates the reciprocating movement of the freezing front in the soil at a certain depth. In the freezing cycle, the ice formation produces the soil

heaving, and in the thawing cycle, the internal volume of the soil decreases. As a result of thawing, the local volumes with low pressure are formed, into which the water rushes from the lower zone of the soil. Further, this additional volume of water freezes, increasing the thickness of the ice layer, and so a thick layer of ice grows [Borozinets, Feldman, 1981]. In fact, the authors have suggested a mechanism for the formation of the driving force of cryogenic migration during cyclic freezing-thawing at the local level due to the fluctuations in the internal pore hydraulic pressure.

The existence of such a mechanism when the temperature fluctuates on the surface of the soil causes doubts since the reciprocating process, which is considered by the authors, is reversible (defrosting is changed by freezing), and the decrease in pressure during the thawing is replaced by its increase during freezing, therefore, the inflow is replaced by the outflow in the same volume, other things being equal.

However, the fact of the formation of the increased iciness and the thick ice lens has been established in the top of permafrost, and there is another explanation for this fact. It has been experimentally established that during the gradual thawing of frozen soil the conditions for ice segregation are preserved in its frozen layer. The accumulated ice is preserved during the subsequent freezing, and its growth resumes in the next thawing-freezing cycle [Ershov et al., 1976].

The potential of a double electric layer on the surface of mineral particles (osmosis). Theoretical and experimental studies have proved that the leading role in the mechanism of cryogenic migration and heaving of freezing soils is played by a double electric layer (DEL) of ions in the water environment on the surface of the mineral clay particles, as well as the existence of a diffuse ion layer in DEL.

M.N. Goldstein, L. Cass and R.D. Miller have suggested to evaluate the role of the basic properties of DEL on the surface of mineral particles in cryogenic migration [Goldstein, 1948; Cass, Miller, 1959].

The theory of DEL has been developed since the middle of XIX century regardless of the frost heaving of soils. It made it possible to explain such interesting physical-chemical effects and phenomena as electro-osmosis, electrophoresis, direct and reverse osmosis, properties of colloidal systems, etc. [Shchukin et al., 2004].

This theory is based on the concept of the German physicist Otto Stern (1924). In this theory he has combined the theory of Helmholtz–Perrin (1878) and the Gouy–Chapman (1910) (Fig. 3). According to these ideas, at the boundary of the contacting phases on solid hydrophilic surface there are the atoms of the crystal lattice with uncompensated charges, the so-called layer of potential-determining ions (PDI), and the electrostatically adjacent layer of

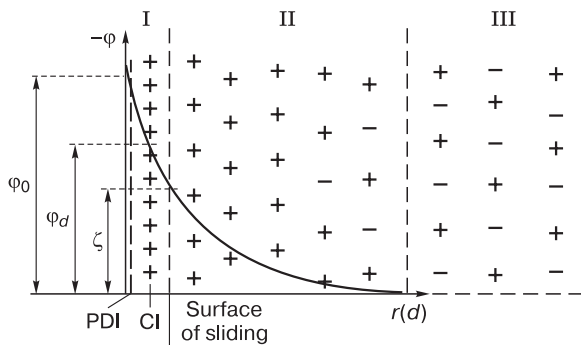


Fig. 3. The electric double layer (by Stern) and the potential change in it (φ):

I – adsorption layer; II – diffuse layer; III – volume solution; PDI – layer of potential-determining ions of mineral surface; CI – a layer of counter ions; φ_0 – thermodynamic adsorption potential; φ_d – diffusion potential, ζ – electrokinetic potential of diffuse layer of ions on the surface of sliding; $r(d)$ – radius (thickness).

counterion (CI) from aqueous solution. The layer of counterions consists of two parts. One part is directly adjacent to the interfacial surface and forms an adsorption layer (Helmholtz layer) with a thickness equal to the diameter of the hydrated ions that make it up. The other part of the CI DEL is located at a certain distance and is called the diffuse layer of counterions (Gouy layer). With increasing distance, the gravity of the counterions to the PDI layer decreases, the concentration of counterions gradually decreases from the maximum value to the average concentration in a neutral solution. At the same time, the ratio of the OC ions (that are in direct proximity to the PDI) to the diffuse layer ions on average constitutes 95:5 % of the total amount, respectively.

An electric field operates within the DEL, the intensity of which is characterized by a certain value of the potential. In Fig. 3 several types of the changes in the DEL potential with the increase of the distance from the surface are demonstrated.

- The thermodynamic potential of the surface (φ_0) is a complete potential jump between the mineral surface and any point in the deepness of the solution where the influence of the surface does not affect.

- The potential of the diffuse layer (φ_d) is the potential arising at the boundary between the adsorption and diffuse layers. In the adsorption layer, the DEL-potential decreases linearly.

- Electrokinetic potential on the sliding surface, or ζ -potential. This potential arises under the action of external forces on the sliding surface. It is maximal at the outer boundary of the adsorption layer and decreases exponentially along with moving into the diffuse layer.

There is reason to believe that the ζ -potential determines the maximum value of the cryogenic migration potential, so let's consider its properties in more details.

The value of the ζ -potential is affected by the thickness of the diffuse layer. The smaller the thickness the lower is the ζ -potential, up to the zero value (when the cryogenic migration stops). In turn, the thickness of the diffuse layer is influenced by various factors. Thus, with the change of concentration of the external solution (which is not included in the DEL) its equilibrium with the diffuse layer is disturbed, because they compete for a coupling with water molecules. In the case of extreme compression, the diffuse layer degenerates and its ions pass into the adsorption layer. Consequently, the effect of compression of the diffuse layer with an increase in soil salinity leads to the cessation of cryogenic migration and heaving. Figure 4 shows the dependence of the cryogenic migration flow on the concentration of the pore solution of the freezing silt clay. When it is increased to 1 N (N is the normality of the solution, it denotes the number of gram equivalents of this substance in one liter of solution or the number of milligram equiva-

lents in one milliliter of solution) the cryogenic migration stops, which indicates the ultimate compression of the diffuse ion layer.

However, at the solution concentration of 0.01 N, the migration flow is maximal, since the ζ -potential of the diffuse layer of ions (at their optimal content) is maximal. At the same time, in ultra-fresh clay (the normal concentration (C) is approximately equal to 0 N), the migration flow is only half of the maximum, which is explained by a significant decrease in the thickness and the ζ -potential of the diffuse layer due to its erosion in the ultra-fresh state. At that, a certain amount of exchange ions is always present in the diffuse layer, as the water is the very good solvent.

It should be taken into account that the ζ -potential of the diffuse layer is not a constant value and depends on the radius, the valence and the charge of the ions, as well as on the chemical nature of the solid phase surface, the temperature, the composition and the concentration of ions of the competing bulk solution.

The leading role of DEL in the formation of frost heaving of the soil can be defined as the existence of a semi-permeable soil layer, which initiates the flow of cryogenic migration from a warm zone to a cold one during freezing, where water freezes in the plastically frozen zone of the freezing soil as thermodynamically excessive and causes deformations and heaving forces. Here, obviously, one can find an analogy with the method of measuring osmotic pressure with a semi-permeable membrane.

The ion-molecular theory of the double electric layer (developed in the field of physical chemistry) can be used to predict and control the frost heaving of freezing soils at a qualitative level. The object for this is the ζ -potential of the diffuse ion layer. Since the diffuse ion layer accumulates the main volume of

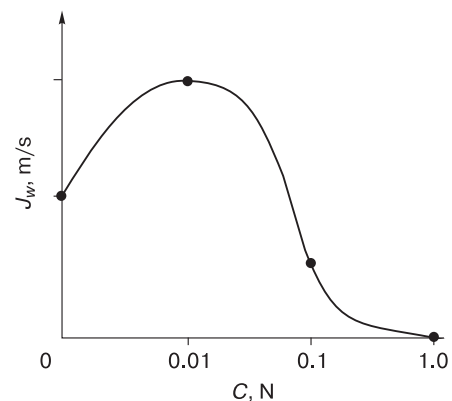


Fig. 4. The character of the effect of the normal concentration (C) of a pore solution of sodium chloride of freezing silty clay on the flow rate of cryogenic water migration (J_w) [Cheverev, 2004, p. 138].

bound water (up to 95 % DEL), then it is possible to control the frost heaving by acting on its ζ -potential (Fig. 3). For example, a change in the chemical composition and concentration of the pore solution changes the value of the ζ -potential and the thickness of the diffuse ion layer. This, in turn, affects the intensity of cryogenic migration and the frost heaving of the freezing soil.

Due to the complexity of the clay soil (polyminerality, polydispersity, heteroporosity, multiphase), the quantitative forecast of frost heaving based on the theory of DEL is not yet seemed possible.

At the same time, the phenomenological model formulated at the macroscopic level can be successfully constructed for frost-sensitive soils and will allow a reliable quantitative forecast. Therefore, the main efforts in the development of numerical modeling of the freezing and heaving of soils forecast are currently aimed at using the basics of thermo-dynamics of irreversible processes and phenomenological laws.

Thermodynamic potential of water in the soil.

It is known that the water in the soil obeys the general trend and flows from places with higher potential energy to places with lower potential energy, which is also valid for freezing of heaving soil.

The method based on the use of partial, or free, specific energy of J.V. Gibbs (*the chemical potential of water*) is used to assess the energy state of water in soils. Since the chemical potential characterizes the state of the component in the absence of external force fields, and the water in the soil is yet under their influence, then the chemical potential of water in the soil has received the special name *thermodynamic potential of water* [Thermodynamics..., 1966].

Chemical potentials of water in the SI system are represented in the dimension of work – kJ/kg (or J/mol). However, for the convenience of a quantitative description of the water transfer process in freezing, thawing and frozen soils, it can be represented in the dimension of the equivalent pressure – Pa (or kg/cm², atm, more convenient in *meters of water column*, 1 m of water = 10⁴ Pa). Based on equality $-\mu_w$ [kJ/kg] = $-P_w/\rho_w$ [m³·kg/(m²·10³ kg)], where ρ_w is the density of water, expressing weight in terms of mass ($F = mg$), we get [m³·kg·m/(m²·10³ kg·s²)]. Taking into account the fact that kJ = m²·kg (mass)/s², we come back to the dimension [kJ/kg] with a coefficient of 0.981, i.e. 1 MPa = 0.981 kJ/kg [Cheverev, 2004].

At the same time, the pressure in the pore solution formed by external energy impact (hydrostatic pressure, suction, compression, etc.), in contrast to the equivalent pressure, is considered simply pore pressure and is denoted $-P_w$. The negative pore pressure in cryogenic soils is not measured in vacuum units, as it is customary in atmospheric physics (from

0 to 1 atm). It is measured in the scale adopted in agrophysics, when the normal atmospheric pressure in pure volumetric water (which is outside the influence of the soil) is equated to zero as neutral.

Hydrostatic and compression-filtration pressures in the soil have positive values ($+P_w$), and the suction pressure and all the components of the chemical potential, when converted to equivalent pressure, have negative values ($-P_w$).

Thus, when studying the energy state of water and the driving forces of water transfer in cryogenic soils, it is necessary to differentiate between the chemical potential of water (μ_w), directly determined by the hydrophilic ability of the soil, and the potential of water as a function of the process itself and external conditions.

When a part of water freezes, the amount of liquid phase decreases, and the remaining part of it is under lower pressure (or higher binding energy) compared to free water. Hence $dP_w/dT < 0$. At the same time, ice crystals having no hydraulic connection with water are free from the pressure existing in the liquid phase. The pressure acting on the crystals no longer depends on T , and, consequently, $dP_i/dT = 0$.

Considering this, we use the Clapeyron–Clausius thermodynamic equation for one-component two-phase ice–water system, which has the form

$$dP/dT = L/(T_0(V_2 - V_1)), \quad (1)$$

where L is the specific heat of the phase transition from the first phase to the second one; $(V_2 - V_1)$ – the difference of specific volume of phases; T_0 is the temperature of the water phase transition at atmospheric pressure on the Kelvin scale.

Modified equation (1) for conditions of water energetic state in soils by N.E. Edlefsen and A.B.C. Anderson, takes the form [Thermodynamics..., 1966; Cheverev, 2003b]:

$$dP_w = DT/(T_0V_w), \quad (2)$$

where V_w is the specific volume of the liquid phase of water.

The validity of using such an approach to frozen and freezing soil was experimentally and analytically confirmed by V.G. Cheverev and co-authors. After substituting the values of T_0 , and L and V_w (as for free water, which is acceptable) we get that an increase in pressure on liquid water by 0.1 MPa leads to an increase in the freezing temperature by 0.0824 K. At that, the expression [Cheverev et al., 1998; Cheverev, 2003a,b] is true:

$$dP_w/dT = -1.2 \text{ MPa/K} = 120 \text{ m of water/K.} \quad (3)$$

Hence, according to S.N. Buldovich and V.G. Cheverev, the equation for calculating the density of the flow of unfrozen water in frozen soil (I_{wm})

under the action of a thermal gradient (dT/dz) has the form [Ershov, 1999]

$$I_{wm} = -\lambda_{wm}(T)kDT/dz, \quad (4)$$

where $\lambda_{wm}(T)$ is the coefficient of water conductivity of the frozen soil, which significantly depends on the type of soil and its temperature, m/s; k is the proportionality coefficient, m of water column, equal to 120 m/K; z is the height of the frozen zone, m.

The thermal gradient in the freezing zone of the soil (more precisely at the freezing front) initiates the gradient of hydraulic pore pressure and water flow in the thaw zone (I_{wt}), for which, the following equation is valid according to S.N. Buldovich and V.G. Cheverev [Ershov, 1999]:

$$I_{wt} = -\lambda_{wt}k(T_{bf} - T_{\xi})/(1 - \xi), \quad (5)$$

where λ_{wt} – coefficient of hydraulic conductivity of the unfrozen soil, which depends considerably on the type of soil, its density and water content, m/s; k – coefficient of proportionality, m of water column, equal to 120 m/K; T_{bf} – the freezing point of soil in the thawed zone (static characteristic); T_{ξ} is the temperature at the freezing front, depending on the type of soil and the dynamics of its freezing (dynamic characteristic): it decreases with an increase of the freezing rate and becomes equal to T_{tot} when the freezing front, cryogenic migration and heaving stop.

Equations (4) and (5), presented in potential form, are the basic ones for the development of a mathematical model of freezing and heaving of soil considering mass transfer.

CONCLUSIONS

Basing on the analytical review of a large volume of theoretical, model and experimental studies, the authors came to conclusions important for the development of the theory of cryogenic migration and frost heaving of soils. In the future, it is possible to improve the physical formulation of the mathematical model of the process of freezing and heaving of soils, taking into account heat and mass transfer.

In general, the process of frost heaving of freezing soil can be attributed to a new chapter of the scientific direction of physical-chemical mechanics of materials and colloidal systems, the founder of this system is academician P.A. Rebinder. The mechanism of cryogenic migration and frost heaving of soils is a complex interaction and interdependence of heat transfer, mass transfer, phase transitions of water in the pores of the soil, segregation of ice and the multidirectional dynamics of its stress-strain state. Heat transfer as the root cause ensures the removal of heat of phase transitions, of the capacitive and convective heat from the soil. By freezing the soil, heat transfer initiates mass transfer and ice segregation in heaving soils.

The article provides an overview of the development of ideas about the root cause of cryogenic migration of water in freezing soils and its driving forces, based on which the following conclusions are made.

1. The possibility of transferring pore water in freezing soils under the influence of a thermal gradient was first proposed by G.Ya. Bliznin [1890]. Attempts to find another explanation, independent of the thermal gradient, were unsuccessful.

2. V.I. Shtukenberg [1894] and S. Taber [Taber, 1930] proposed the capillary hypothesis as the first cause of water migration during freezing and heaving of the soil. However, this hypothesis has not been confirmed. The driving force of cryogenic migration occurs in the freezing zone of the soil, where the menisci of pore water do not form at the border with air, which is practically absent in heaving and water-saturated soils. However, the capillaries of the soil perform an important transit function for cryogenic migration.

3. The theories of pressure forces and compressive compaction of the soil have also not been confirmed, since as a result of the outflow of water from the thaw zone into the freezing zone, the negative pore pressure with shrinkage of the soil is formed under the front of the freezing, but not a positive one as it takes place during the compression compaction.

4. The theory of the forces of water crystallization during its transition to the ice phase has also not been confirmed. The main role of the adsorption forces of the mineral component was confirmed by the experiments of A.P. Bazhenova and F.G. Bakulina in 1957 on hydrophobization of the soil mineral matrix, after which the cryogenic migration and heaving stopped [Bazhenova, Bakulina, 1957].

5. The theory of the main role of surface adsorption forces of the mineral component of the soil in the process of cryogenic migration (put forward for thawed soils by A.F. Lebedev, and for frozen soils by G. Beskow) turned out to be significantly closer to the truth than the hypotheses considered above. The decrease of water molecules in the film due to its gradual crystallization contributes to the release of part of the surface energy of the mineral component of the soil, which causes and inhibits the migration of water to the freezing front. The theory of adsorption forces was the right direction, but this direction was far from completion. For the development of this theory it was necessary to take into account the physical chemistry of surface phenomena, namely, the double electric layer of ions according to Stern.

6. M.N. Goldstein [1948], L.C. Kass and R.D. Miller [Cass, Miller, 1959] assigned an essential role in cryogenic migration to osmotic properties of the diffusion of a double electric layer. More developed version of this theory is proposed in this article.

Due to the particular complexity of the composition of heaving (and, as a rule, clay) soils, the microscopic level of knowledge of the mechanism of cryogenic filtration does not imply in the foreseeable future the development of a numerical mathematical model of freezing of heaving soils on this basis. Therefore, in order to achieve a real practical result, it is necessary to move to the macroscopic, phenomenological level of development of the theory of frost heaving of soils. To achieve this goal, it is necessary to use the concept of thermodynamic potential of water.

7. The theory of cryogenic migration flow formation based on thermodynamic potential uses a modified equation Clapeyron–Clausius, thermodynamically substantiated by N.E. Edlefsen and A.B.C. Anderson [Edlefsen, Anderson, 1943] and experimentally and analytically confirmed and proved by V.G. Cheverev [Cheverev, 1998, 2003a].

Acknowledgments. *The materials for the preparation of the article were obtained with the financial support of Ltd “Research Institute of Transneft” (contract No. 4220 P/20-511/2015 dated 19.11.2015).*

References

- Bazhenova, A.P., Bakulin, F.G., 1957. Experimental studies of the mechanisms of moisture movement in freezing soils. In: Materials on laboratory research of frozen soils. AN SSSR, Moscow, No. 3, pp. 117–123 (in Russian).
- Beskow, G., 1935. Soil freezing and frost heaving with special application to roads and railroads. Swed. Geol. Soc., Ser. C, No. 375, 26 the yearbook No. 3, 145 pp.
- Black, P.B., 1995. Applications of the Clapeyron Equation to Water and Ice in Porous Media. US Army Corps of Engineers, Cold Regions Research and Engineering Laboratory (CRREL Rep.), No. 95-6, 6–7.
- Bliznin, G.Ya., 1890. Soil moisture according to observations of the Elizavetgradka meteorological station 1887–1889. Printing House of V. Demakov, St. Petersburg, pp. 239–262 (in Russian).
- Borozinets, V.E., Feldman, G.M., 1981. Vacuum-filtration mechanism of formation of thick layers of ice. In: Problems of Cryolithology. MGU, Moscow, iss. 9, pp. 165–178 (in Russian).
- Brovka, G.P., 1991. Heat and Mass Transfer in Natural Dispersed Systems During Freezing. Nauka i tekhnika, Minsk, 190 pp. (in Russian).
- Cass, L., Miller, R.D., 1959. Role of the electric double layer in the mechanism of frost heaving. USA Snow, Ice and Permafrost Research Establishment, Res. Rep. 49 (available from CRREL), 15 pp.
- Cheverev, V.G., 2003a. Classification of water bond forms in frozen fine-grained soils. Kriosfera Zemli [Earth’s Cryosphere], VII (3), 31–40.
- Cheverev, V.G., 2003b. Properties of bound water in cryogenic grounds. Kriosfera Zemli [Earth’s Cryosphere], VII (2), 30–41.
- Cheverev, V.G., 2004. Nature of Cryogenic Properties of Soils. Nauch. Mir, Moscow, 234 pp. (in Russian).
- Cheverev, V.G., Ershov, E.D., Magomedgadzhiyeva, M.A., Vidyapin, I.Y., 1998. Results of physical simulation of frost heaving in soils. In: Proceedings of the 7th International Conference on Permafrost Yellowknife, Yellowknife, Canada, pp. 145–149.
- Cheverev, V.G., Burnaev, R.S., Gagarin, V.E., Safronov, E.V., 2013. Influence of the external pressure on the degree of frost heaving of clay soils. Kriosfera Zemli [Earth’s Cryosphere], XVII (4), 57–62.
- Cvignunov, D.G., 2018. Influence of seasonally freezing soils on the foundations of vertical bar elements: Doctoral dissertation. Khabarovsk (in Russian).
- Dranitsyn, D.A., 1914. On some zonal landforms of the Far North. Pochvovedeniye [Pedology], No. 4, 21–68.
- Edlefsen, N.E., Anderson, A.B.C., 1943. Thermodynamics of soil moisture. Hilgardia 15 (2), 31–298.
- Ershov, E.D. (Ed.), 1999. Fundamentals of Geocryology. Part 5. Engineering geocryology. Frost heaving of soils and its impact on structures. MGU, Moscow, pp. 109–133 (in Russian).
- Ershov, E.D., Cheverev, V.G., Lebedenko, Yu.P., 1979. Experimental study of moisture migration and ice formation in the frozen zone of thawing soils. Vestnik MGU [Moscow State University Bulletin. Ser. 4. Geology], No. 1, 111–114.
- Goldstein, M.N., 1948. Deformations of the subgrade and engineering structures during freezing and thawing. In: Proceedings of NIIZhT, Transzheldorizdat, Moscow, vol. 16, 212 pp. (in Russian).
- Lebedev, A.F., 1919. Water Movement in Soils and Soils. Izvestiya Donskogo Agricultural Institute, Rostov na Dony, 220 pp. (in Russian).
- Nikiforov, K.O., 1912. On some dynamic processes in soils in the permafrost distribution area. Pochvovedeniye [Pedology], No. 2, 49–74.
- Orlov, V.O., 1962. Cryogenic Heaving of Fine-Dispersed Soils. AN SSSR, Moscow, 187 pp. (in Russian).
- Shchukin, E.D., Pertsov, A.V., Amelina, E.A., 2004. Colloidal Chemistry: Textbook. Publishing house of Moscow University, Moscow, 445 pp. (in Russian).
- Shtukenberg, V.I., 1894. About the fight against the depths on the Railways. Zhurnal Ministerstva putei soobshcheniya [Journal of the Ministry of Railways], book 2, pp. 24–30.
- Sungin, M.I., 1929. Physical and mechanical processes in wet and frozen soils in connection with the formation of depths on roads. Transpechat, Moscow, 196 pp. (in Russian).
- Taber, S., 1930. The mechanics of frost heaving. J. Geology 38 (4), 303–313.
- Thermodynamics of Soil Moisture, 1966. Translated from English and edited by A.M. Globus. Gidrometeoizdat, Leningrad, 437 pp. (in Russian).
- Tsyтович, N.A., 1973. Mechanics of Frozen Soils. Vyschaya shkola, Moscow, 446 pp. (in Russian).

Received November 13, 2020

Revised March 4, 2021

Accepted March 11, 2021

Translated by S.B. Sokolov

GEOTHERMAL FIELDS AND THERMAL PROCESSES IN CRYOSPHERE

SOIL TEMPERATURE IN THE CONTEMPORARY
NATURAL-CLIMATIC SITUATION OF THE STEPPE BAIKAL REGION
(ON THE EXAMPLE OF OLKHON ISLAND)A.A. Svetlakov¹, E.A. Kozyreva¹, D.O. Sergeev²¹*Institute of the Earth's Crust, SB RAS, Lermontov str. 128, Irkutsk, 664033, Russia; svetlakov@crust.irk.ru, kozireva@crust.irk.ru*²*Sergeev Institute of Environmental Geoscience, RAS, Ulansky per. 13, bld. 2, Moscow, 101000, Russia; sergueedo@mail.ru*

The paper analyzes the current temperature state of frozen and thaw soils in the Baikal region (Olkhon Island). It is shown that the current trend in soil temperature is directly related to climate change in and to the increase in the atmospheric air temperature. Permafrost within Olkhon Island is significantly transformed: the processes in soils are aimed at the degradation of frozen formations.

Keywords: permafrost, temperature regime, seasonally thawed and seasonally frozen layer.

INTRODUCTION

The purpose of this work is to estimate the state of the seasonally thawed and seasonally frozen layers near the southern boundary of the cryolithozone under conditions of recent climate change. The basic task of the study is to determine the temperature regime of permafrost and unfrozen soils and its transformation under conditions of freezing and thawing.

Climate significantly affects the thermodynamic regime of permafrost: changes in the air temperature can activate geocryological processes [Grosse *et al.*, 2011; Malkova *et al.*, 2011]. A positive trend in the air temperature has been established for the entire Baikal region: in 1965–2003, the temperature increased by 0.042–0.046 °C/yr [Pavlov, 2008; Malkova *et al.*, 2011]. Within the steppe zone in the Baikal region, on the Olkhon Island, an increase in the air temperature has led to the establishment of positive (above

0 °C) mean annual air temperatures in the recent years. Over the past 65 years, the trend of the mean annual air temperature has been 0.03 °C/yr (Fig. 1) [<http://gis.ncdc.noaa.gov>; <http://www.pogodaiklimat.ru>]. We have also calculated mean seasonal air temperatures for the cold and warm seasons corresponding to a hydrological year.

The main changes in the thermodynamic regime of permafrost depend on the air temperature. This is primarily reflected in the state of the seasonally frozen or seasonally thawed layers, where the main heat exchange occurs in the annual cycle of heat turnover [Kudryavtsev, 1978]. Changes in the thermal state of permafrost and permafrost degradation may continue for decades and centuries [Balobaev, 1971]. Therefore, the short-term studies do not always identify degradation of permafrost, whereas temperature changes in the active layer allow us to judge the re-

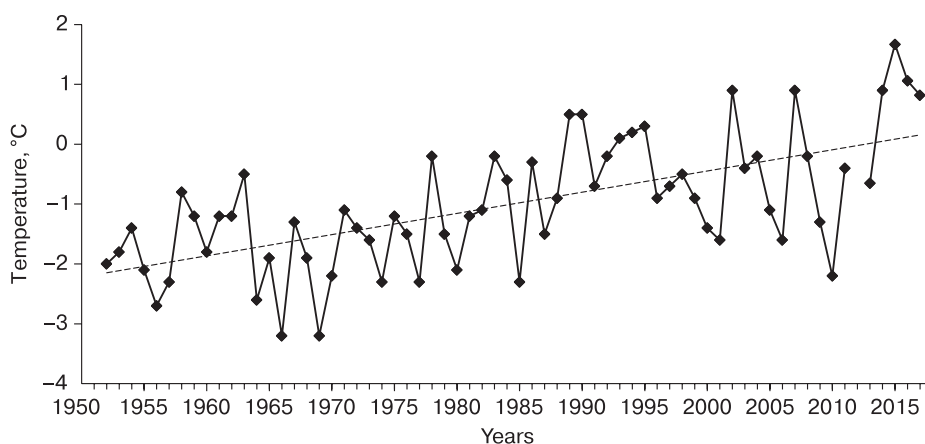


Fig. 1. Atmospheric air temperature on Olkhon Island; data from the Uzura weather station, 462 m a.s.l.).

Copyright © 2021 A.A. Svetlakov, E.A. Kozyreva, D.O. Sergeev, All rights reserved.

sponse of permafrost to the contemporary climate transformation and the direction of these processes.

STUDY AREA

Olkhon Island is located in the central part of Lake Baikal, on the border of the North Baikal and Middle Baikal depressions (Fig. 2) [Lut, 1978]. Detailed studies of the temperature regime of soils have been conducted on the western coast of Olkhon Island, northeast of the Kharantsy settlement, between Kharantsy and Kharaldai capes. The study site is allocated to a gentle slope of northwestern aspect; the slope surface topography is complicated by landslides of varying degrees of activity.

The entire Baikal steppe region is deficient in atmospheric precipitation. On Olkhon Island, annual precipitation ranges from 197 to 278 mm, and the annual ratio of precipitation to potential evapotranspiration is 0.34. Precipitation in the winter is particularly small; the snow cover depth does not exceed 10–15 cm [Imetkhenov et al., 1997; Pellinen, 2018]. The vegetation cover is poor and is represented mainly by steppe and meadow herbs [Khimenkov et al., 2015]. In the areas with permafrost, the vegetation cover is denser and richer. Surface sediments are mainly represented by the Quaternary colluvium (deluvial-proluvial sediments) and Neogene lacustrine and lacustrine-bog sediments. These sediments are involved in various exogenous geological processes [Palshin, 1968]. In terms of geocryology, this area belongs to the zone of isolated patches of permafrost. According to F.N. Leshchikov [1978], the thickness of permafrost in this zone does not exceed 10–15 m, the mean annual permafrost temperature ranges from -0.1 to -0.2 °C, and the permafrost table lies at a

depth of 2.0–2.5 m. The mean annual temperature of the active layer above the permafrost table is from -0.1 to -0.5 °C. The depth of seasonal freezing-thawing does not exceed 2.0–2.5 m. According to the thermal regime, permafrost in such areas is extremely unstable and may be subjected to degradation in the case of disturbances of the natural environment.

Four boreholes were drilled within the study area: Olh-12-1 with a depth of 3.5 m, Olh-13-1 with a depth of 8.0 m, Olh-13-2 with a depth of 9.0 m, and Olh-13-3 with a depth of 15.0 m. These boreholes can be divided into two groups: with and without permafrost (Fig. 2). Boreholes of the first group (Olh-12-1 and Olh-13-1) were drilled in the area of permafrost. The lithological section was studied to a depth of 8.0 m. The upper part of the section consisted of lacustrine clayey sediments with thin (1–3 cm) interlayers of loamy sand from a depth of 1.0 m. Temporary perched water was found at a depth of 1.5 m. Its presence resulted in an increased water content (up to 30 %) in the upper part of the section (0.5–1.0 m). From a depth of 1.9 m, the sediment was in the frozen state.

Boreholes of the second group (Olh-13-2 and Olh-13-3) were found 300 m away from the first group and penetrated unfrozen ground. Its lithological section of was studied to a depth of 15.0 m and consisted of clayey sediments with interlayers of sand. The lower part of the section was composed of clay of the lacustrine origin. The groundwater table was at a depth of 4.5 m. The water content in the upper part of the section (0.5–1.0 m) did not exceed 4–5 %. To determine the air temperature, a temperature sensor was installed at a height of 2.5 m at about 800 m southwest of the boreholes of the first group.

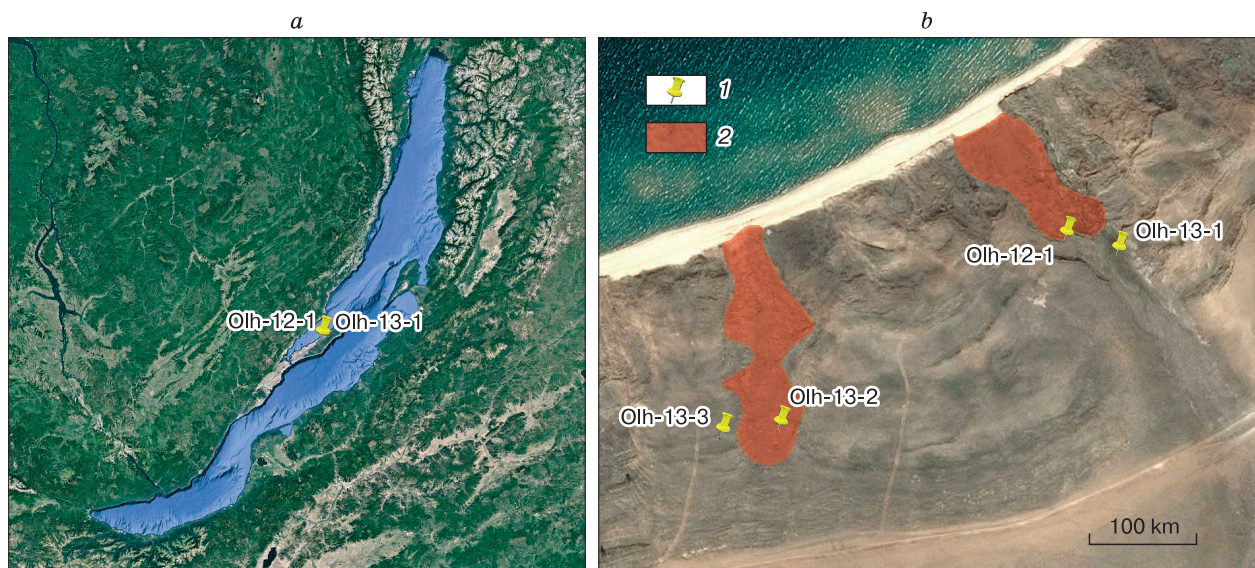


Fig. 2. Study area (a) and location of monitoring boreholes (b).

1 – boreholes; 2 – areas affected by landslides.

METHODS

Geocryological monitoring was carried out in the observation boreholes Olh-12-1, Olh-13-1, Olh-13-2, and Olh-13-3 in agreement with the recommendations of the Global Terrestrial Network for Permafrost (GTN-P) program, which is part of the Global Climate Observing System of the World Meteorological Organization. At the initial stage, the observation network was arranged on the basis of available technical means in order to determine the dynamics of changes in the temperature regime of soils within the seasonally thawed and seasonally frozen layers. The temperature sensors in borehole Olh-12-1, which was drilled in August 2012, were installed at the depths of 0.6 m, 1.0 m, 1.6 m and 3.5 m. In August 2013, boreholes Olh-13-1, Olh-13-2, and Olh-13-3 were drilled, and the temperature sensors were installed in them at the depths of 0.1 m, 2.0 m and 4.0 m. The maximum depth of the installation of the temperature sensor in borehole Olh-13-3 was 9.3 m.

We used temperature sensors (loggers) produced by the Onset Computer Corporation: HOBO U12-008, HOBO Pro V2 Temperature/Relative Humidity Data Logger, and HOBO UA-001-64 Pendant Temperature/Alarm (Waterproof) Data Logger. Loggers of the HOBO U12-008 type were installed in boreholes Olh-12-1, Olh-13-2, and Olh-13-3; they ensured the accuracy of measurements of ± 0.1 °C. Loggers of the HOBO Pro V2 type with the accuracy of measurements of ± 0.2 °C were installed in borehole Olh-13-1. Logger HOBO UA-001-64 recorded the air temperature with an accuracy of ± 0.4 °C. The air and soil temperatures were recorded every hour.

RESULTS

Air temperature. According to the results of air temperature measurements performed since 2013, the mean annual air temperature in the study area ranges

from -1.2 to 1.7 °C, which is close to the results obtained at the Uzury weather station (462 m a.s.l.) located in the steppe zone to the north of the study area.

The calculation of the mean annual temperatures corresponds to the hydrological year and includes two periods: winter (October to March) and summer (April to September). During the observation period from 2013 to 2018, the mean annual air temperature in the study area rose above 0 °C. An insignificant, but stable increase in the air temperature took place in the warm (summer) period (April–September) (Fig. 3, *a*). In 2013, the mean air temperature during the warm period was 9.6 °C; in 2018, it reached 12.1 °C. In the cold (winter) period (October–March), the general trend of the air temperature also demonstrates a positive trend, although a longer observation period is required for reliable conclusions (Fig. 3, *b*). A significant rise in the temperature of the cold season (by 4.8 °C) took place in 2014 in comparison with 2013. However, since 2014, the mean values of the air temperature during the cold season have decreased from -7.4 to -10.3 °C.

Soil temperature. In 2012, in borehole Olh-12-1, permafrost at a depth of 3.5 m was characterized by the subzero mean annual temperature of -0.1 °C [Svetlakov, 2018]. Since the beginning of our observations, the temperature at the top of permafrost remained in the subzero range throughout the year up to 2015. In 2015, the transition from to above-zero temperatures at this depth took place in the annual cycle, i.e., the permafrost table lowered, and the thickness of the seasonally thawed layer increased.

The temperature of the active layer in the study area also changed in 2013–2018. Thus, at a depth of 0.1 m, the mean annual temperature varied from 2.9 to 4.4 °C. The soil temperature during the year at a depth of 0.1 m ranged from -21.3 to 24.4 °C. During the period of monitoring, high temperature values in

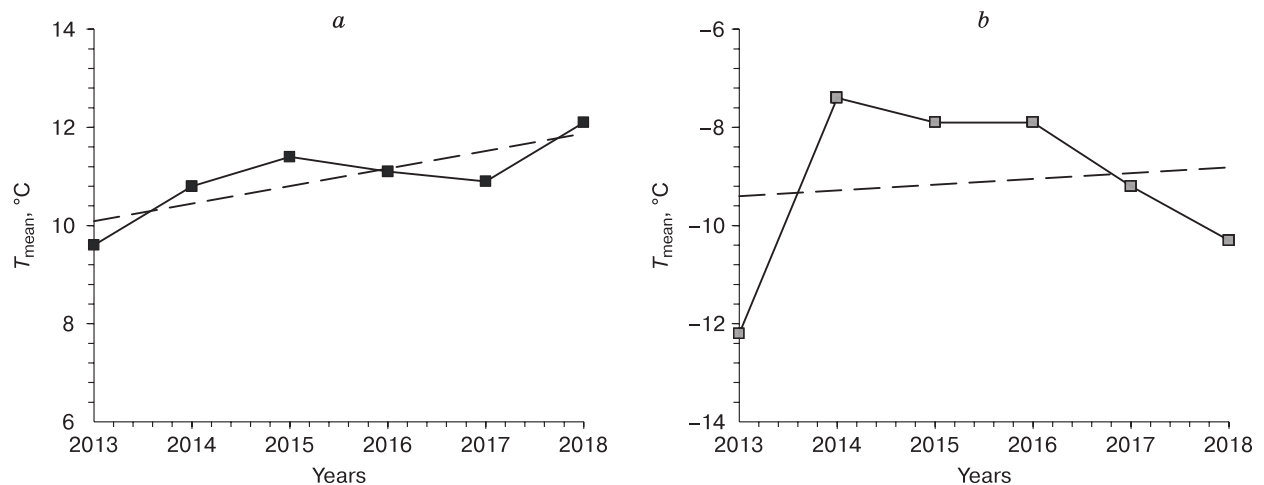


Fig. 3. The mean seasonal air temperature T_{mean} during the warm (*a*) and cold (*b*) seasons in the study area.

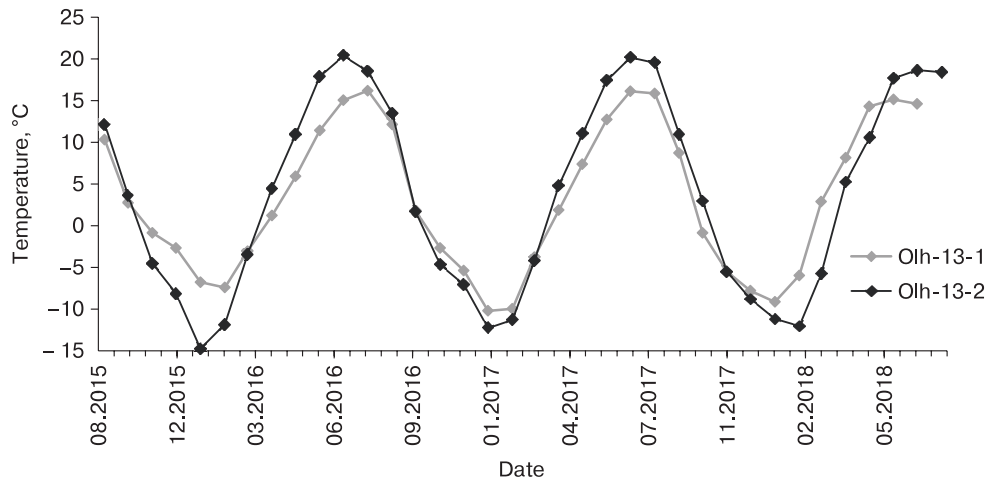


Fig. 4. The mean monthly temperatures at a depth of 0.1 m in the areas with permafrost (borehole Olh-13-1) and unfrozen ground (borehole Olh-13-2).

the annual cycle and a shift towards a positive gradient indicate the additional warming of soils on the surface.

In 2018, within the permafrost area (borehole Olh-13-1), the annual amplitude of soil temperatures at a depth of 0.1 m was 29.9 °C (from -11.2 to 18.7 °C), whereas the annual amplitude of air temperatures reached 53.9 °C (from -31.1 to 22.8 °C). In the unfrozen area (borehole Olh-13-2), the annual amplitude of soil temperatures at a depth of 0.1 m was 44.0 °C (from -20.0 to 24.0 °C), at a depth of 0.1 m). The amplitude of the mean monthly soil temperatures at a depth of 0.1 m ranged from -10.2 to 16.2 °C for the permafrost area, and from -14.8 to 20.4 °C for the unfrozen area (Fig. 4).

A significant difference between soil temperature ranges at the frozen and unfrozen sites attests to the high thermal resistance of permafrost (i.e., the need to spend more energy to warm up the soil), as well as to a higher sensitivity of unfrozen ground to changes

in the air temperature. The water content of soils and vegetation conditions have an additional impact. Vegetation is denser in the area with permafrost development and protects the soil from temperature changes both in summer and in winter. The seasonally thawed layer in the area with permafrost freezes more intensively, and the transition through 0 °C proceeds quicker.

The annual amplitude of temperatures at a depth of 2.0 m within the seasonally thawed layer (borehole Olh-13-1) is 13.8 °C (from -4.3 to 9.5 °C). As noted earlier, permafrost in this area was found at a depth of 1.9 m. As the drilling was carried out in August, the thawing depth in the borehole somewhat increased, and subzero temperatures at a depth of 1.9 m were established only in January (Fig. 5).

In the area of unfrozen ground (borehole Olh-13-3), the temperature at a depth of 2.0 m drops to 0 °C. However, below this depth, it remains in the positive range. Thus, this depth indicates the maxi-

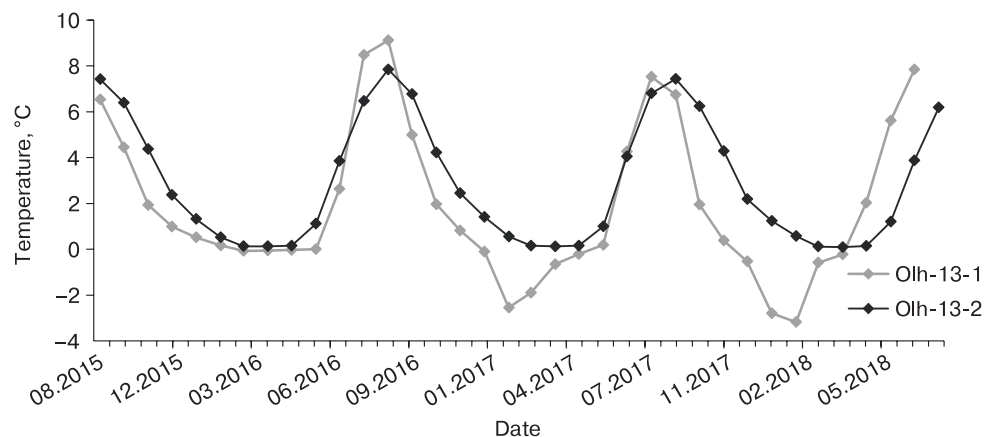


Fig. 5. The mean monthly temperature at a depth of 2.0 m in the areas with permafrost (borehole Olh-13-1) and unfrozen ground (borehole Olh-13-2).

imum depth of seasonal soil freezing. The annual amplitude of temperatures at this depth in the area with unfrozen ground reaches 7.9 °C (0.1 to 8.0 °C).

The mean annual soil temperature at a depth of 2.0 m, within the active layer of both plots (with and without permafrost) in the steppe zone of the Baikal region was steadily rising during the monitoring period. Thus, in borehole Olh-13-3 (unfrozen ground), the mean annual temperature soil temperature at this depth (within the seasonally freezing layer) increased from 2.6 to 3.0 °C. The temperature below the seasonally freezing layer also increased; at a depth of 9.3 m, the mean annual temperature was 1.8 °C in 2013 and 2.4 °C in 2018 (Fig. 6).

The mean annual soil temperature at a depth of 2.0 m, within the seasonally thawing layer in the area with permafrost (borehole Olh-13-1) varied from 2.0 to 2.1 °C, which was higher than the data published earlier [Leshchikov, 1978].

The mean annual soil temperature at a depth of 3.5 m during the study period in the permafrost area (borehole Olh-12-1) increased from -0.1 to 0.7 °C, which indicates an increase in the depth of seasonal thawing from 2.5–3.0 m to more than 3.5 m in the area with isolated permafrost patches in steppe landscapes of the Baikal region (Fig. 7).

Within the steppe area, previous geocryological studies were conducted in 1984. Initial observations demonstrated that the mean annual temperature of permafrost ranged from -0.1 to -0.2 °C, and the total water content was in the range of 30–40 %. Permafrost table was found at a depth of 2.0–2.5 m [Leshchikov *et al.*, 1984]. During the study period from 2013 to 2018, the general trend of changed in the mean annual temperature was close to the regional trend of changes in the air temperature in the region, the main factor affecting regional soil temperatures.

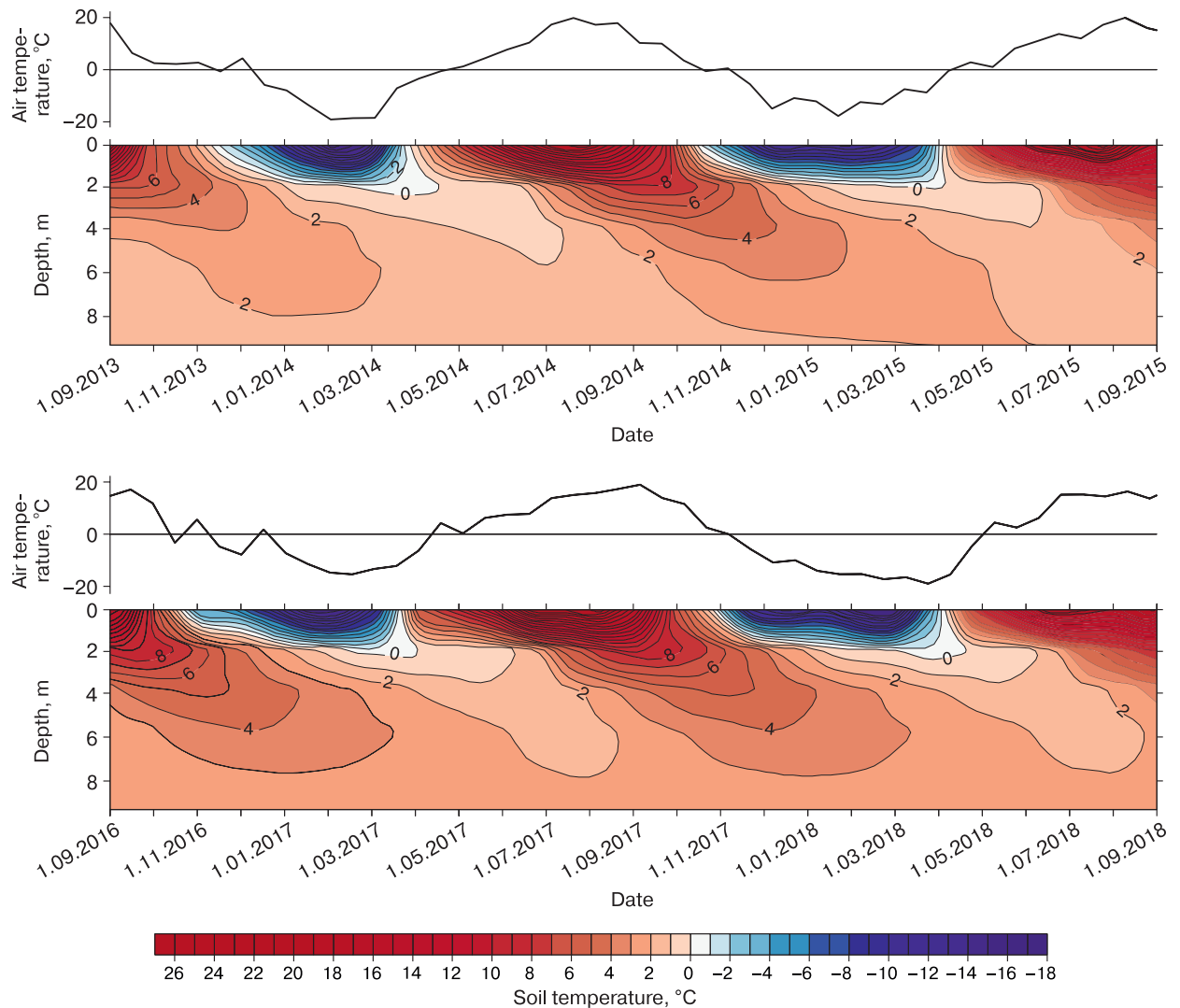


Fig. 6. Thermaisopleths of soils, borehole Olh-13-3.

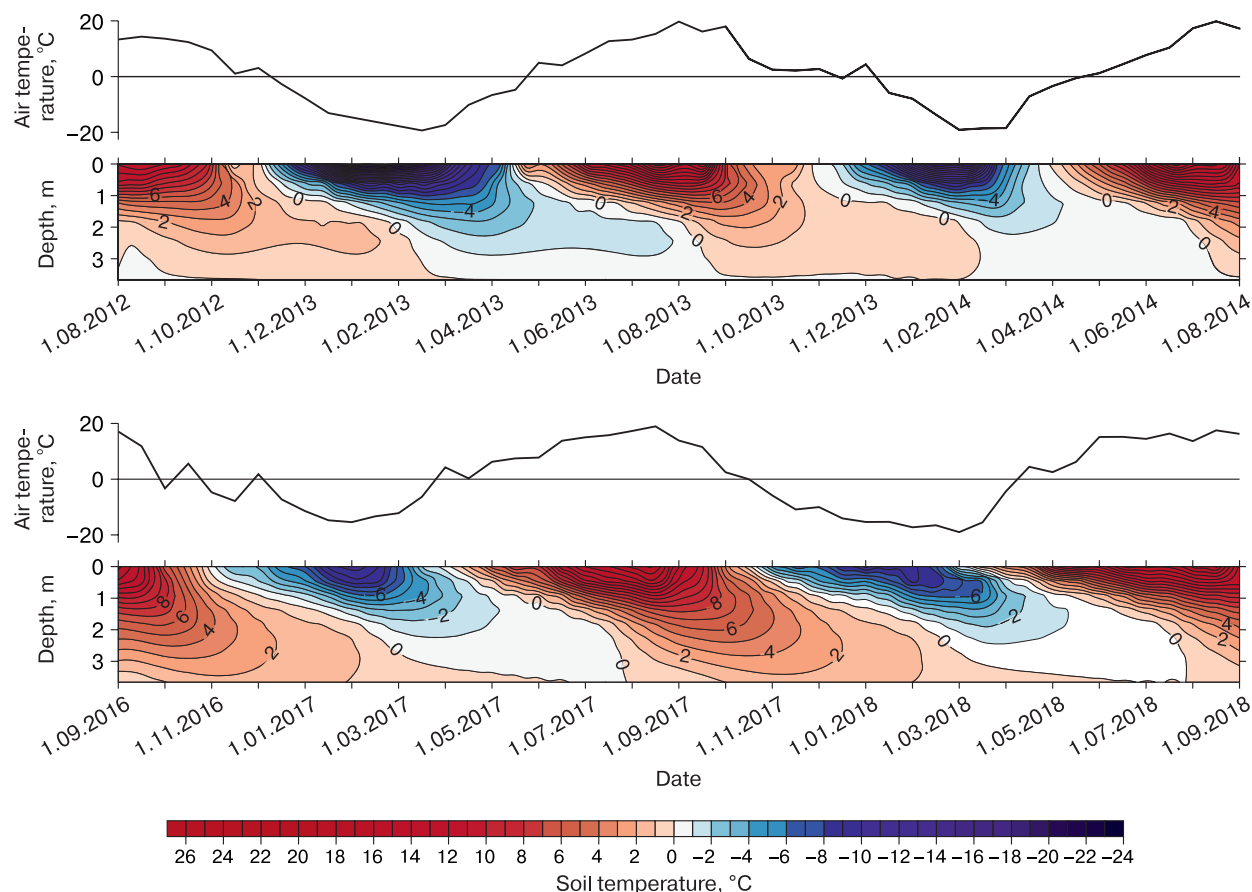


Fig. 7. Thermoisopleths of frozen soils, borehole Olh-12-1.

DISCUSSION

The temperature regime of permafrost is transformed under the current trend of the air temperature. The change in the soil temperature is largely related to the modern rise in the air temperature. The influence of the secondary factors (precipitation, vegetation cover, moisture) has led to additional warming of soils and local thawing of permafrost.

Olkhon Island is characterized by insufficient atmospheric moistening. The annual precipitation varies from 197 to 278 mm, and the ratio of annual precipitation to the total evapotranspiration is 0.34. Most of precipitation falls during the three summer months. In winter, monthly precipitation does not exceed 5 mm and the snow cover thickness does not exceed 10–15 cm [Imetkhenov *et al.*, 1997; Pellinen, 2018], which is insufficient to moist the surface soil layer. The soil water content on the plot with unfrozen clayey sediments (boreholes Olh-13-2 and Olh-13-3) reaches 4.5 and 6.3 %, respectively, in the upper part of the profile (0–1 m) and increases to 29.2 and 27.0 % at the depths up to 4.0 m. Vegetation on the surface does not form the dense cover and, therefore, the summer heating of the surface soil is intense.

On the plot with permafrost (boreholes Olh-12-1 and Olh-13-1), the water content of clayey sediments in the upper layer varies from 23.4 to 30.7 %, which is comparable with the data obtained several decades ago [Leshchikov *et al.*, 1984]. An increased water content creates more favorable conditions for the formation of a stable vegetation cover. This is the reason for the difference in the amplitudes of temperatures in the surface soil layers in the annual cycle at the plots with permafrost and unfrozen soil (Fig. 4). During the cold season, before the establishment of subzero temperatures on the surface, the amount of atmospheric precipitation decreases and the remaining water migrates towards the top of permafrost. Thus, soil freezing begins at low values of the water content in the surface soil layers. An abnormally high for clayey soils value of seasonal soil thawing in borehole Olh-12-1 is apparently explained by a relatively low soil water at the initial stage of thawing. The low water content in the surface soil layer contributes to a greater soil warming and deeper soil thawing. Taking into account a continuous rise summer temperature, the changes in the soil temperature regime occur both in the active (seasonally thawed) layer and in

the underlying permafrost. During the study period, the mean annual soil temperatures display a positive trend throughout the section. This is related to the changes in the air temperature against the background of insignificant precipitation and the low soil water content.

Seasonal freezing on the plot with unfrozen soil occurs intensively; however, as winter air temperatures remain relatively high, the depth of soil freezing does not reach 2.0 m. The thawing of seasonally frozen soil layer in the steppe zone on the plot with unfrozen soil proceeds without delay, because the snow cover is very thin, and the vegetation cover is poor and weakly protects the surface from warming. In combination with a low soil water content, thermal conductivity of the soils increases, and the soil layer frozen in winter thaws out quickly in May; then, it is subjected to a gradual warming and remains in the thawed state almost until November (Fig. 6).

During the observation period from 2012 to 2018, the soil temperature within the active layer on the plot with permafrost (borehole Olh-12-1) displayed a trend toward gradual rising. In 2012, permafrost temperature at a depth of 3.5 m was in the subzero range (from 0 to -0.1 °C), which was slightly higher than that in the 1980s [Leshchikov *et al.*, 1984]. In 2015, there was a transition from subzero to above-zero values: the maximum temperature at a depth of 3.5 m reached 1.3 °C. In 2017–2018, the maximum soil temperature at this depth was already 1.7 °C.

Changes in the temperature regime of permafrost are associated with a general increase in the ambient air temperature and with the low atmospheric precipitation. The soil water content on the plots with permafrost is higher than that on the plots with unfrozen soil. However, owing to the downward migration of moisture migration towards the underlying permafrost table, the soil freezing from the top occurs without significant delay and proceeds to the full depth of the soil thawing. The mean annual soil temperature on the plot with permafrost varies from -0.3 to 1.3 °C. The active layer, thawed in summer, completely freezes in winter. Under the conditions of constantly increasing temperature both in the warm and cold periods, the soil thawing depth reaches 3.5 m. If the current trend for temperature rise, insufficient atmospheric moistening, and changes in the soil water content on the plots with permafrost is preserved, we can expect the formation of taliks and permafrost degradation in the steppe landscapes of Olkhon Island.

Compared to other areas in the Baikal region, permafrost on Olkhon Island is under high stress related to the current climate change. Therefore, the Olkhon station organized by the Institute of the Earth's Crust of the Siberian Branch of the Russian Academy of Sciences should be maintained and developed as one of the reference points for monitor-

ing the natural state of permafrost at its southern boundary.

CONCLUSIONS

Permafrost at the boundary of the southern geocryological zone is subjected to significant transformation under the influence of climate change. In the study area of the steppe region of Olkhon Island, the ambient air temperature demonstrates a positive trend. From 2013 to 2018, annual air temperature increased from -1.2 to 1.7 °C. The main growth took place in the summer period, owing to which the surface soil warming became more intense.

The mean annual temperature of unfrozen soil also demonstrated the rise throughout the entire massif; the depth of soil freezing on this plot did not exceed 2.0 m. The soil temperature on the plot with permafrost also increased, which contributes to degradation of high-temperature permafrost in the zone of isolated patches of permafrost. The thawing depth lowered deeper than 3.5 m, and the mean annual temperature increased to 1.7 °C.

Migration of moisture has a significant influence on the temperature regime of soils in Olkhon Island. The water content in the areas of unfrozen soil in the near-surface layer is 4.5 and 6.3 %, which accelerates the soil freezing, and the phase transition occurs without delay. In the areas with permafrost, the soil water content is higher and varies from 23.4 to 30.7 %. However, due to migration of moisture to the top of permafrost and the positive trend of air temperature, soil thawing reaches the maximum values and contributes to the formation of taliks.

Acknowledgments. *The authors are grateful to candidate of geological and mineralogical sciences A.A. Rybchenko and candidate of geological and mineralogical sciences V.A. Pellinen and the staff of the Laboratory of Engineering Geology and Geocology for their substantial assistance in the fieldwork.*

This work was carried out within the framework of State Assignment No. AAAA-A19-119021190077-6 (IGERAN). It was supported by grant No. 075-15-2020-787 in the form of subsidies for the major research projects of the Ministry of Science and Higher Education of the Russian Federation (project "Fundamental Bases, Methods and Technologies of Digital Monitoring and Forecasting of Ecological Conditions in the Baikal Natural Area").

References

- Balobaev, V.T., 1971. Peculiarities of geothermal processes in regions with permafrost rocks. In: Geocryological research. Yakutsk book publishing house, Yakutsk, pp. 9–17 (in Russian).
- Grosse, G., Romanovsky, V., Jorgenson, T., et al., 2011. Vulnerability and feedbacks of permafrost to climate change. *Eos, Transactions American Geophysical Union*, 92 (9), 73–74.

- Imetkhenov, A.B., Dolkhonova, E.Z., Elbaskin, P.N., 1997. Olkhon is a Native Land. Publishing house of Buryat State University, Ulan-Ude, 352 pp. (in Russian).
- Khimenkov, A.N., Sergeev, D.O., Vlasov, A.N., et al., 2015. Modern and paleo-cryogenic formations on Olkhon Island. *Earth's Cryosphere* XIX (4), 48–57.
- Kudryavtsev, V.A. (Ed.), 1978. *General Permafrost Science (Geocryology)*. Publishing house of Moscow University, Moscow, 464 pp. (in Russian).
- Leshchikov, F.N., 1978. Frozen rocks of the Angara and Baikal Regions. Nauka, Novosibirsk, 145 pp. (in Russian).
- Leshchikov, F.N., Spesivtsev, V.I., Miroshnichenko, A.P., 1984. Landslide deformations on the shores of Olkhon Island. In: *Coastal Processes in Permafrost*. Nauka, Novosibirsk, pp. 71–77 (in Russian).
- Lut, B.F., 1978. *Geomorphology of the Baikal Region and Basins of Lake Baikal*. Nauka, Novosibirsk, 213 pp. (in Russian).
- Malkova, G.V., Pavlov, A.V., Skachkov, Yu.B., 2011. Assessment of permafrost stability under contemporary climatic changes. *Kriosfera Zemli [Earth's Cryosphere]*, XV (4), 33–36.
- Palshin, G.B., 1968. *Engineering geology of the Baikal region*. Nauka, Moscow, 194 pp. (in Russian).
- Pavlov, A.V., 2008. Trends of contemporary changes of soil temperature in northern Russia. *Kriosfera Zemli [Earth's Cryosphere]*, XII (3), 22–27.
- Pellinen, V.A., 2018. Assessment of the stability of the geological environment of Olkhon Island. *Cand. Sci. (Geol.-Mineral.) Diss., Irkutsk*, 136 pp. (in Russian).
- Svetlakov, A.A., 2018. Features of the temperature regime of soils in the conditions of the southern geocryological zone of Eastern Siberia. *Cand. Sci. (Geol.-Mineral.) Diss., Irkutsk*, 153 pp. (in Russian).
- URL: <http://gis.ncdc.noaa.gov/map> (last visited: 20.10.2018).
- URL: <http://www.pogodaiklimat.ru/weather.php?id=30637> (last visited: 07.05.2018).

Received July 30, 2020

Revised May 4, 2021

Accepted June 18, 2021

Translated by V.A. Krutikova

CRYOGENIC PHENOMENA IN SEAS AND OCEANS

INTERANNUAL VARIATIONS OF MAXIMAL FAST ICE EXTENT
IN THE EAST SIBERIAN SEA

V.V. Selyuzhenok

*Zubov State Oceanographic Institute, Roshydromet,
Kropotkinskij per. 6, Moscow, 119034, Russia; v1selyuzhenok@oceanography.ru*

The paper presents the data on maximal extent of the East Siberian Sea fast ice and its variability based on the Arctic and Antarctic Research Institute operational sea ice chart for the period from 1999 to 2019. The maximal fast ice extents were compared to the ERA5 reanalysis local winds. The analysis of the maximal fast ice variability showed no statistically significant changes between 1999 and 2019. Two typical configurations of fast ice edge were revealed for the winter month characterized by the maximal fast ice extent. In some seasons fast ice development stops, once the edge reaches 20 m depths, while in other season the fast ice edge advances to 30 m depths. The maximal fast ice extent is reached during the seasons with prevailing onshore northerly and north-easterly wind. The onshore wind favors sea ice deformation and grounding at the seaward fast ice edge.

Keywords: *landfast sea ice, sea ice, stamukhas.*

INTRODUCTION

The East Siberian Sea is located in the zone affected by the Atlantic and Pacific Ocean atmospheric interactions. The region is characterized by the shortest summer and the coldest winter among the Russian Arctic shelf seas. In winter the atmospheric wind regime is mainly defined by the Siberian High with a less effect of the Polar High. This results in the domination of south-easterly and southerly winds with a mean speed of 6–7 m/s. Atlantic cyclones, prevailing in the western part of the sea, and Pacific cyclones, prevailing in the southeastern part of the sea, cause an increase in the winds in the north and northeast directions [Dobrovolskij, Zalogin, 1982]. The northerly and north-easterly wind favor formation of rafted and ridged sea ice in the region. The formation and development of sea ice cover take place during the entire winter period and ends in the end of May [Yulin *et al.*, 2018]. The western part of the East Siberian Sea is characterized by the presence of favorable factors for the formation of fast ice: a rugged coastline, the presence of islands and shallow waters that allow the formation of stamukhas and the absence of strong tidal currents [Zubov, 1945]. The fast ice extent around the New Siberian Islands at its maximal development comprises more than a half of the total fast ice area in the Russian Arctic [Karklin *et al.*, 2013]. The water depth and the underwater relief are the main factors limiting maximal fast ice extent. Commonly, the seaward fast ice edge follows the contours of 20 to 25 m isobaths [Gudkovich, 1974; Mahoney *et al.*, 2014]. The fast ice regime in the region is described in details in [Karklin, Karelin, 2009].

Currently, due to observed climate changes and developing economic activity in the Arctic, the sea ice state and regime have been actively observed and investigated. Based on the sea ice charts produced by Arctic and Antarctic Research Institute (AARI) and National Oceanic and Atmospheric Administration (NOAA) trends in the duration of fast ice season were derived [Divine *et al.*, 2004; Yu *et al.*, 2014; Selyuzhenok *et al.*, 2015]. The analysis of NOAA data revealed a negative trend in fast ice area for all Russian Arctic shelf seas, while the total fast ice area in the Northern hemisphere decreases with a speed of $12.27 \cdot 10^3 \text{ km}^2$ ($7 \pm 1.5 \%$) per decade [Yu *et al.*, 2014]. The aim of this study is to evaluate the interannual variability of the maximal fast ice extent in the East Siberian Sea from 1999 to 2019.

DATA

The data on fast ice extent and the location of fast ice edge in the East Siberian Sea were retrieved from the regional sea ice charts produced at AARI for the period 1999–2019. The sea ice charts are freely available in SIGRID-3 format [<http://wdc.aari.ru/>]. Since 1998 the charts are mainly based on the information from the satellite remote sensing, which is analyzed by an expert. The charts are drawn at a scale 1:500 000 and issued on a weekly basis. Thus, the sequence of sea ice charts allows to create the most accurate homogeneous series of observation on the fast ice state.

Figure 1 shows the mean seasonal changes in fast ice extent in the East Siberian Sea. The average fast ice extent in February–May was used as the maxi-

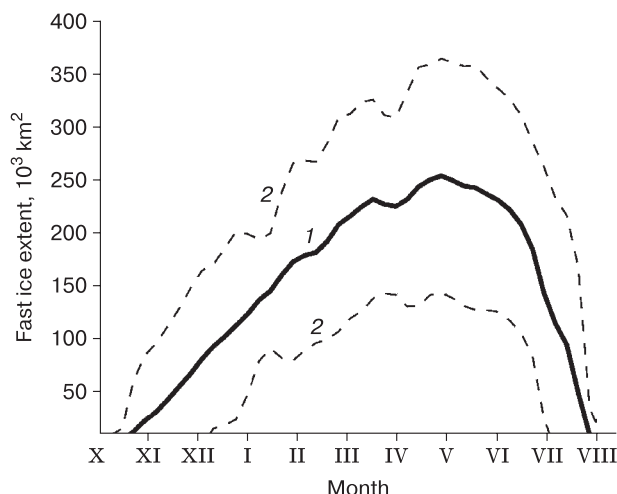


Fig. 1. Mean seasonal changes in fast ice extent in the East Siberian Sea for 1999–2019.

1 – mean value; 2 – two standard deviation from the mean.

mum fast ice extent. From October to May, the fast ice extent increases, and from June it begins to decrease (Fig. 1). Due to gap in sea ice charts in winter period 2002–2003, this period was excluded from the analyses.

The ERA5 reanalysis data [Hersbach et al., 2020] were used to obtain wind speed and direction in the region. Compared to other reanalysis models (ERA-Interim, Japanese 55-year Reanalysis, Modern Era Retrospective Analysis for Research and Applications-2, National Centers for Environmental Prediction / National Center for Atmospheric Research Reanalysis 1), ERA5 reproduces wind speed and direc-

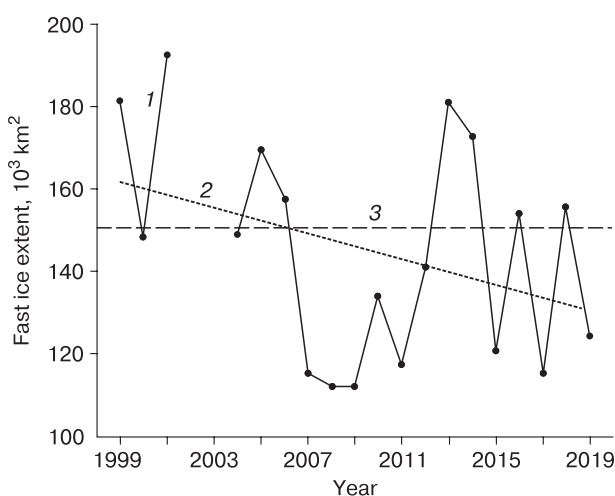


Fig. 2. Variations in maximal fast ice extent in the East Siberian Sea for 1999–2019.

1 – mean fast ice extent in February–May; 2 – linear trend; 3 – multi-annual average value of fast ice extent in February–May (1999–2019).

tion with high accuracy [Ramon et al., 2019]. The mean daily wind speed and direction for the marine part of the region were derived from hourly meridional and zonal wind components at 10-m level. Next, we calculated the frequency of wind in eight directions and the number of calms (the number of days with an average wind speed of less than 0.5 m/s) from the beginning of November to the end of May, which covers the period from the beginning of fast ice formation to the beginning of its decay.

RESULTS AND DISCUSSION

Figure 2 shows interannual variability of the maximal fast ice extent (February–May) for 1999–2019. The mean interannual fluctuations of fast ice extent comprises 15 %, but in some season can exceed 30 % from multi-annual mean. The minimal fast ice extent was observed from 2007 to 2012. This period coincides with the seasons of record low summer sea ice extent in the eastern Arctic. The maximal retreat of sea ice edge in summer in the East Siberian Sea was observed in 2007 [Egorov, 2020]. The linear trend for fast ice extent comprises $-1.6 \cdot 10^3 \text{ km}^2$ for 1999–2007, but it is not statistically significant (p -level $< 90 \%$).

In the seasons with negative fast ice extent anomaly in February–May, the location of fast ice edge coincides with the contours of 20–25 m isobaths (Fig. 3). In the seasons with positive extent anomaly, in the central part of the region fast ice edge shifts to the north and reaches 30-m isobath. The main differences in the average position of the edge are observed between the 155° E and 170° E.

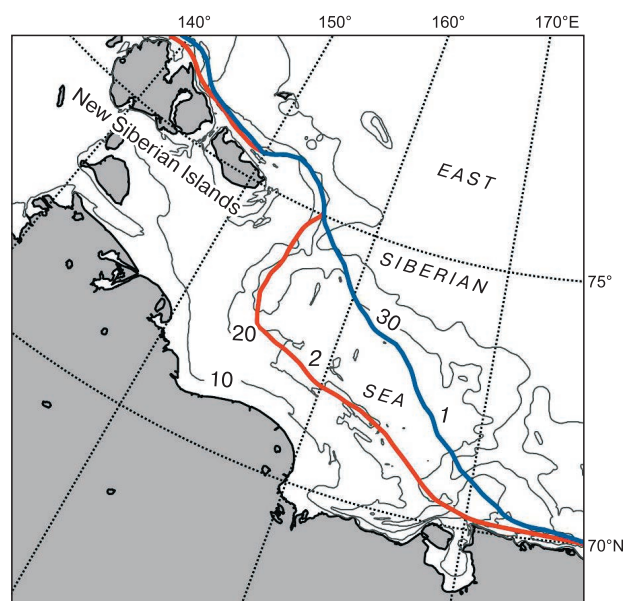


Fig. 3. Mean location of fast ice edge in February–May:

1 – in seasons with positive fast ice extent anomaly; 2 – in seasons with negative fast ice extent anomaly.

Table 1. Frequency of wind occurrence in directions; number of calms

Years	Frequency of wind occurrence in directions, %								Number of calms
	N	NE	E	SE	E	SW	W	NW	
With positive fast ice extent anomaly	18.8	26.2	12.1	9.2	6.2	6.0	10.0	11.5	4
With negative fast ice extent anomaly	14.9	7.0	10.7	10.7	20.3	13.3	10.1	13.0	11

An analysis of the surface wind frequency shows that seasons with a positive fast ice extent anomaly are characterized by onshore northerly and north-easterly winds (Table 1). The total frequency of winds of these directions in seasons with a negative extent anomaly is 2 times lower. For the seasons with negative fast ice extent anomaly, the southerly winds, which push the sea ice away from the shore, are the most frequent. The occurrence of calms from November to May for seasons with both positive and negative anomalies of the fast ice extent is less than in 15 days (9%).

The correspondence between the fast ice extent variations and predominant wind directions indicate a close relationship between the processes. The role of onshore winds in the seasonal formation of fast ice was first described in [Zubov, 1945]. The mechanism of interaction between the wind direction and fast ice extent is clear: under the influence of pressure winds, drifting ice fields are shifted to the fast ice boundary. As a result of strong compression, they freeze to the previously formed fast ice. Such a mechanism of an abrupt increase in the fast ice extent in the adjacent to the East Siberian Sea, Laptev Sea is described in modern works (for example, [Karklin et al., 2013]). When changing the mode of the prevailing wind direction from onshore to offshore, the sea ice is held in place and freezes in the fast ice cover. The location of fast ice edge the period of its maximum development in the eastern part of the Laptev Sea coincides with the contour of 20–25 m isobaths and shows no inter-annual variations. The variations of fast ice maximal extent there do not ice in the sea do not exceed 15% [Selyuzhenok et al., 2015]. According to [Gudkovich, 1974], 1.5–2 m thick fast ice [Karklin et al., 2013] cannot withstand the combined effect of tangential wind forces and tidal phenomena acting at the fast ice edge at 20–25 m depths. At greater water depth stamukhas provide additional additional support 25 m [Gorbunov et al., 2008]. The absence of stamukhas is another factor which might limit the development of fast ice to 20–25 m depth. In the East Siberian Sea, the distribution of fast ice up to the 30 m isobath (the position of the edge 1 in Fig. 3) is observed only in seasons with a predominance of onshore winds. It is likely that with the predominance of the offshore wind directions, a sufficient number of stamukhas capable of holding the fast ice of a large area in place are not formed.

CONCLUSIONS

The fast ice extent in the East Siberian Sea shows a large long-term interannual variability. The mean variations of fast ice extent are 15 %, but in some years they can exceed 30 % of the long-term average. Depending on the prevailing wind directions, the fast ice edge in the period of maximum development occupies one of two characteristic positions: 1) the seaward edge of the fast ice coincides with location of the 20 m isobath; 2) the seaward edge of the fast ice in the central part of the water area protrudes to the north and approaches the 30 m isobath. Fast ice reaches its maximum extent in winters with prevailing onshore winds, which likely contribute to ice hummocking and the formation of stamukhas. Stamukhas are additional support points for fast ice, due to which fast ice is able to withstand the forces of wind and tidal phenomena at depths of more than 25 m. The analysis of fast ice extent time series shows no statistically significant trend during the period between 1999 and 2019.

This research was funded by RFBR, project number 19-35-60033.

References

- Divine, D.V., Korsnes, R., Makshtas, A.P., 2004. Temporal and spatial variation of shore-fast ice in the Kara Sea. *Continental Shelf Research* 24 (15), 1717–1736.
- Dobrovolskij, A.D., Zalogin, B.S., 1982. *Seas of the USSR*. Izd-vo MGU, Moscow, 192 pp. (in Russian).
- Egorov, A.G., 2020. Spatial location of ice edge in August–September in the Russia’s eastern seas in early 21st century. *Problemy Arktiki i Antarktiki [Arctic and Antarctic Research]*, 66 (1), 38–55.
- Gorbunov, Yu.A., Losev, S.M., Dymant, L.N., 2008. Stamukhas of the Laptev Sea. *Problemy Arktiki i Antarktiki [Arctic and Antarctic Research]*, 79 (2), 111–116.
- Gudkovich, Z.M., 1974. The influence of tangential wind and wave action on fast ice. *Trudy AANII [Transactions of AARI]*, vol. 316, 96–106.
- Hersbach, H., Bell, B., Berrisford, P., et al., 2020. The ERA5 global reanalysis. *Quarterly J. Royal Meteorol. Soc.*, No. 146, 1999–2049.
- Karklin, V.P., Karelin, I.D., 2009. Seasonal and interannual variability of sea ice regime in the Laptev and East Siberian Sea. In: *System of the Laptev Sea and the Adjacent Arctic Seas: Modern and Past Environment*. Izd-vo MGU, Moscow, pp. 187–201 (in Russian).
- Karklin, V.P., Karelin, I.D., Yulin, A.V., Usoltseva, A.E., 2013. Peculiarities of the landfast ice formation in the Laptev Sea. *Problemy Arktiki i Antarktiki [Arctic and Antarctic Research]*, 97 (3), 11–14.

- Mahoney, A.R., Eicken, H., Gaylord, A.G., Gens, R., 2014. Landfast sea ice extent in the Chukchi and Beaufort Seas: The annual cycle and decadal variability. *Cold Regions Sci. and Technol.*, vol. 103, 41–56.
- Ramon, J., Lledó, L., Torralba, V., et al., 2019. What global re-analysis best represents near-surface winds? *Quarterly J. Royal Meteorol. Soc.*, No. 145, 3236–3251.
- Selyuzhenok, V., Krumpen, T., Mahoney, A., et al., 2015. Seasonal and interannual variability of fast ice extent in the southeastern Laptev Sea between 1999 and 2013. *J. Geophys. Reseach: Oceans*, 120 (12), 7791–7806.
- Yu, Y., Stern, H., Fowler, C., et al., 2014. Interannual variability of Arctic landfast ice between 1976 and 2007. *J. Climate* 27 (1), 227–243.
- Yulin, A.V., Sharatunova, M.V., Pavlova, E.A., Ivanov, V.V., 2018. Seasonal and interannual changes of ice massifs in East Siberian sea. *Problemy Arktiki i Antarktiki [Arctic and Antarctic Research]*, 64 (3), 229–240.
- Zubov, N.N., 1945. *Arctic Ice*. Izd-vo Glavsevmorputi, Moscow, 360 pp. (in Russian).
URL: <http://wdc.aari.ru/datasets/d0004/> (last visited: 05.05.2021).

Received August 10, 2020

Revised June 10, 2021

Accepted June 15, 2021

Translated by the author

SNOW COVER AND GLACIERS

MASS BALANCE MODELLING FOR THE SARY-TOR GLACIER
(THE AK-SHYIRAK MASSIF, INNER TIEN SHAN)E.P. Rets¹, D.A. Petrakov², E.V. Belozеров¹, A.M. Shpuntova²¹*Water Problems Institute, RAS, Gubkina str. 3, Moscow, 119333, Russia; retska@mail.ru*²*Lomonosov Moscow State University, Faculty of Geography, Leninskie Gory 1, Moscow, 119991, Russia*

As the direct measurements for the mass balance estimation can be applied only for a limited number of glaciers, alternative methods of estimation need to be developed. One of the most promising approaches is physically-based modelling, that is now being applied globally. In this study the mass balance of the Sary-Tor valley glacier was reconstructed for the period of 2003–2016. Originally developed for the North Caucasus AMelt model was modified to fit the conditions of continental glaciers. A block of snowpack processes was added to the model, including: head conductivity in the snowpack and in the active layer, water filtration in the snowpack and firn, congelation and regelation. The modelling results were verified using: 1) direct measurements on the ablation stakes net; 2) mass balance estimation according to geodetic method. The calibration parameters are compared to their measured values. Contrasting modeled mass-balance components for 2003–2016 and measured in 1985–1989 provided possibility to reveal climatically induced change of the Sary-Tor glacier dynamics.

Keywords: mass balance modelling, glaciers, Tien Shan, AMelt model.

INTRODUCTION

Glaciers are one of the key indicators of climate change and an important source of fresh water, especially in mountains surrounded by arid areas [Kaser *et al.*, 2010; Carey *et al.*, 2017; McDowell *et al.*, 2019]. In Central Asia, the population of the foothills is highly dependent on water flowing from the mountains [Lutz *et al.*, 2013]. The situation with freshwater resources is complicated by disputes between water-donor countries (Kyrgyzstan, Tajikistan) and water-consumer countries (Turkmenistan, Uzbekistan, and, to a lesser extent, Kazakhstan) [Zhupankhan *et al.*, 2017]. The former are mainly interested in using water to generate electricity in the winter time, whereas the latter need water for irrigation farming in the summer. According to recent estimates, more than 20 million people in Kazakhstan, Turkmenistan, and Uzbekistan depend on irrigated agriculture [Siegfried *et al.*, 2012].

Glaciers play a significant role in the runoff of the main rivers of Central Asia. According to [Sorg *et al.*, 2012], more than two dozen studies are devoted to estimates of the contribution of glacial runoff to the river flow in Central Asia. On average, it is estimated at about 15 % for rivers of Kyrgyzstan. Glacial runoff is defined as the total runoff from the glacier, including water from melting ice, firn, and snow and rainwater runoff. The contribution of glaciers to river runoff increases by 1.5–3 times in summer, up to 50 % for the Amu Darya River, 27 % for the rivers of the Lake Issyk-Kul basin, and 80 % for the Tarym River.

The contribution of glacial runoff to the Amu Darya River runoff is estimated at about 40 % in August and 25 % in July [Armstrong *et al.*, 2019]. From the standpoint of the formation of river runoff, the widespread reduction in the area of the Tien Shan glaciers [Narama *et al.*, 2010; Bolch *et al.*, 2019] is still compensated by an increase in ablation [Aizen *et al.*, 2007; Huss, Hock, 2018]. It is expected that the continuing reduction in the area of glaciation will lead to a decrease in river runoff in summer [Sorg *et al.*, 2012, 2014; Huss, Hock, 2018]. Detailed studies of glaciers in Central Asia will make it possible to reduce the errors of scenarios of changes in water resources in the future [Unger-Shayesteh *et al.*, 2013; Sorg *et al.*, 2014] and will contribute to ensuring the water security of the region. Obviously, in order to predict correctly the evolution of glaciers, the detailed information on the response of glaciers to current and past climate changes is required [Kronenberg *et al.*, 2016].

Such information can be provided both by direct observations of the mass balance and by modeling the mass balance of the glacier. After the collapse of the Soviet Union, all observations of the mass balance in the Tien Shan, Alai, and Pamir territories within the borders of the former USSR were curtailed (with the exception of Kazakhstan). They have been resumed only recently (<https://wgms.ch>). Mathematical modeling of the components of the mass balance of glaciers is used to solve a wide range of problems. There are models designed to carry out calculations on a

scale of whole mountain systems and for global generalizations [Bliss et al., 2014; Huss, Hock, 2015, 2018; Shea, Immerzeel, 2016; Shannon et al., 2019] and models with a more detailed description of the processes applicable to individual glaciers and glacial regions [Klok, Oerlemans, 2002; Lehning et al., 2006; Ayala et al., 2017]. Mathematical modeling was previously used to model the mass balance of individual glaciers in Kyrgyzstan – the Abramov Glacier [Barandun et al., 2015], Glacier no. 354 [Kronenberg et al., 2016], and the Suek West Glacier [Kenzhebaev et al., 2017]. The mathematical model of the Sary-Tor glacier was constructed in [Rybak et al., 2019] to carry out numerical experiments in order to study the possible evolution of glacier characteristics under different scenarios of climate change.

Reconstruction of the mass balance of the Sary-Tor Glacier for various periods was previously carried out on the basis of the relationship between the mass balance and the Equilibrium line altitude (ELA) [Ushnurtsev, 1991; Mikhalenko, 1993], as well as on the empirical dependences of the mass balance components on meteorological predictors [Popovnin et al., 2021].

The objectives of this study are: (1) to construct the mass balance model of the Sary-Tor Glacier (Ak-Shiyrak massif, Inner Tien Shan), basing on the spatially distributed energy-balance AMelt model [Rets et al., 2011]; (2) to reconstruct the glacier mass balance for 2003/04 to 2015/16 balance years; (3) to verify the results of modeling using in-situ data and geodetic mass balance, and (4) to analyze changes in the mass balance of the glacier in comparison with the period of 1985–1989 [Dyurgerov, 1995].

STUDY AREA

The Sary-Tor Glacier is a valley glacier in the upper reaches of the Naryn River within the Ak-Shiyrak massif. In 2018, the glacier area was 2.63 km² (Fig. 1) [Shpuntova et al., 2019]. The Ak-Shiyrak massif is characterized by a continental climate, which is mainly manifested in the frequent recurrence of air masses of the continental type and a small amount of atmospheric precipitation. In the annual distribution of precipitation, the summer maximum is well pronounced: on average, 70–80 % of the annual precipitation fall from May to September [Dyurgerov, 1995]. The mean annual precipitation according to records of the nearest Kumtor weather station (3659 m a.s.l.) is 317 mm [Petraikov et al., 2016]. At altitudes of about 4000 m, more than 90 % of the annual precipitation is in the solid form [Voloshina, 1988].

The Sary-Tor Glacier was recognized as a reference glacier for the Ak-Shiyrak massif and was the object of mass balance monitoring in 1985–1991. In 2014, the mass balance measurements on the Sary-Tor Glacier were resumed by the Institute of Water Problems and Hydropower of the National Academy of Sciences of Kyrgyzstan.

METHODS AND INITIAL DATA

Brief description of modeling approaches

To model the mass balance of the Sary-Tor glacier, the AMelt model of snow and ice melting in alpine basins was used. This energy-balance model with distributed parameters was suggested by E.P. Rets with co-authors [2011]. It implies the solution of the



Fig. 1. Location of the Sary-Tor Glacier, other considered glaciers, and the Kumtor weather station.

energy balance equation at each point of the computational grid:

$$-\omega = (S_b + S_{df})(1 - A) + E_{lrd} - E_{lru} \pm H \pm LE \pm Q_m \pm Q_{snp} \pm Q_{act},$$

where ω is the energy balance of the surface, W/m^2 ; S_b , S_{df} is the incoming direct and diffuse short-wave radiation, respectively, W/m^2 ; A is the surface albedo; E_{lrd} is the counter radiation of the atmosphere, W/m^2 ; E_{lru} is the long-wave radiation of the earth's surface, W/m^2 ; H is the sensible turbulent heat exchange with the atmosphere, W/m^2 ; LE is the latent turbulent heat exchange with the atmosphere, W/m^2 ; Q_m is the heat flux through the debris cover, W/m^2 ; Q_{snp} is the energy change due to processes in the snowpack and at the snow/ice interface, W/m^2 ; and Q_{act} is the energy change due to processes in the active layer of ice and firn, W/m^2 .

All calculated values are distributed over the cells of a regular grid.

To separate the incoming short-wave radiation (S_g) into direct (S_b) and diffuse (S_{df}) radiation, the following dependency [Bindi *et al.*, 1992; Boland, Ridley, 2008] is used:

$$S_{df}/S_b = f(k), k = S_g/S_o,$$

where k is the transparency coefficient of the atmosphere, and; S_o is the shortwave radiation at the upper boundary of the atmosphere.

The spatial distribution of the incoming short-wave radiation at a grid cell at each time point is based on:

- the angle of incidence of sun rays, calculated from the height of the sun above the horizon and the coordinates of the normal vector to the surface of the i -th elementary area centered at the grid cell;
- the angle of closure of the horizon by the surrounding relief of the surface of the i -th elementary area centered at the grid cell in the j -th sector of the horizon, corresponding to the current azimuth of the sun for each time step.

Diffuse solar radiation arriving at the surface of the i -th elementary area centered at the grid cell (S_{df_i}) consists of diffuse short-wave radiation coming from the visible part of the sky and re-reflected from the surrounding area:

$$S_{df_i} = S_{df_0}(1 - \bar{a}_i) + \bar{a}_i A_i'' S_{g_i}'',$$

where S_{df_0} is the scattered radiation flux at a fully open sky, W/m^2 ; \bar{a}_i is the average proportion of the closure of the firmament by the surrounding relief on the i -th elementary area; A_i'' is the albedo of the surrounding area of the i -th elementary area; and S_{g_i}'' is the total short-wave radiation arriving at the surface of the i -th elementary area, W/m^2 .

The albedo of the surface of the i -th elementary area is determined in accordance with the type of its surface. The albedos of melting snow, ice, firn and debris are set as constants based on field measurements and literature sources. In case of snowfall, the albedo increases to the albedo of fresh snow, then exponentially decreases to the albedo of melted snow, depending on the time elapsed since the last snowfall [Rohrer, Braun, 1994].

Long-wave surface radiation (E_{lru}) is calculated using the Stefan–Boltzmann equation. The counter radiation of the atmosphere (E_{lrd}) is calculated using the Angstrom formula. Turbulent heat exchange with the atmosphere (latent and sensitive heat fluxes) is calculated using the empirical formula of P.P. Kuzmin [1961].

The model was previously tested for the Djankuat and Bashkara glaciers (North Caucasus) [Rets, Kireeva, 2010; Rets *et al.*, 2011, 2014; Belozero *et al.*, 2020] and the Grenfjord glacier (Spitsbergen) [Elagina *et al.*, 2021]. Comparison of the simulation results with the results of direct observations on the network of ablation stakes attested to a good reproducibility of the results of field observations by the model.

The model was originally developed for the conditions of the North Caucasus [Rets *et al.*, 2011] and had to be adapted for the climatic conditions of Central Asia. The model was supplemented with the blocks of water filtration through the snowpack and firn; water refreezing in the snowpack, at the snow/ice boundary, and in the firn; and the heat transfer in the active layer of the glacier. The snowpack in the design scheme was presented as a system of layers, between which the heat transfer and the gravitational filtration of water took place. Also, the calculation of melt water yield per unit area of the glacier was added.

In the modified version of the model, the snowpack is divided into layers. The snow layers have a fixed thickness h (specified in mm by the StepTprof parameter), except for the top layer, the thickness of which is variable: it increases with fresh snow falling and decreases with melting. If the increasing thickness of the top layer reaches the StepTprof value, another layer is added to the snowpack. If the thickness of the top layer becomes zero, the snowpack becomes reduced by one layer.

In this version of the AMelt model, the vertical precipitation gradient (dP , %/100 m), which is a calibrated parameter, is used to describe the spatial distribution of liquid precipitation. When precipitation falls at an air temperature of less than -2 °C, it is considered that precipitation falls in solid form at each point of the grid cell.

Each layer has a set of characteristics that are averaged for a given layer: T – temperature, °C;

c – heat capacity, J/(kg·°C); H_w – gravitational water content, mm; Θ_{vir} – capillary water content, mm; ρ_{sn} – snow density, g/cm³; λ_{sn} – coefficient of molecular thermal conductivity of snow, W/(m·K).

The initial values of the snow density and the gravitational and capillary water contents are set the same for all snow layers, based on the available observation results, the archived data for adjacent areas and the theoretical concepts [Konovalov, 1985; Singh, 2001; Seo et al., 2008].

The heat capacity of snow is calculated from the heat capacity of ice, air and water in accordance with the density of snow and the content of gravitational and capillary water. The coefficient of thermal conductivity of the snow layer is calculated at each time step using its dependence on the density of snow [Sturm et al., 1997].

The initial temperature distribution in the snow stratum is set as uniform, equal to the mean air temperature for January–February.

In the extended version of the AMelt model, the change in the temperature of the snow layers occurs in the process of molecular heat transfer between the snow layers and heat release during the refreezing of infiltrated melt water into this layer.

1. Molecular thermal conductivity is calculated layer by layer as:

$$Q_{ij} = \lambda_{snij} (T_i - T_j) / dh,$$

where Q_{ij} is the heat flux due to molecular thermal conductivity between snow layers i and j , W/m²; λ_{snij} is the coefficient of thermal conductivity of snow averaged for layers i and j , W/(m·K) and given as a function of snow density [Sturm et al., 1997]; T_i is the temperature of the i -th layer of snow, °C; T_j is the temperature of the j -th layer of snow, °C; and dh is the distance between snow layers, m.

2. The release of heat inside the layer during the refreezing of infiltrating melt water into this layer (Q_{Lm} , W/m²) is calculated as:

$$Q_{Lm} = Lm,$$

where L is the specific heat of fusion of ice ($3.335 \cdot 10^5$ J/kg); m is the mass of refreezing water, kg.

Infiltration is calculated from an adapted version of Darcy's law [DeWalle, Rango, 2008; Snow..., 2008]. The infiltration rate u_w is given as a function of the ρ_{sn} , the average grain diameter d , the proportion of gravitational water in the snow pores S_w , and the water-holding capacity Θ_{vi} :

$$u_w = f(\rho_{sn}, d, S_w, \Theta_{vi}).$$

The water-holding capacity of snow (in fractions of a unity) is calculated from its dependence on the porosity of the snow p [Coleou, Lesaffre, 1998]:

$$\Theta_{vi} = 0.057p / (1 - p) + 0.017.$$

The porosity of the snow is calculated approximately from the snow density as $(1 - \rho_{sn})$.

The density of the snow layer increases in the course of refreezing of infiltration water. In this case, the snow density is calculated at each step as:

$$\rho_{sn}^t = \left(\rho_{sn}^{t-1} h + 0.917 (H_w^t + \Theta_{vir}^t) \right) / (h + H_w^t + \Theta_{vir}^t).$$

The density of the newly accumulated fresh snow layer is set by the RoFreshSnow parameter.

If the thickness of the top snow layer is less than 0.7 StepTprof, then it is combined with the underlying snow layer or with the surface ice layer (if this is the only snow layer) during the layer-by-layer calculation of thermal conductivity.

The active layer of the glacier is also divided into layers, the number of which is set by the nLIce model parameter. Heating/cooling of the active layer of ice proceeds due to molecular thermal conductivity; an additional source of thermal energy is the refreezing of water on the surface of ice at a temperature below the melting point. The initial temperature distribution in the active ice layer is linear: from the surface layer, the initial temperature of which is equal to the mean January–February temperature, to the bottom of the active layer with a constant temperature specified by the Tact parameter.

Water loss from the firn occurs after the cold content (CC) condition of the firn is satisfied [Takeuchi et al., 2014].

The filtration coefficient for describing the process of water filtration through the firn was adopted according to the published data of experimental measurements by various scientific groups [Oerter, Moser, 1982].

The modeled accumulation values include the total accumulation, as well as the refreezing of melt water in the snow stratum, on the ice surface, and in the firn layer. Avalanche feeding is not taken into account in this version, since it is practically absent for the object under study due to the features of the relief. Wind redistribution of solid precipitation is taken into account indirectly, considering the position of the firn line: for areas above the firn line of a given year, an additional coefficient is applied to the altitudinal increase in precipitation. For the Sary-Tor glacier, in the areas above the firn line, the value of precipitation additionally increases by 30 %.

Adaptation of the AMelt model for the Sary-Tor Glacier

The following input data were used to build a model of the Sary-Tor glacier:

1) a digital elevation model composed of a highly detailed model obtained for the surface of the Sary-Tor Glacier from a GeoEye stereoscopic pair (July 29, 2012) and an SRTM model for the surrounding landforms;

2) meteorological data with a 1 h resolution for 2003–2016 from the automatic weather station (AWS) Campbell located less than 5 km from the gla-

cier at the height of 3659 m asl, including incoming shortwave radiation (S_g , W/m^2), air temperature ($T(H)$, $^{\circ}C$), wind speed (U , m/s), relative air humidity (e , %), and precipitation (P , mm) (provided by the Kumtor Gold Company);

3) the position of the firn line and glacier boundaries for each year as determined from Landsat images;

4) field data on melting regime as measured in 2015 on a network of ablation stakes was used for model calibration;

5) field data on melting regime as measured in 2014 on a network of ablation stakes was used for model validation.

In the model adapted for the Sary-Tor Glacier, the heat flux through the debris cover was not taken into account, since there is practically no debris cover on the glacier.

The albedo values of ice, firn, melted snow, and freshly fallen snow were taken as 0.25, 0.4, 0.55, and 0.8, respectively, according to the averaged results obtained by D.A. Petrakov with coauthors in the studied region [Petrakov *et al.*, 2019].

As we had no data on air temperatures and precipitation, as well as on the snow depths at different heights during the modeled period, the altitudinal gradients of precipitation and air temperature were calibrated.

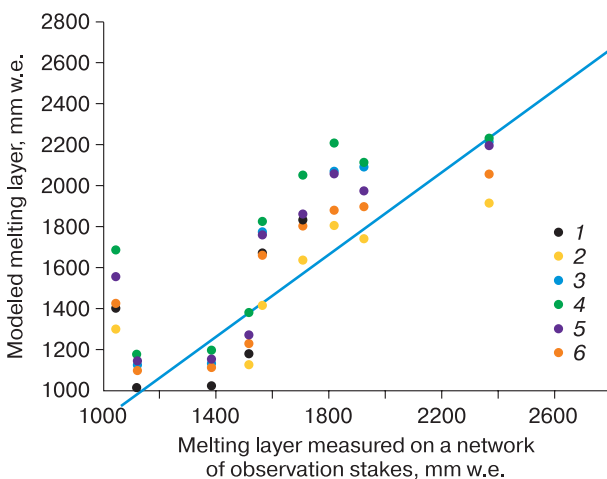


Fig. 2. Calibration of the Sary-Tor Glacier model according to the results of field measurements on a network of ablation stakes in 2015.

Blue line – linear approximation function. Results of model experiments with different values of calibration parameters of air temperature (dP , precipitation gradient; dT , temperature gradient; t_{sh} , temperature shift); 1 – $dP = 20\%/100\text{ m}$, $dT = -7\text{ }^{\circ}C/1000\text{ m}$, $t_{sh} = 0\text{ }^{\circ}C$; 2 – $dP = 20\%/100\text{ m}$, $dT = -6\text{ }^{\circ}C/1000\text{ m}$, $t_{sh} = 1\text{ }^{\circ}C$; 3 – $dP = 20\%/100\text{ m}$, $dT = -5.5\text{ }^{\circ}C/1000\text{ m}$, $t_{sh} = 0.5\text{ }^{\circ}C$; 4 – $dP = 20\%/100\text{ m}$, $dT = -5\text{ }^{\circ}C/1000\text{ m}$, $t_{sh} = 0.5\text{ }^{\circ}C$; 5 – $dP = 20\%/100\text{ m}$, $dT = -5\text{ }^{\circ}C/1000\text{ m}$, $t_{sh} = 0.75\text{ }^{\circ}C$; 6 – $dP = 20\%/100\text{ m}$, $dT = -5\text{ }^{\circ}C/1000\text{ m}$, $t_{sh} = 1\text{ }^{\circ}C$.

The best agreement of the model data with the field data for all altitudinal zones was obtained at a temperature gradient of $-7\text{ }^{\circ}C$ per 1000 m, a temperature shift equal to $0\text{ }^{\circ}C$, and a precipitation gradient of 20% per 100 m. The choice of these parameters is analyzed in the Discussion section. In this case, the deviation of the simulated values from the measured values in different parts of the glacier may be associated with spatial differences in the temperature regime and the distribution of snow, which cannot be described by a constant gradient (Fig. 2).

The simulation results were validated using two independent methods:

1. Comparison of the results of modeling with the field data obtained in 2014, which demonstrated a good agreement between them (Fig. 3). The correlation coefficient was 0.99. The Nash-Sutcliffe model efficiency coefficient (NSE) for 2014 was 0.95 [Garriock *et al.*, 1978]. A small systematic deviation was noted: the model overestimated the melting in the middle and lower zones of the glacier by about 0.05–0.1 m w.e. (meters of water equivalent).

2. Comparison of the change in the average surface height of the Sary-Tor Glacier from July 29, 2003 to September 29, 2013 as determined from the analysis of stereoscopic pairs of QuickBird and GeoEye satellite images [Petrakov *et al.*, 2016] with the total modeled mass balance of the glacier for this period. The average decrease in the surface height was 3.8 m according to the geodetic method and 4.3 m according to the modeling. The deviation of the simulation results from the measured data was 13 % over the 10 mass balance years, or 0.05 m per year. Thus, we can say that the simulation by the AMelt model reliably represents the dynamics of the mass balance of the glacier.

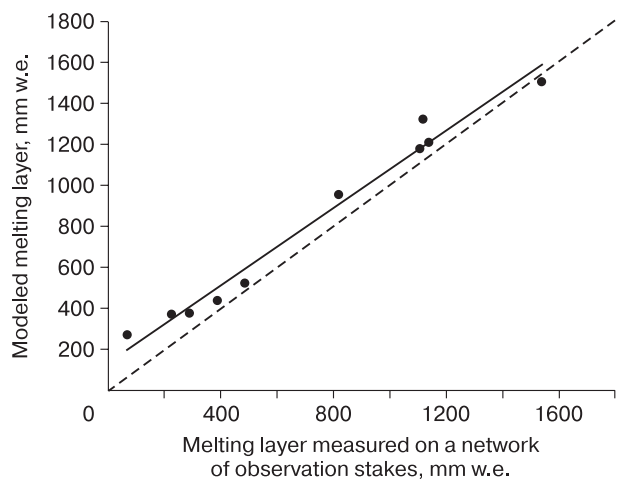


Fig. 3. Verification of the model based on the results of field observations on a network of ablation stakes on the Sary-Tor Glacier in 2014.

Dashed line: graph $y = x$; solid line: linear approximation function.

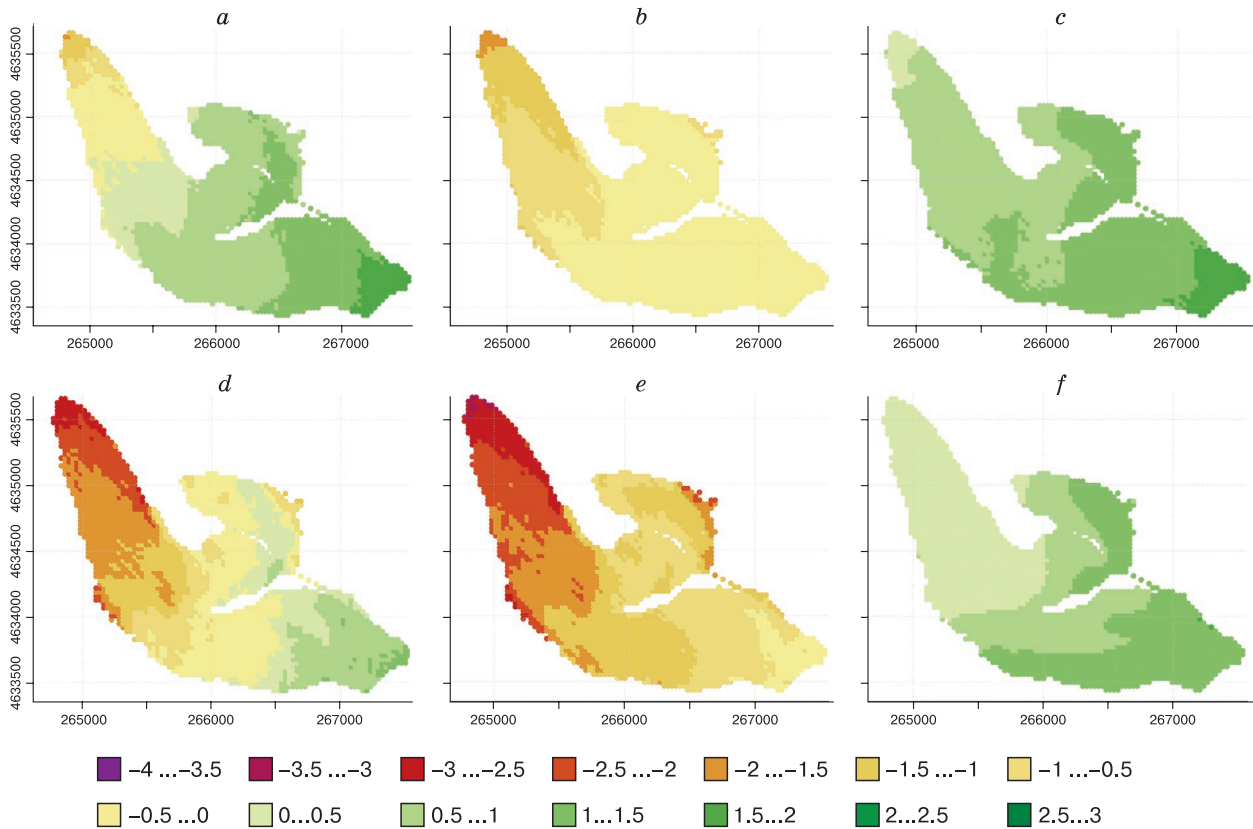


Fig. 4. Schematic maps of mass balance fields of the Sary-Tor Glacier for glaciological years of (a, b, c) 2008/09 and (d, e, f) 2014/15: (a, d) mass balance Bal; (b, e) surface lowering due to ablation Abl; and (c, f) accumulation Acc.

The color shows the change in the surface height, m w.e.

Table 1. Annual values of the mass balance (Bal), ablation (Abl), and accumulation (Acc) of the Sary-Tor Glacier according to modeling data

Mass balance year	Bal	Abl	Acc
	m w.e.		
2003/04	-0.44	1.03	0.59
2004/05	-0.52	0.99	0.48
2005/06	-0.71	1.24	0.54
2006/07	-0.47	1.09	0.62
2007/08	-0.63	1.10	0.46
2008/09	0.37	0.53	0.89
2009/10	-0.62	1.34	0.72
2010/11	-0.37	1.05	0.68
2011/12	-0.56	1.24	0.68
2012/13	-0.36	0.98	0.62
2013/14	-0.50	0.96	0.46
2014/15	-0.76	1.42	0.67
2015/16	-0.48	1.09	0.61
Average value	-0.463	1.08	0.618

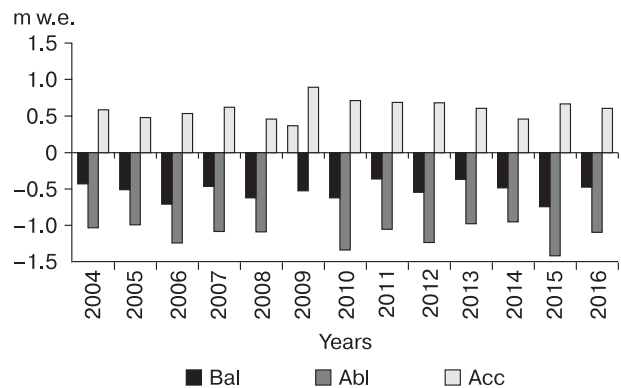


Fig. 5. Accumulation (Acc), change in the height of the glacier surface due to ablation (Abl), and mass balance (Bal) of the Sary-Tor Glacier for the period 2003/04–2015/16 according to the modeling.

RESULTS

The output of the model is the depth of snow, firn, and ice melt and corresponding water yield calculated for each point of the regular grid (30×30 m) at each time step (in this work, 1 h). Examples of the spatial distribution of the total values of ablation, accumulation, and mass balance of the Sary-Tor Glacier calculated for the mass balance year are shown in Fig. 4. According to the model, the annual accumulation on the Sary-Tor Glacier varies from 0.48 to 0.89 m w.e. in different years, and the ablation changes from 0.53 to 1.42 m w.e. (Table 1 and Fig. 5). For most of the years during the study period, the glacier mass balance is negative and averages -0.46 m w.e. per year. With regard to mass balance, the only positive year was 2009 because of the low ablation and increased accumulation.

DISCUSSION

Despite the fact that the AMelt model is focused on physically-based simulation of snow and ice melting, the lack of complete information about the simulated objects necessitates the use of calibration parameters: the gradients of temperature and precipitation in this case. The problem of the presence of calibration parameters in hydrological models has long been known and widely discussed [Christophersen *et al.*, 1990; Beven, Freer, 2001; Kirchner, 2006; Vinogradov, Vinogradova, 2010; Semenova, Beven, 2015]. When calibrating, the modeler strives to achieve, first of all, the correspondence of the main sought parameter (in the case of hydrological modeling, the runoff in the outlet; in the case of glaciological modeling, the final mass balance) to the observational data. It is important that the same satisfactory result can be obtained using different independent sets of values, i.e., calculations with different initial values in hydrological modeling are equifinal. Moreover, the values of the calibration parameters can go beyond their physical limits for a given object and lose their physical meaning. Accordingly, in the course of model calibration, the mechanisms of the simulated process can be significantly distorted.

In accordance with this, the authors consider it appropriate to analyze the selected values of the calibration parameters (see the Methods and data section), as well as the results of modeling individual components of the dynamics of the Sary-Tor Glacier mass balance, for which observational data can be found for comparison.

The altitudinal temperature gradient was taken equal to -7 °C per 1000 m, and the altitudinal precipitation gradient was 20 % per 100 m. The representation of the vertical distribution of air temperature and precipitation as a linear function with a constant

slope is a significant simplification. In reality, the vertical distribution of these parameters in the mountains is not described by a linear function; it is strongly affected by local factors and changes significantly both during the entire season and during one day [Barry, 2008].

The results of simultaneous observations over the air temperature at the Tien Shan weather station (it was located in the same trough valley as the modern Kumtor weather station, 9 m lower) and in the middle part of the ablation zone on the Davydov Glacier (which occupies the neighboring valley) in July–August 1984 were presented in the study by A.P. Voloshina [1988]. In summer, during the daytime in clear weather, the air temperature at the weather station can exceed the air temperature in the middle part of the ablation zone on the glacier by 4–6 °C, while temperature inversions are usually observed at night. On average, the recorded difference in air temperatures between the two points was 1.6–2.6 °C, which corresponded to a temperature gradient of 5.5–8.9 °C per 1000 m; on average, -7.2 °C per 1000 m. This value turned out to be extremely close to the calibration parameter of the temperature gradient, which gave the best fit of the simulated melting to the results of factual measurements at the Sary-Tor Glacier.

The work [Voloshina, 1988] also contained data on simultaneous measurements of precipitation at the same points. The magnitude of the precipitation gradient, according to the observation results, depended on the amount of precipitation at the height of the weather station: with an increase in the amount of precipitation, the gradient decreased exponentially, settling at a level of 25–30 % per 100 m with the amount of precipitation equal to 3 mm or more.

Thus, the precipitation gradient adopted in the model (20 % per 100 m) may be somewhat underestimated, but it is close to the values typical for this region.

The altitudinal distribution of solid precipitation on a glacier is determined by a combination of the altitudinal distribution of liquid precipitation and air temperature.

According to [Dyurgerov *et al.*, 1992], the altitudinal gradient of solid precipitation during summer snowfalls in 1987–1989 was variable. It usually increased with an altitude from 0–20 % per 100 m in the lower glacier zones to 40–100 % per 100 m at the height of 4200–4400 m a.s.l., and decreased to 10–40 % at the heights above 4400 m a.s.l. The average value of the altitudinal gradient of solid precipitation was 46 % per 100 m. The simulated altitudinal distribution of annual precipitation and accumulation is relatively even because of constant temperature and precipitation gradients: the accumulation gradients increase from 20–40 to 40–100 % per 100 m; this

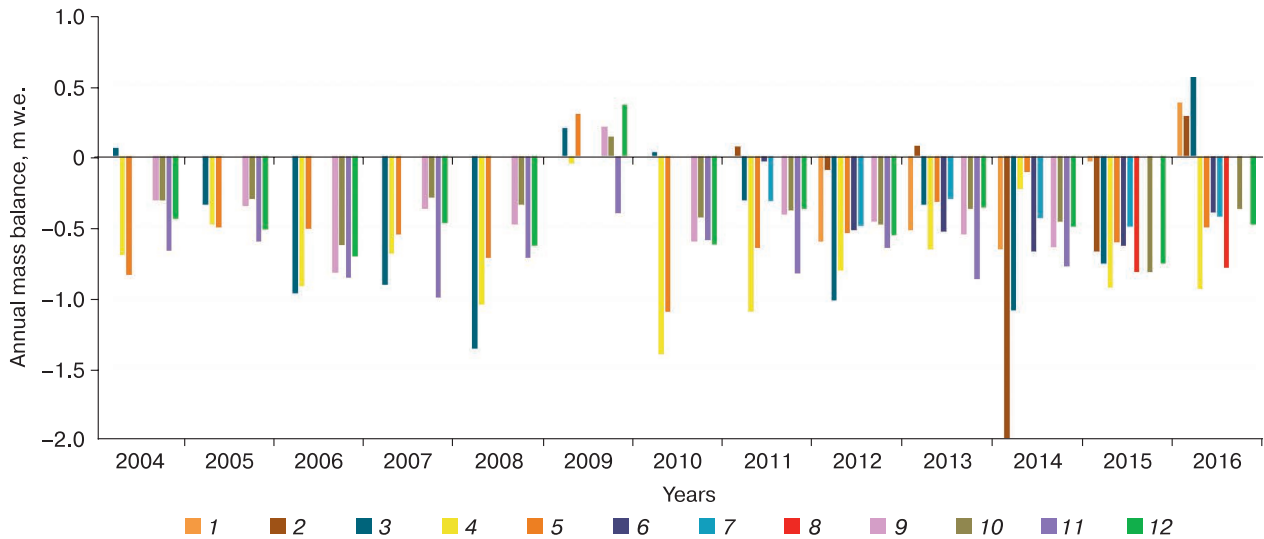


Fig. 6. Annual values of the mass balance on the Tien Shan glaciers in the period from 2003/04 to 2015/16 balance years.

According to the glaciological method (<https://wgms.ch/>): 1 – Abramov Gl, 2 – Golubev Gl, 3 – Tuyuksu Gl, 4 – Glacier no. 1 Urumqi, eastern branch; 5 – Glacier no. 1 Urumqi, western branch; 6 – Glacier no. 354; 7 – Western Suek Gl, and 8 – Sary-Tor Gl. Mass balance reconstruction: 9 – Glacier no. 354 [Kronenberg et al., 2016], 10 – Western Suek Gl [Kenzhebaev et al., 2017], 11 – Sary-Tor Gl [Popovnin et al., 2021], and 12 – Sary-Tor Gl (present study).

gradient decreases at the altitude above 4400 m. The average simulated accumulation gradient is 52 % per 100 m. It can be stated that the model simplifies the real field of snow distribution due to the simplified consideration of the vertical distribution of temperature and precipitation.

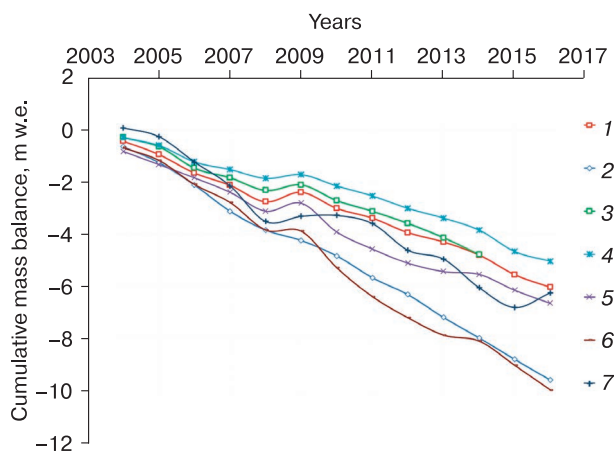


Fig. 7. Comparison of cumulative mass balance curves for Tien Shan glaciers.

According to modeling data: 1 – Sary-Tor Gl (present work); 2 – Sary-Tor Gl (reconstruction based on empirical dependences on meteorological predictors [Popovnin et al., 2021]); 3 – Glacier no. 354 [Kronenberg et al., 2016]; 4 – Western Suek Gl [Kenzhebaev et al., 2017]. According to the glaciological method (<https://wgms.ch/>): 5 – Glacier no. 1 Urumqi, western branch; 6 – Glacier no. 1 Urumqi, eastern branch; and 7 – Tuyuksu Gl.

According to the modeling data, the mass balance of the Sary-Tor Glacier in 2004–2016 repeated the trends observed on the Tien Shan glaciers according to the data of direct observations and reconstructions by various authors (Figs. 6 and 7). For most of the glaciers, a positive mass balance was observed in 2009. The simulated annual mass balance values of the Sary-Tor Glacier fit into the range of measured and modeled elsewhere mass balance values of the Tien Shan glaciers (Fig. 6). The obtained annual values are closest to the measured and modeled values reported for the nearby glaciers no. 354 and Western Suek.

The mass balance of the Sary-Tor Glacier simulated for 2015 demonstrated a good agreement with the mass balance determined by the glaciological method (-0.76 and -0.82 m w.e., respectively). In 2016, the discrepancy between the simulated and factual (glaciological method) mass balances was 0.31 m w.e. (-0.48 and -0.79 m w.e., respectively). The differences may be associated primarily with the different methodology for extrapolating the values of the glacier mass balance to the area, for which observational data are absent, or with errors of both the glaciological method (estimated at about 0.2 m w.e. for this region [Kronenberg et al., 2016; Kenzhebaev et al., 2017]) and the modeling method. For the present model, the average error in calculating the annual balance is approximately 0.1 m w.e. (see the Results section). It should also be noted that the values of the modeled and experimentally determined mass ba-

lance of the Sary-Tor Glacier in 2015 (-0.76 and -0.82 m w.e., respectively) are within the range of the mass balance values observed for most of the glaciers in the region (from -0.499 to -0.93 m w.e.), except for the Abramov Glacier with a mass balance close to zero in that year (<https://wgms.ch/>). In 2016, the loss of mass of glaciers in the region was less significant than in 2015: from -0.37 to -0.5 m w.e. (the exception was Urumqi, the eastern branch). For many glaciers, the mass balance was even positive (from 0.287 to 0.561 m w.e.) (<https://wgms.ch/>). Thus, the modeled value of the mass balance of the Sary-Tor Glacier for 2016 (-0.48 m w.e.) was closer to the regional distribution than that obtained by the glaciological method (-0.79 m w.e.).

In general, according to the obtained results, the mass of the Sary-Tor Glacier decreases slower than that of the Urumchi and Tuyuksu glaciers, and faster than that of the Western Suek Glacier. The cumulative curve obtained from the reconstruction of the mass balance of glacier no. 354 [Kronenberg et al., 2016] is the closest to the one obtained for the Sary-Tor Glacier.

Reconstruction of the mass balance of the Sary-Tor Glacier based on empirical relationships between the components of the mass balance and the meteorological predictors [Popovnin et al., 2021] demonstrated good agreement with the results of our modeling for 2005, 2006, 2008, 2010, and 2012. In other years,

the values of the mass balance reconstructed from the empirical dependences on meteorological predictors were lower than those obtained with the help of the AMelt model (Fig. 6). As a consequence, the cumulative mass balance curve of the Sary-Tor Glacier obtained by the reconstruction method with the use of empirical dependences on meteorological predictors [Popovnin et al., 2021] lies significantly lower than the curve obtained in our study and closer to the curve obtained for the Tuyuksu Glacier (Fig. 7).

Comparison of the simulation results with observational data on the Sary-Tor Glacier in 1984/85–1988/89 [Dyurgerov et al., 1992; Dyurgerov, 1995] reveals the intensification of the glacier mass loss. The average value of the mass balance in the modern period (2003/04 to 2015/16) was -0.46 m w.e.; in 1984/85–1988/89, it was -0.14 m w.e. According to the reconstruction by S.N. Ushnurtsev [1991] based on the relationship between the mass balance and the height of the feeding boundary, the mass balance of the Sary-Tor Glacier in the period from 1930 to 1984 ranged from -0.6 to 0.2 m w.e. A similar tendency for the intensification of mass loss is observed for all Tien Shan glaciers provided with long-term observation series (Fig. 8).

The intensification of the loss of mass by the Sary-Tor Glacier occurred primarily due to the increased melting in the lower altitudinal zones. In the accumulation zone, the annual mass balance values

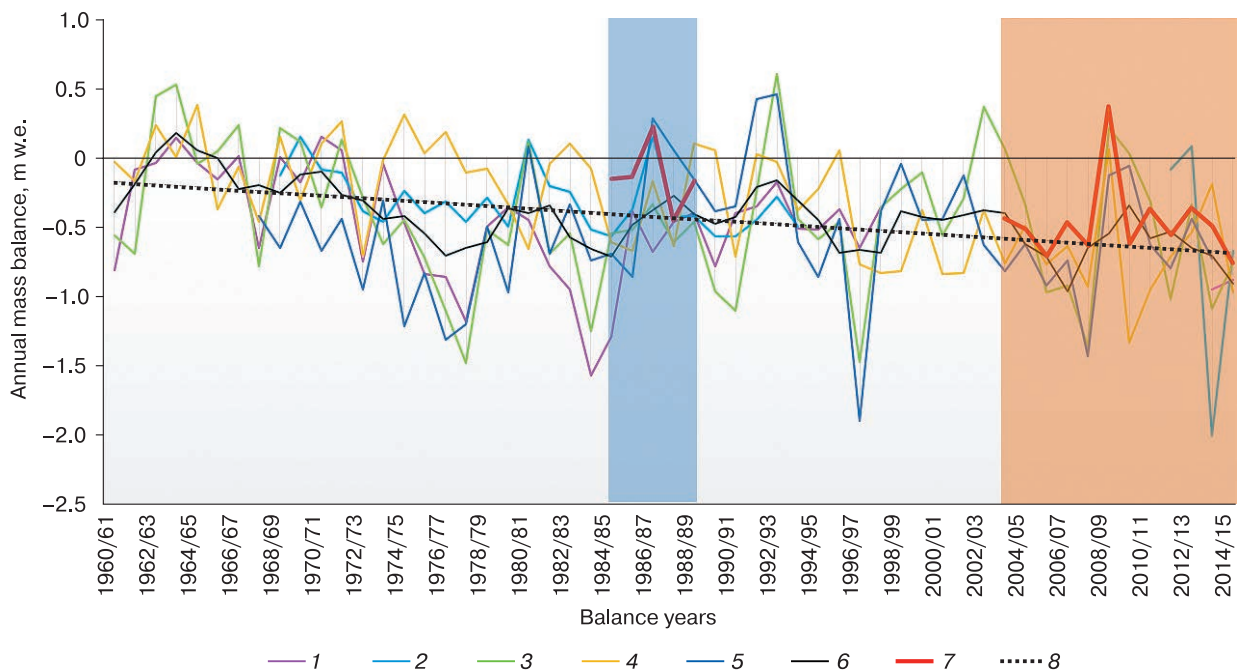


Fig. 8. Long-term fluctuations in the mass balance of the Tien Shan glaciers.

1 – Karabatkak Gl; 2 – Golubev Gl; 3 – Tuyuksu Gl; 4 – Urumqi Gl; 5 – Abramov Gl; 6 – moving average with a three-year window; 7 – Sary-Tor Gl (1984/85–1988/89, observation data [Dyurgerov, 1995]; 2003/04–2015/16, modeling data); 8 – linear approximation of a moving average with a three-year window. Graphs 1–5 are based on data from the Internet resource <https://wgms.ch/>.

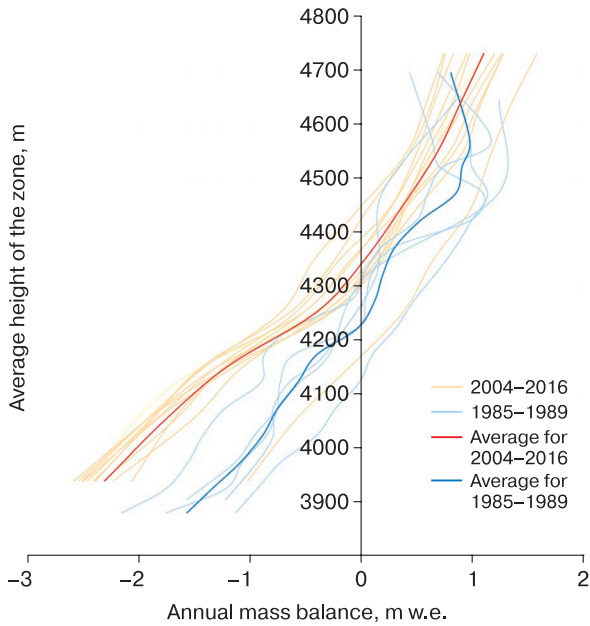


Fig. 9. Altitude distribution of the annual mass balance for the model period (2004–2016) and the period of field observations (1985–1989).

averaged over altitudinal zones for 1984/85–1988/89 and 2003/04–2015/16 are generally close: the ranges of variation coincide for both periods, and the average for the latter period is shifted towards more negative values by 0–0.25 m w.e. (Fig. 9). At the altitude below 4300 m asl, the averaged curves begin to diverge: at the altitudes of 3900–4000 m, melting in the recent period was 1.0–1.2 m w.e. higher than that in

the 1980s. The ELA shifted upwards by 125 m: from 4225 m in 1984/85–1988/89 to 4350 m in 2003/04–2015/16 with a range of variation from 4254 to 4446 m.

A smoother pattern of the altitudinal distribution of the mass balance in the model period compared to the period of field observations in the 1980s is associated with a simplified representation of the altitudinal distribution of precipitation and temperature. Spatial differences in the structure of the modeled values of the glacier balance are due to the distribution of solar radiation and the surface topography (Fig. 10).

The intensification of the ablation of glaciers in the Ak-Shyirak massif occurs against the background of an increase in the annual and summer air temperatures (Fig. 11, *a*). Thus, the air temperature of the warm (May–September) season in 1984/85–1988/89 at the Tien Shan weather station was +1.8 °C; in 2003/04–2015/16, it increased to +3.0 °C. The rise in temperature was not offset by a significant increase in the annual precipitation: from 288 mm in 1984/85–1988/89 to 373 mm in 2003/04–2015/16. An increase in precipitation was noted during the ablation period; there was no significant increase in precipitation during the accumulation period. The rise in temperature could have led to a significant decrease in the proportion of solid precipitation in the lower part of the glacier in the summer. In addition, the increase in precipitation could be related to the relocation of the weather station. The unevenness of the precipitation curve after the relocation of the station was noted in a number of studies [Kutuzov, Shahgedanova, 2009; Petrakov et al., 2016].

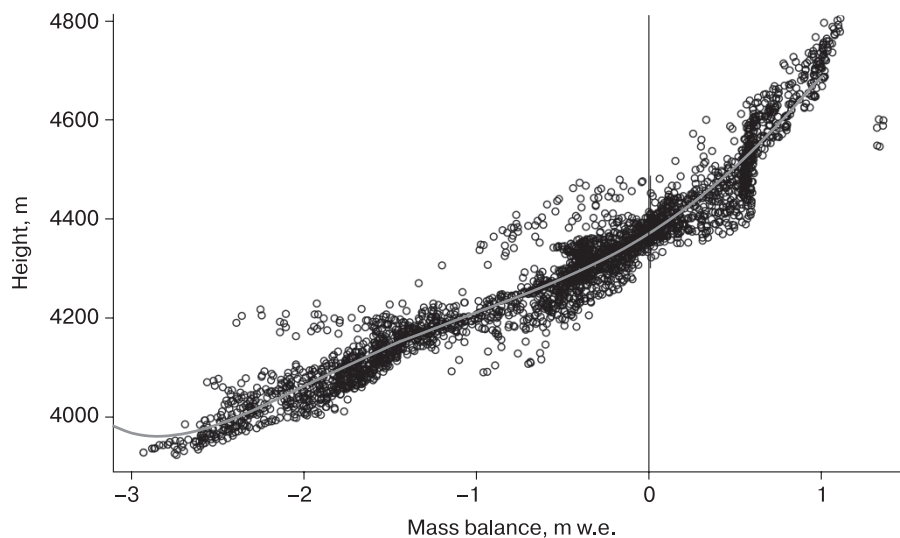


Fig. 10. Distribution of the annual mass balance depending on the absolute height according to the data of all grid cells of the model in 2014/15.

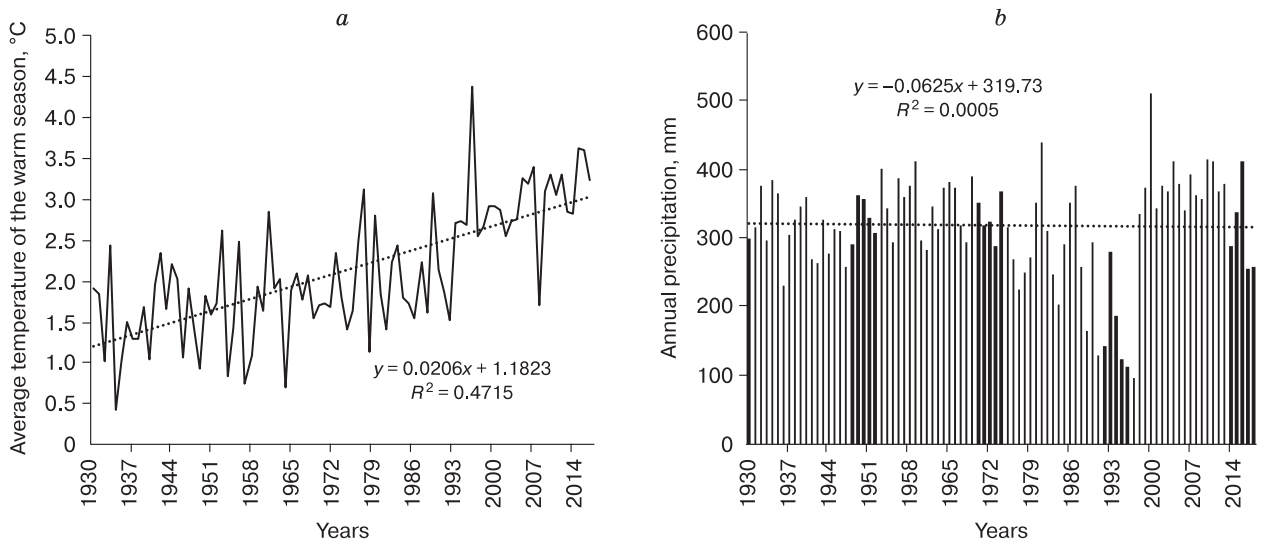


Fig. 11. Average air temperatures of the warm season (May–September) (a) and annual precipitation (b) according to the data of the Tien Shan and Kumtor weather stations for 1930–2018.

CONCLUSIONS

In this work, the physically based AMelt model of snow and ice melting in alpine zones was adapted to simulate the mass balance of glaciers under the climatic conditions of Central Asia. Approbation of an improved version of the model on the Sary-Tor Glacier for the period 2003/04 to 2015/16 demonstrated a good agreement with the results of glacial ablation measurements on a network of ablation stakes and the average subsidence of the glacier surface calculated using the geodetic method. The calibration coefficients (altitudinal gradient of temperature and precipitation) turned out to be close to the values observed in July–August 1984.

According to the modeling data, the annual accumulation values on the Sary-Tor Glacier in 2003/04–2015/16 varied within the range from 0.48 to 0.89 m w.e. and the ablation values, from –1.42 to –0.53 m w.e. The glacier mass balance was negative for most of the years during the study period and averaged –0.46 m w.e. per year. This value is significantly lower than the value observed in 1984–1989 (on average, –0.14 m w.e. per year). The ELA increased by 125 m: from 4225 in 1984/85–1988/89 to 4350 in 2003/04–2015/16. Such an intensification of mass loss is typical for all Tien Shan glaciers, on which mass balance observations have been performed.

According to modeling data, the dynamics of the mass balance of the Sary-Tor Glacier in the period from 2004 to 2016 repeats the trends noted for the Tien Shan glaciers according to direct observations and reconstructions by various authors. The obtained annual values of the mass balance are closest to the

measured and modeled values characteristic of the nearby glaciers no. 354 and Western Suek. In general, according to the obtained results, the Sary-Tor Glacier is melting slower than the Urumqi and Tuyuksu glaciers to the east and faster than the Western Suek glacier.

Acknowledgments. This work was supported by the grant of the President of the Russian Federation MK-2936.2019.5 in terms of modeling the mass balance of the Sary-Tor Glacier. The analysis of the problem of equifinality and the correspondence of the values of the calibrated parameters of the model to the observation data was supported by the Russian Foundation for Basic Research, project no. 20-35-70024. Selection and processing of remote sensing data and the analysis of the mass balance of the Tien Shan glaciers were carried out within the framework of state assignment no. AAAA-A16-116032810095-6. The analysis of long-term changes in the characteristics of the mass balance of the Sary-Tor Glacier was carried out within the framework of state assignment no. AAAA-A18-118022090056-0.

The authors are grateful to the Kumtor Gold Company for providing meteorological data.

References

- Aizen, V.B., Kuzmichenok, V.A., Surazakov, A.B., Aizen, E.M., 2007. Glacier changes in the Tien Shan as determined from topographic and remotely sensed data. *Glob. and Planet. Change* 56 (3–4), 328–340.
- Armstrong, R.L., Rittger, K., Brodzik, M.J., et al., 2019. Runoff from glacier ice and seasonal snow in High Asia: separating melt water sources in river flow. *Regional Environ. Change* 19 (5), 1249–1261.

- Ayala, A., Pellicciotti, F., Peleg, N., Burlando, P., 2017. Melt and surface sublimation across a glacier in a dry environment: Distributed energy-balance modelling of Juncal Norte Glacier, Chile. *J. Glaciol.* 63 (241), 803–822.
- Barandun, M., Huss, M., Sold, L., et al., 2015. Re-analysis of seasonal mass balance at Abramov glacier 1968–2014. *J. Glaciol.* 61 (230), 1103–1117.
- Barry, R.G., 2008. Mountain weather and climate. Cambridge Univ. Press, New York, 532 pp.
- Belozerov, E., Rets, E., Petrakov, D., Popovnin, V., 2020. Modelling glaciers' melting in Central Caucasus (the Djankuat and Bashkara Glacier case study). *E3S Web of Conferences*, 163, p. 01002. EDP Sciences.
- Beven, K., Freer, J., 2001. Equifinality, data assimilation, and uncertainty estimation in mechanistic modelling of complex environmental systems using the GLUE methodology. *J. Hydrol.* 249 (1–4), 11–29.
- Bindi, M., Miglietta, F., Zipoli, G., 1992. Different methods for separating diffuse and direct components of solar radiation and their application in crops growth models. *Clim. Res.* 2, 47–54.
- Bliss, A., Hock, R., Radić, V., 2014. Global response of glacier runoff to twenty-first century climate change. *J. Geophys. Res. Earth Surf.* 119 (4), 717–730.
- Boland, J., Ridley, B., 2008. Models of diffuse solar fraction. In: *Modeling Solar Radiation at the Earth's Surface*. V. Badescu (Ed.). Springer, Berlin, Heidelberg, pp. 193–219.
- Bolch, T., Shea, J.M., Liu, S., et al., 2019. Status and change of the cryosphere. In: *The Extended Hindu Kush Himalaya Region*. P. Wester, A. Mishra, A. Mukherji, A. Shrestha (Eds.). Springer, Cham., New York, pp. 209–255.
- Carey, M., Molden, O.C., Rasmussen, M.B., et al., 2017. Impacts of glacier recession and declining meltwater on mountain. *Societies, Ann. Amer. Assoc. Geogr.* 107 (2), 350–359.
- Christophersen, N., Neal, C., Hooper, R.P., et al., 1990. Modelling streamwater chemistry as a mixture of soilwater end-members – a step towards second-generation acidification models. *J. Hydrol.* 116 (1–4), 307–320.
- Coleou, C., Lesaffre, B., 1998. Irreducible water saturation in snow: experimental results in a cold laboratory. *Ann. Glaciol.*, No. 26, 64–68.
- DeWalle, D.R., Rango, A., 2008. Principles of snow hydrology. Cambridge Univ. Press, New York, 428 pp.
- Dyurgerov, M.B., Kunakhovich, M.G., Mikhaleiko, V.N., et al., 1992. Mass balance, runoff and meteorological conditions of the Sary-Tor glacier in the Ak-Shyirak ridge (Inner Tien Shan) 1985–1989. *IGRAN, Moscow*, 69 pp. (in Russian).
- Dyurgerov, M.B. (Ed.), 1995. Glaciation of the Tien Shan. *VINITI, Moscow*, 237 pp. (in Russian).
- Elagina, N., Kutuzov, S., Rets, E., et al., 2021. Mass balance of Austre Grønfjordbreen, Svalbard, 2006–2020, estimated by glaciological, geodetic and modeling approaches. *Geosciences* 11 (2), p. 78.
- Garrick, M., Cunnane, C., Nash, J.E., 1978. A criterion of efficiency for rainfall-runoff models. *J. Hydrol.*, No. 36, 375–381.
- Huss, M., Hock, R., 2015. A new model for global glacier changes and sea-level rise. *Front. Earth Sci.*, No. 3, p. 54.
- Huss, M., Hock, R., 2018. Global-scale hydrological response to future glacier mass loss. *Nat. Clim. Chang.* 8 (2), 135–140.
- Kaser, G., Grobhauser, M., Marzeion, B., 2010. Contribution potential of glaciers to water availability in different climate regimes. *Proc. Natl. Acad. Sci.* 107 (47), 20223–20227.
- Kenzhebaev, R., Barandun, M., Kronenberg, M., et al., 2017. Mass balance observations and reconstruction for Batysh Sook Glacier, Tien Shan, from 2004 to 2016. *Cold Reg. Sci. Technol.*, No. 135, 76–89.
- Kirchner, J.W., 2006. Getting the right answers for the right reasons: Linking measurements, analyses, and models to advance the science of hydrology. *Water Resources Res.* 42 (3), W03S04.
- Klok, E.L., Oerlemans, J., 2002. Model study of the spatial distribution of the energy and mass balance of Morteratschgletscher, Switzerland. *J. Glaciol.* 48 (163), 505–518.
- Konovalov, V.G., 1985. Melting and runoff from glaciers in the river basins of Central Asia. *Gidrometeoizdat, Leningrad*, 239 pp. (in Russian).
- Kronenberg, M., Barandun, M., Hoelzle, M., et al., 2016. Mass-balance reconstruction for Glacier No. 354, Tien Shan, from 2003 to 2014. *Ann. Glaciol.* 57 (71), 92–102.
- Kutuzov, S., Shahgedanova, M., 2009. Glacier retreat and climatic variability in the eastern Terskey-Alatau, inner Tien Shan between the middle of the 19th century and beginning of the 21st century. *Glob. and Planet. Change* 69, 59–70.
- Kuzmin, P.P., 1961. The process of melting snow cover. *Gidrometeoizdat, Leningrad*, 364 pp. (in Russian).
- Lehning, M., Völksch, I., Gustafsson, D., et al., 2006. ALPINE3D: a detailed model of mountain surface processes and its application to snow hydrology. *Hydrol. Process.* 20 (10), 2111–2128.
- Lutz, A.F., Immerzeel, W.W., Gobiet, A., et al., 2013. Comparison of climate change signals in CMIP3 and CMIP5 multi-model ensembles and implications for Central Asian glaciers. *Hydrol. Earth Syst. Sci.*, No. 17, 3661–3677.
- McDowell, G., Huggel, C., Frey, H., et al., 2019. Adaptation action and research in glaciated mountain systems: Are they enough to meet the challenge of climate change? *Glob. Environ. Change*, No. 54, 19–30.
- Mikhaleiko, V.N., 1993. Calculation and reconstruction of the mass balance of the Ak-Shyirak glacial system in the Tien Shan. *Materialy Glaciol. Issled. [Data of Glaciological Studies]*, iss. 76, 102–107 (in Russian).
- Narama, C., Kääb, A., Duishonakunov, M., Abdrakhmatov, K., 2010. Spatial variability of recent glacier area changes in the Tien Shan Mountains, Central Asia, using Corona (~1970), Landsat (~2000), and ALOS (~2007) satellite data. *Glob. and Planet. Change* 71 (1–2), 42–54.
- Oerter, H., Moser, H., 1982. Water storage and drainage within the firn of a temperate glacier (Vernagtferner, Oetztal Alps, Austria). In: *Hydrological Aspects of Alpine and High Mountain Areas: Proc. of the Exeter Symposium (July 1982, Exeter, UK)*, IAHS Publ., No. 138, pp. 71–83.
- Petrakov, D., Shpuntova, A., Aleinikov, A., et al., 2016. Accelerated glacier shrinkage in the Ak-Shyirak massif, Inner Tien Shan, during 2003–2013. *Sci. Total Environ.*, No. 562, 364–378.
- Petrakov, D.A., Tutubalina, O.V., Shpuntova, A.M., et al., 2019. Assessment of glacier albedo in the Ak-Shyirak massif (Inner Tien Shan) from ground-based and Landsat data. *Earth's Cryosphere XXIII* (3), 11–19.
- Popovnin, V.V., Gubanov, A.S., Satylkanov, R.A., Ermenbaev, B.O., 2021. Reconstruction of the mass balance of the Sary-Tor glacier from meteorological data. *Led i Sneg [Ice and Snow]*, 61 (1), 58–74 (in Russian).
- Rets, E.P., Frolova, N.L., Popovnin, V.V., 2011. Modeling the melting of the surface of a mountain glacier. *Led i Sneg [Ice and Snow]*, No. 4 (116), 24–31 (in Russian).

- Rets, E., Kireeva, M., 2010. Hazardous hydrological processes in mountainous areas under the impact of recent climate change: case study of Terek River basin. In: *Global Change: Facing Risks and Threats to Water Resources*. Proc. of the Sixth World FRIEND Conf. Fez, IAHS Publ., Morocco, No. 340, pp. 126–134.
- Rets, E.P., Kireeva, M.B., Loshakova, N.A., 2014. Heat balance model for the study of features formation of the flow of a glacial river (on example, of the r. Djankuat basin). *Eurasian Union of Scientists (ESU)*, No. IV, 97–103 (in Russian).
- Rohrer, M.B., Braun, L.N., 1994. Long-term records of snow cover water equivalent in the Swiss Alps, 2. Simulation. *Nordic Hydrol.* 25 (1–2), 65–78.
- Rybak, O.O., Rybak, E.A., Yaitskaya, N.A., et al., 2019. Modeling the evolution of mountain glaciers: a case study of Sary-Tor glacier (Inner Tien Shan). *Earth's Cryosphere XXIII* (3), 27–42.
- Semenova, O., Beven, K., 2015. Barriers to progress in distributed hydrological modelling. *Hydrol. Processes* 29 (8), 2074–2078.
- Seo, D., Azar, A.E., Khanbilvardi, R., Powell, A., 2008. Analysis of snowpack properties and estimation of snow grain size using CLPX Data. *Geosci. and Remote Sensing Symp.*, vol. 4, IV-1034–IV-1037.
- Shannon, S., Smith, R., Wiltshire, A., et al., 2019. Global glacier volume projections under high-end climate change scenarios. *Cryosphere*, No. 13, 325–350.
- Shea, J.M., Immerzeel, W.W., 2016. An assessment of basin-scale glaciological and hydrological sensitivities in the Hindu Kush-Himalaya. *Ann. Glaciol.* 57 (71), 308–318.
- Shpuntova, A.M., Usabaliev, R.A., Petrakov, D.A., 2019. Modern changes in the area of glaciation of the Ak-Shyirak massif (Inner Tien Shan). In: *Remote and ground-based studies of the Earth in Central Asia: Proc. of the Intern. conf. MoYuR Bishkek*, Bishkek, pp. 252–258 (in Russian).
- Siegfried, T., Bernauer, T., Guiennet, R., et al., 2012. Will climate change exacerbate water stress in Central Asia? *Clim. Chang.* 112, 881–899.
- Singh, P., Singh, V.P., 2001. *Snow and Glacier Hydrology*. Kluwer Academic Publ., Boston, 742 pp.
- Snow and Climate Physical Processes, Surface Energy Exchange and Modeling / R.L. Armstrong, E. Brun (Eds.), 2008. *Antarctic Science*. Cambridge Univ. Press, Cambridge, vol. 20 (6), pp. 610–611.
- Sorg, A., Bolch, T., Stoffel, M., et al., 2012. Climate change impacts on glaciers and runoff in Tien Shan (Central Asia). *Nat. Clim. Chang.* 2 (10), 725–731.
- Sorg, A., Huss, M., Rohrer, M., Stoffel, M., 2014. The days of plenty might soon be over in glacierized Central Asian catchments. *Environ. Res. Lett.* 9 (10), p. 104018.
- Sturm, M., Holmgren, J., König, M., Morris, K., 1997. Thermal conductivity of seasonal snow. *J. Glaciol.* 43 (143), 26–41.
- Takeuchi, N., Fujita, K., Aizen, V.B., et al., 2014. The disappearance of glaciers in the Tien Shan Mountains in Central Asia at the end of Pleistocene. *Quatern. Sci. Rev.* 103, 26–33.
- Unger-Shayesteh, K., Vorogushyn, S., Farinotti, D., et al., 2013. What do we know about past changes in the water cycle of Central Asian headwaters? A review. *Glob. and Planet. Change*, 110, No. A, 4–25.
- Ushnutsev, S.N., 1991. Oscillations of the mass balance of the Sary-Tor Glacier in the Inner Tien Shan and its reconstruction for 1930–1988. *Materialy Glaciol. Issled. [Data of Glaciological Studies]*, iss. 71, 70–80 (in Russian).
- Vinogradov, Yu.B., Vinogradova, T.A., 2010. *Mathematical modeling in hydrology*. Publisher. house “Academy”, Moscow, 204 pp. (in Russian).
- Voloshina, A.P., 1988. Climatic and meteorological features of the area of glaciation of the Ak-Shyirak massif. *Materialy Glaciol. Issled. [Data of Glaciological Studies]*, iss. 62, 184–193 (in Russian).
- Zhupankhan, A., Tussupova, K., Berndtsson, R., 2017. Could changing power relationships lead to better water sharing in Central Asia? *Water* 9 (139), 17 pp.
URL: <https://wgms.ch/> (last visited: 10.11.2019).

Received December 16, 2019

Revised May 8, 2021

Accepted June 20, 2021

Translated by A.V. Muravyov

CRYOSPHERE RESEARCH METHODS

THE STUDY OF SEASONAL VERTICAL CHANGES OF GROUND SURFACE
IN THE POLAR URAL FOOTHILLS BASED ON FIELD MEASUREMENTS
AND ALOS PALSAR RADAR INTERFEROMETRY

V.V. Elsakov, D.A. Kaverin, V.M. Shchanov

*Institute of Biology, Komi Science Centre UrB RAS, Kommunisticheskaya str. 28, Syktyvkar, 167982, Russia;
elsakov@ib.komisc.ru, dkav@mail.ru, shchanov@ib.komisc.ru*

Interferometric pairs of ALOS PALSAR dataset (2007–2010) were used to estimate the seasonal and long-term variations in the ground surface height in the piedmont of the Polar Ural, the far northeast of European Russia. The obtained results were validated by ground-truth measurements at the CALM R2 site (active layer thickness monitoring site). The values and amplitude of ground surface height variations obtained from the satellite imagery were lower compared to field measurements. The sites under study were classified in two conditional groups: more drained sites (confined to the upper parts of the moraine ridges) and sites with higher moisture content in the soil (lower parts of the slopes). This classification was based on the intensity of seasonal changes in the height of ground surface during the vegetation period of 2007. Significant correlations between *in situ* and remote sensing-based measurements were established for these groups. The convergence of the results increased with a greater number of *in situ* measurements inside the pixel of the satellite image. The greatest differences in the magnitude of vertical movements of ground surface were reported in the years with contrasting weather conditions (2007 and 2010). Ground surface subsidence was reported to be greater (up to 1.5–4.5 cm) during the colder and wetter vegetation period of 2010, and less pronounced in a drier and warmer season of 2007 (0–3.0 cm) within tundra zones of the Pechora Lowland. A summer heave of ground surface was noted (up to 2–3 cm) in sites with moraine deposits in the piedmont plains for the whole period of observations.

Keywords: differential radar interferometry, piedmont landscapes of the Polar Ural, ground subsidence and heave.

INTRODUCTION

Changes in ground surface elevation can be caused by various geological (both exogenous and endogenous) processes [Dobrovolsky, 2001]. The differential interferometry synthetic aperture radar (DInSAR) technique is based on analysis of the phase shift of the echo signals of multitemporal images, which allows measuring ground surface displacements to a centimetre-level accuracy over large areas. Interferometry using data from spaceborne SAR instruments has proven to be not inferior to conventional geodetic monitoring methods [Musikhin, 2012; Chimitdorzhiev et al., 2013]. Present-day DInSAR-based investigations deal with the analysis of surface-level variations induced by both natural and technogenic effects: underground mine workings [Epov et al., 2012], oil extraction [Evtuyushkin, Filatov, 2009; Elsakov, 2012], and growth of urban areas [Gornyy et al., 2010].

Cycles of freezing and thawing of the active layer containing different amounts of ground ice are among major causes of vertical movements of the ground surface in permafrost regions [Kachurin, 1961; Bockheim, 2015]. Recent years have seen an increased interest in monitoring of natural surface deformations in the permafrost zone considered as indicators of

cryogenic landscapes changes at a local or regional level. The balance between multidirectional seasonal thaw subsidence and heave processes is one of the key indicators of changes in permafrost and thermokarst development. The intensity of winter heave and summer subsidence of the ground surface is largely related to climatic conditions [Mazhitova, Kaverin, 2007; Romanovsky et al., 2008].

Meteorological observations in the north of Russia demonstrate the existence of a steady warming trend during the period 1976–2012 marked by increased surface air temperature (SAT) [Leshkevich, 2014]. This has resulted in a higher rate of permafrost degradation and enhanced biological productivity of tundra plant communities, while the implications of climate change in the Arctic are spatially heterogeneous [Elsakov, 2017]. The informative value of DInSAR methods is noted in research of Alaska ecosystems [Liu et al., 2010], the Canadian Arctic Archipelago [Short et al., 2014; Rudy et al., 2018], Central Siberia [Chimitdorzhiev et al., 2013; Antonova et al., 2018], the Tibetan plateau [Chen et al., 2013], etc. More frequent surveying (up to 6–12 days for Sentinel-1A/B) has made the method indispensable for

studies of the seasonal dynamic of the mosaic permafrost landscapes. However, given that interferograms are generated for meteorologically different years and span a relatively short period, they need to be validated by systematic ground-based observations. A lack of available and unified field measurements for verification and calibration of the results obtained has been the biggest constrain to expanding DInSAR-based applications for monitoring the northern areas. This was primarily due to the curtailment of many long-term monitoring programs at permanently operating integrated geocryological and biocenotic research stations in the last decades. The established and subsequently expanded Circumpolar Active Layer Monitoring (CALM) network allow resuming the collection and unification of datasets from long-term observations of changes in seasonal thaw depth (active layer thickness, ALT) and ground surface deformations in permafrost areas [Brown et al., 2000].

The aim of this work was to compare seasonal and interannual vertical movements of permafrost-affected soil surface within the piedmont plain of the Polar Urals calculated with interferometric pairs of ALOS PALSAR images and the data of field topographic surveys obtained in the meteorologically contrasting years.

STUDY AREA

The study area is located in the northeast of European Russia in the southern hypoarctic tundra subzone which abuts with the Polar Urals (Fig. 1, A)

[Geobotanical zoning..., 1989]. According to the map of Neogene-Quaternary deposits of Vorkuta district (scale 1:200 000) and the accompanying Explanatory Note [Shishkin et al., 2013], three regions are identified within the study area based on its geological structure [Shishkin et al., 2013]. The western part is located within the platform plain having a thick sedimentary cover of glacial deposits (up to 40 m) and thinner alluvial-marine deposits (up to 20 m) and includes areas of fens and raised bogs (Fig. 2, A). The flat terrain is subsequently replaced to the east by piedmont and intermountain plains with patches of gently undulating outwash plains passing into a hilly glacial plain with areas of accumulative-denudation plain composed of up to 5 m thick lacustrine-glacial deposits. The eastern part of the study area includes a mountain belt whose area is dominated by flat-topped rough and low mountains.

The study area is characterized by continuous and discontinuous permafrost distribution with a thickness of 50–150 m and mean annual ground temperature from 0 to -2°C [Ershov, 1996]. The permafrost table has a complex configuration with through taliks beneath watersheds and river beds. The depth of seasonal thaw of soils is highly differentiated depending on the vegetation cover patterns and snow cover thickness. Shallow (up to 1 m) occurrence of the permafrost table is rather common for moss-dwarf shrub tundra, while permafrost usually occurs at a depth of 1–2 m and more under large-shrub or willow communities [Mazhitova, 2008]. Analysis of the vegetation map generated with the supervised classi-

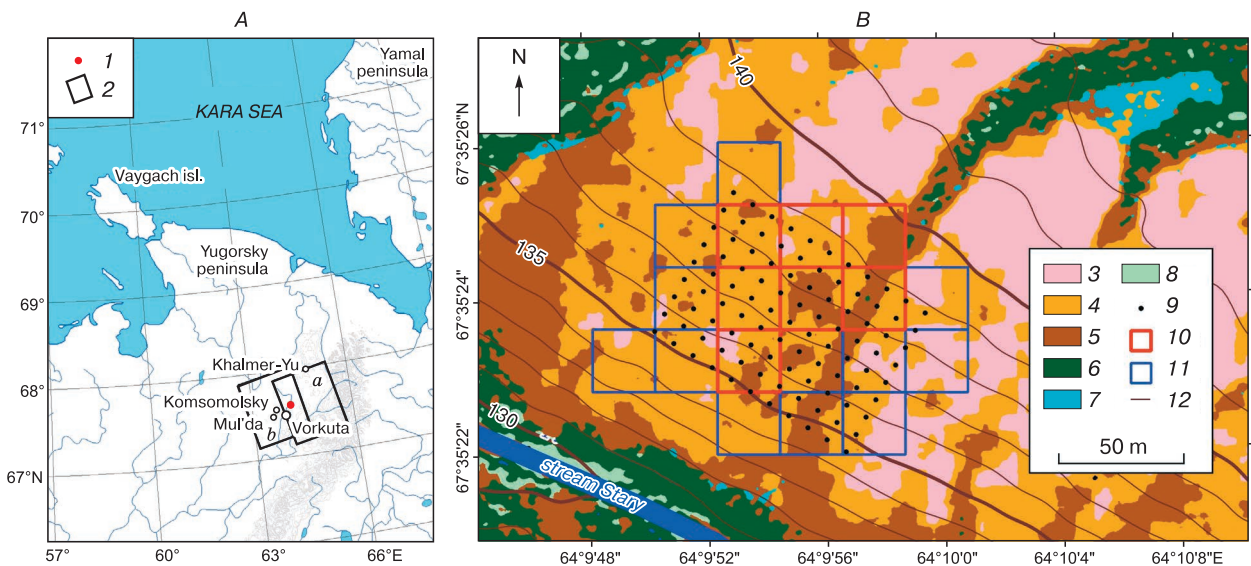


Fig. 1. The location of CALM R2 site and contours ALOS PALSAR dataset (A). The distribution of field observation points and PALSAR pixel net (25 × 25 m) within the instrumental measurement site (B).

1 – CALM R2 monitoring site; 2 – contours of ALOS PALSAR images; 3 – low-shrub-lichen tundra; 4 – dwarf shrub tundra; 5 – low bush tundra; 6 – willow-shrubs; 7 – swampland complexes; 8 – grass communities; 9 – reference rods for in situ measurements; 10 – pixels assigned in 2007 to the cluster “upper parts of the sloping hill”; 11 – pixels for the cluster “lower parts of the sloping hill”; 12 – contour lines.

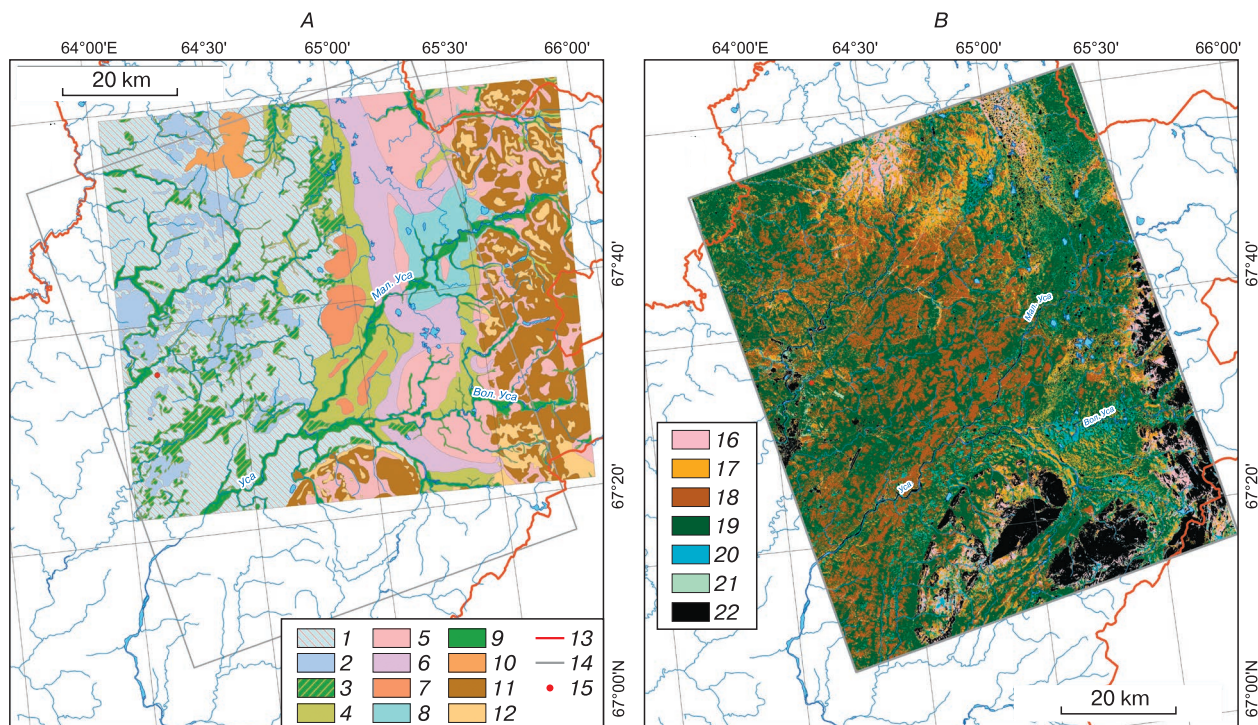


Fig. 2. Main geomorphological elements (A) and dominant vegetation cover classes (Landsat 7 ETM+ processing) (B).

Landscape-geomorphological complexes: 1–3 – platform plain (1 – rolling-undulating smoothed glacial plain; 2 – gently undulating plain with alluvial-marine alluvial sediments; 3 – peatlands); 4–10 – piedmont and intermontane plains (4 – outwash plain; 5 – rolling glacial plain on the Khanmei moraine; 6 – marginal rolling ridge-like glacial debris accumulation formations; 7 – rolling-ridge glacial plain on the Pachvozh moraine; 8 – accumulation-denudation plain on lacustrine-glacial deposits of the Khanmei moraine; 9 – floodplain terraces; 10 – rolling steeply-sloping denudation plain); 11, 12 – mountain belt (11 – steep glacial-exaration slopes; 12 – gentle slopes with glacial accumulative deposits); 13 – boundaries of the Komi Republic; 14 – ALOS PALSAR satellite image contours; 15 – location of the CALM R2 site. Vegetation cover classes: 16 – low-shrub-lichen tundra; 17 – dwarf shrub tundra; 18 – shrub tundra; 19 – willow shrub; 20 – bog plant association complexes; 21 – grass communities; 22 – barren patches.

fication of Landsat 7 ETM+ imagery (shooting: 137.7.2000) (Fig. 2, B) has revealed seven dominant classes of vegetation cover. The tundra plant communities are represented by shrub (20.7 % of the image area), dwarf-shrub (15.6 %) and shrub-lichen (4.7 %) vegetation. Azonal groups include willow shrubs (42.2 %), bog plant species assemblages (5.6 %), areas of grass communities (0.6 %). Territories without vegetation cover account for 10.3 % of the area.

The choice of the study area and the selection of satellite imagery was prompted by the availability of the CALM R2 monitoring site (67°35.04' N, 64°09.09' E) located 13 km northeast of Vorkuta city and having long-term series of ALT measurements, surface elevation and soil temperature. The CALM R2 site (81 × 88 m in size) is located on the southwestern slope of a riverine ridge and consists of a network of 99 permanent observational grid nodes with 9 × 8 m grid cells (Fig. 1, B). The surface slope is on average 3°, the elevation difference is not more than 4 m. The main orographic elements of the site are flat

hilly-ridge uplands with flat slightly convex tops and long gentle slopes [Druzhinina, Myalo, 1990]. The vegetation cover of the site is mosaic, dominated by communities of small dwarf-moss tundras on the tops of watershed ridges, large shrub tundras on the slopes of ridges, and bog complexes in depressions and on the flat tops of ridges. The site is dominated by gley soils on clay loams; ice content of the underlying permafrost varies from 40 to 50 % [Mazhitova, Kaverin, 2007]. The average ALT varied from 86 to 89 cm during the study period.

RESEARCH METHODS

Monitoring studies. Within the CALM R2 key site year-round soil temperature measurements (at depths of 0, 0.2, and 0.5 m) were carried out using HOBO U-12 data loggers, and ALT was measured with graduated metal probe stick. To determine the heaving/subsidence of the soil surface in all grid nodes of the site, the elevations of the permafrost top and soil surface were measured annually after the

snowmelt (late May) and at the end of the warm season (late September). The measurements were taken with a common instrumental levelling method using Geobox N8-32 optical level with 1.5 mm per 1 km accuracy. A state geodetic survey benchmark located 100 m away from the site served as a stationary reference to determine absolute heights.

The main climatic parameters were derived from the RIHMI–WDC (Russian Institute of Hydrometeorological Information-World Data Center) archive data (<http://www.meteo.ru>). When characterizing the weather conditions at the time of SAR images acquisitions, the weather archive for the weather station in Vorkuta (airport) (WMO ID 23226) (<http://rp5.ru>) was used. To assess the influence of meteorological factors on vertical movements of the ground surface, a sum of average daily positive (thawing degree days, TDD) and negative (freezing degree days, FDD) air temperatures were calculated for the hydrological years (October 1 – September 30) of the study period.

Satellite images processing. Satellite images were processed using the ENVI SARscape module. The phase unwrapping was obtained with the “Minimum Cost Flow” automated algorithm. The parameters of ground control points (GCPs) within the runway segments of the Vorkuta airport were taken into account during phase unwrapping. The 2007–2011 ALOS PALSAR images (Fine Beam Dual scanning mode, *L* range, 23.5 cm wavelength, 34.3° off-nadir angle for all scenes) were used to construct two sets of overlapping interferometric pairs (Table 1). In the *L*-range radar imaging, the height of vegetation can be ignored, since the signal is predominantly reflected from the ground surface. Surface deformations were determined by their comparison with master images (15.08.07 and 18.09.07). Master images were selected by the least visual distortion of the resulting interferograms associated with the atmospheric phase delay (caused by atmospheric effects). For most of the compared images, the perpendicular component of the baseline (Bn) had acceptable values (from 298 to 2128 m). The differential interferogram was calculated from the ArcticDEM digital elevation model which was used as a terrain data source (<https://www.pgc.umn.edu/data/arcticdem>).

The surface level displacement was computed for satellite images with 25 m pixel size and the noise was suppressed by applying adaptive filtering before the phase unwrapping. The weather conditions were inferred from information on the shooting time (17:30 UTC) (Table 1). The effect of precipitation and cloud cover on most of the images was negligible. Scenes with signal distortions (i.e. inaccurate phase shift) caused by atmospheric interference were rejected from the analysis.

Table 1. **ALOS PALSAR scenes and weather conditions on the shooting dates**

No.	ALOS PALSAR scenes	Bn, m	N, %	Daily precipitation
Path/Frame 529/1350 17:42 UTC (a)				
1	18.09.07 (master-image)		40	–
2	18.06.07	615	100	drizzle, 2.6 mm
3	08.08.09	2128	100	rain
4	26.06.10	1018	70–80	rain shower, 0.2 mm
5	11.08.10	1479	100	drizzle, 7.0 mm
Path/Frame 527/1350 17:35 UTC (b)				
6	15.08.07 (master-image)		100	–
7	30.06.07	298	<10	–
8	30.09.07	512	100	light rain shower, 4.4 mm
9	02.07.08	1621	–	–
10	08.07.10	1389	20–30	–
11	23.08.10	1808	70–80	rain shower, 6.0 mm
12	17.08.08	5269	60	rain, 0.1 mm

Note. Bn – perpendicular baseline; N – cloudiness, according to the Vorkuta (airport) weather station archive (WMO ID 23226).

Analysis of temporal variations in the ground surface. Characterization of the seasonal variations in the ground surface movements within the key site was made by two approaches. The first approach analyzes the pairs of PALSAR images from the same set which differ maximally in shooting dates within the season (for summer subsidence: 30.06–30.09.07 and 08.07–23.08.10; for winter frost heave: 30.09.07–02.07.08). The available image pairs often did not represent the maximum values of seasonal subsidence and heave. The comparison of satellite data with in situ measurements made on adjacent dates allows comparing the methods employed.

The second approach is focused on the course of seasonal changes of the ground surface using complete sets of scenes. ALOS PALSAR surveys provide interferometric measurements with the 46-day repeats, thus allowing taking not more than 3–4 images per year during the snow-free period. However, the set of images included two territorially overlapping groups (their boundaries are shown via contours marked as *a* and *b* in Fig. 1). Changes in the soil surface level were computed for all the images from the set of group *a* (master scene 18.09.07) and *b* (master scene 15.08.07). Master images of two groups were not mutually calibrated by soil surface elevation and were acquired on different dates. Therefore, the indicators were recalculated for different groups using similar-time scenes. Most comparable were images of the end of the growing season (18.09.07 for group *a* and 30.09.07 for group *b*). The values for the ground

surface level were taken as equal numbers for the same sites on these dates and sets of images were calibrated relative to the baseline scene (15.08.07).

Analysis of georeferencing of ALOS PALSAR images has demonstrated “sub-pixel accuracy of georeferencing” [Baranov *et al.*, 2008]. The satellite image matrix of the CALM R2 monitoring site is formed by 19 pixels (Fig. 1, B). The field observations values were averaged by the pixels of satellite images for comparative analysis of the variance between the ALOS PALSAR data and instrumental measurements. The number of field measurements at a pixel varied from 1 to 10. Results of the satellite and *in situ* measurements were used to compare summer subsidence of the ground surface for meteorologically contrasting years 2007 and 2010. Frost heave values were calculated and compared for the hydrological year 2007/08.

RESEARCH RESULTS

Comparison of changes in ground surface elevations estimated from satellite images and instrumental measurements. Comparison of the results of the DInSAR data processing and field measured elevations demonstrated that the values for the ground surface movements over 2007 were distinctly separated into two conventional groups according to their position in the relief (Fig. 3, a): drained, predominantly upper parts of the hill (summit, 7 pixels) and lower, essentially wetter (hill base, 12 pixels) areas. When split, the compared indicators obtained by different methods showed significant correlations (for the summit group the rank correlation coefficient $r = 0.83$, probability $p < 0.05$ with total number of observations $n = 7$, for the hill base group: $r = 0.86$, $p < 0.01$, $n = 12$). Significant correlations observed

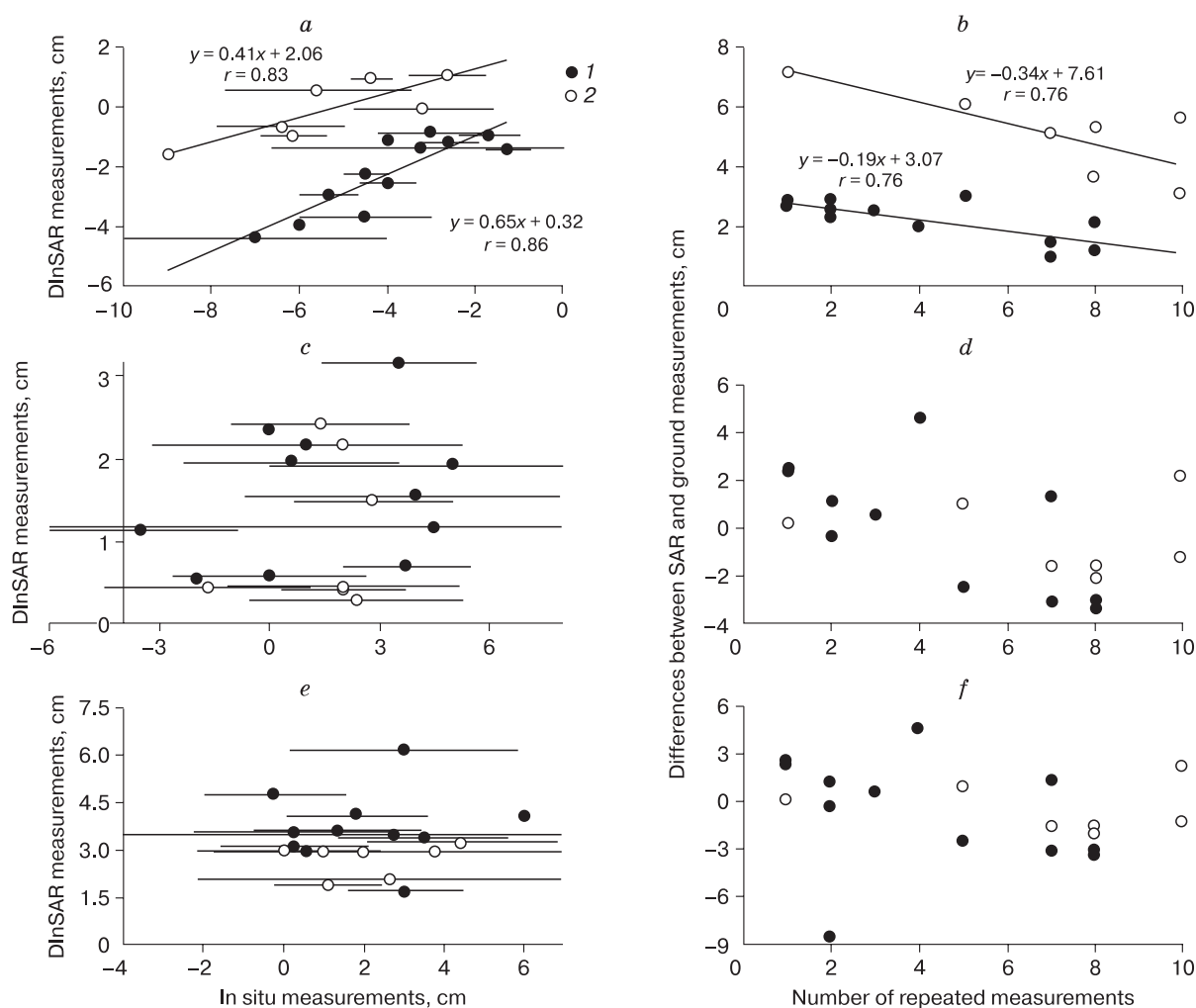


Fig. 3. Seasonal vertical movements of the ground surface from satellite imagery and field measurements.

The mean volumes and standard deviation (SD) are presented (a, c, e). Subsidence is presented by negative value. Measurements dates: a – 30.06–30.09.07; c – 08.07–23.08.10; e – 30.09.07–02.07.08. Differences between the values of satellite and ground methods and numbers of ground measurements (n) in pixel of satellite image (b, d, f): b – 30.06–30.09.07; d – 08.07–23.08.10; f – 30.09.07–02.07.08. Groups of pixels assigned to: 1 – lower part of the sloping hill; 2 – upper part of the sloping hill.

between indicators obtained by different methods of measurements allowed separation of the value set into two clusters differing in their location in the relief: for the summit group the rank correlation coefficient (r) 0.83 ($n = 7, p < 0.05$), for the base of hill group 0.86 ($n = 12, p < 0.01$). The difference between the values of satellite and field observations was the slightest for the cluster of pixels located at the lower part of the hill. The satellite measurements had lower values and amplitudes of variations compared to the pointwise in situ measurements. The upper (drained) segments of the hill are characterized by lesser seasonal surface deformations according to the DInSAR data: from the heave of 1.1 cm to subsidence of 1.7 cm. The *in situ* measurements at the sites were marked by a greater magnitude and amplitude of variation: from 2.6 to 9.0 cm of subsidence. The data obtained by the different methods equally demonstrated that surface deformation in the lower parts of the bluff is represented by subsidence only: from 0.8 to 4.4 cm with DInSAR data and from 1.4 to 7.0 cm with *in situ* measurements. A more pronounced soil surface subsidence in the lower part of the site is associated with higher water content and active thawing of ice-rich ALT layers. The differences between ground-based and remote measurements can be explained by different size of the measurement areas: ground measurements are pointwise, while the size of pixels utilized in ALOS PALSAR images covers an area sized 25×25 m. The inconsistency between the results obtained by different methods tended to decrease with higher number of measurement points per pixel ($r^2 = 0.58, n = 12, p < 0.01$ and $r^2 = 0.59, n = 7, p < 0.05$) and proved to be minimal (< 1.0 cm) for the lower parts of the hill at $n = 7-8$ (Fig. 3, *b*).

Results showed the largest mismatch (up to 7.3 cm) for the segments in the upper parts of the hill and with single instrumental measurements at the pixel. On average, the mismatch decreased from 0.2 cm (base) to 0.3 cm (summit) per each additional point of *in situ* measurements. The agreement of results obtained by different methods in 2007 was good due to very close dates of DInSAR acquisitions and field observations.

The differences for the 2010 growing season were largely related to shorter intervals for DInSAR observations (only 46 days) by the instrumental method. Low- and medium-amplitude ground surface heave (08.07–23.08.10) was determined from satellite (0.3–3.2 cm) and instrumental (0–5 cm) measurements at the key site. The subsidence of up to 3.5 cm was recorded at several pixels (Fig. 3, *c*). The pixels splitting into clusters according to the relief features was found inconsistent with the year 2007, and the values of in situ measurements showed higher variability. The larger number of measurements at the pixel did not improve the agreement between the satellite and field measurements (Fig. 3, *d*) due to a lesser overlaying of intervals of observations with these methods. The relatively low surface subsidence can be explained by lower summer air temperatures but high amount of precipitation (44 % higher than mean annual) during the 2010 growing season (Table 2). The greater subsidence in the warmer and less the humid year 2007 has demonstrated the permafrost response (depending on local topography and surface conditions) to air temperature warming.

The measured surface heave was 1.7–6.2 cm (DInSAR estimates) and 0–6.0 cm (in situ measurements) at the monitoring site during the 2007/08 winter season. The greatest DInSAR-derived displacements were reported from sites assigned to the cluster of the base of the hill (Fig. 3, *e*). Increasing of number of *in situ* measurements in pixel did not improve convergence.

Seasonal changes in soil surface. The weather conditions are interpreted as the most contrasting during the periods 2006/07 and 2009/10 among the compared periods (Table 2). The diversity of surface air temperature characteristics in different years is reflected in the ALT temperature records. Ground temperatures reached the minimum (-3.7 °C) at a depth of 0.2 m to April 2010 due to a larger amount of winter precipitation and snow isolation. The minimal soil temperature in 2007 was recorded earlier, in the beginning of March (-3.3 °C) due to lower precipitation amount. The daily mean soil temperatures in 2007 were in the range from $+0.8$ to $+2.1$ °C (depth:

Table 2. Climatic indicators for the compared years of observation

Hydrogeological years	Temperature			Amount of precipitation, mm		
	<i>TDD</i> , °C·days	<i>FDD</i> , °C·days	T_{mean} , °C	per year	liquid	solid
2006/07	1277 (14.9)	-2498 (8.9)	-3.8	489	220 (-15.7)	269 (-20.9)
2007/08	1126 (1.4)	-2322 (15.3)	-3.6	525	195 (-25.4)	331 (-2.8)
2008/09	1046 (-5.9)	-2604 (5.0)	-4.5	613	252 (-3.3)	361 (6.2)
2009/10	995 (-10.4)	-3542 (-29.2)	-7.0	776	376 (44.4)	399 (17.4)
Average	1111	-2742	-4.7	600.7	260.6	340.1

Note. The values in parentheses are standard deviations from the multiyear means (%). T_{mean} – mean annual air temperature.

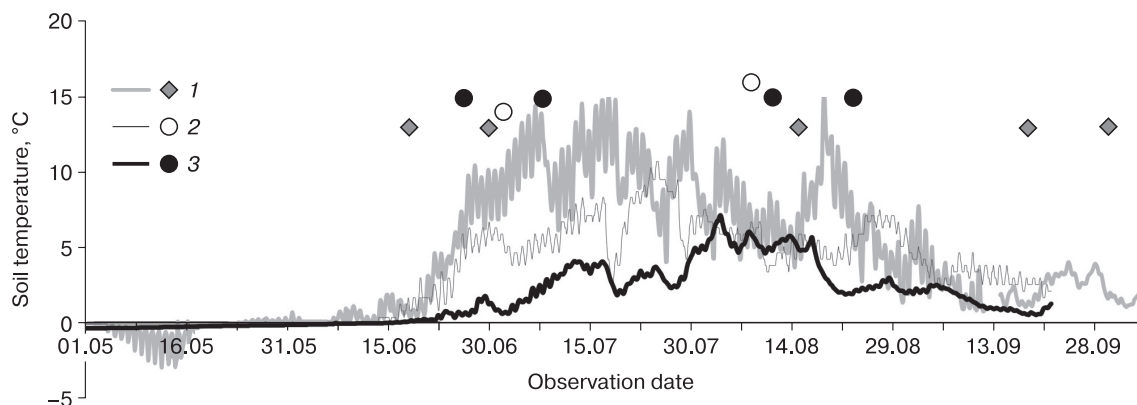


Fig. 4. The soil temperature dynamic at a depth of 0.2 m during growing seasons in different years with the 3 h measuring step.

1 – 2007; 2 – 2008; 3 – 2010.

0.2 m) and from -0.1 to -0.2 °C (depth: 0.5 m) (Fig. 4) at the time of the first survey (18.06.07) because of the early warming of the soil profile. The soil temperatures warmed slowly in the 2010 growing season: transition over 0 °C (TDD) at 0.2 m depth was recorded in mid-June. By the time of the first survey (26.06.10) the ground temperature had warmed to $+0.5 \dots +0.6$ °C.

The 2007 growing season was the warmest within the observation period. Differences in summer air temperatures for growing seasons of different years demonstrate a clearly TDD decreasing trend from 2007 to 2010 (Table 2). Soil was warming most intensely in the first half of the summer 2007 and the maximum temperature ($+14.3$ °C) at a depth of 0.2 m was recorded on July 6 (i.e. 6 days after the PALSAR acquisitions). Soils demonstrated slower heating in 2010: maximal temperature ($+7.1$ °C) was recorded on August 3.

The average ALT depth was close for years with contrasting temperature conditions: (89 ± 14) cm in 2007 and (89 ± 13) cm in 2010 ($n = 99$). The summers in these years were characterized by remarkable differences in the surface air temperatures (SAT) effected the ground which were balanced by contrasting summer rainfall amount. Results of ground deformation measured *in situ* showed a subsidence of surface (4.0 ± 3.5) cm ($n = 19$) at the CALM site during May–September 2007, against its heave (2.2 ± 4.9) cm noted in 2010. The 2008 temperature values occupied an intermediate position between 2007 and 2010. First PALSAR acquisitions of 2007 and 2010 were coincident with the beginning of soil heating (freeze-thaw transition), which suggests a minimal partial compensation for winter heave. The exception is 2008, when first acquisitions were coincident with the heating of compared soil depth (0.2 m) to 5 °C.

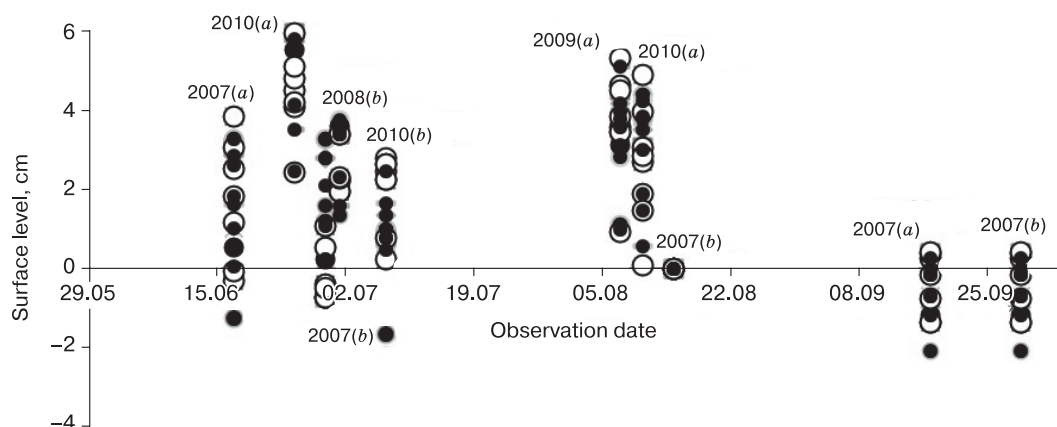


Fig. 5. Ground vertical movements at the CALM R2 monitoring site for different years.

Satellite image pairs: *a* – 529/1350; *b* – 527/1350; parts of the lower part of the slope hill (dark dots) and upper part (light dots). The zero value of surface level is taken for date of master-image (15.08.07).

The ground surface dynamics for growing seasons of different years based on remote sensing method was determined from comparison of the subsidence/heave amplitudes within the monitoring site pixels on satellite images. The maximum soil surface subsidence within the observation period was reported in 2007 (Fig. 5), similarly to the *in situ* measurements. The average variation in ground surface elevation in the upper part of the hill was characterized by lower values (subsidence: 0 to 1 cm) against its base (2 to 4 cm) in that year. The disagreement in estimates for seasonal variations on the 2010 scenes (reduction from 26.06.10 to 08.07.10 with subsequent increase by 11.08.10) was most likely to be a result of using different sets of satellite scenes (527/1350 and 529/1350).

In terms of magnitude of land-surface subsidence, the weather conditions of the 2009 summer season were the most consistent with the years 2010, and 2007 with 2008, which is also corroborated by soil temperatures and meteorological parameters, accordingly (Table 2). The winter seasonal heave was only slightly compensated by summer subsidence during the years with relatively cold summers (2009 and especially 2010).

The seasonal and interannual vertical surface movements at a regional level. Satellite imagery offering a good spatial coverage (the ALOS PALSAR scene size covers an area of 69 × 87 km) allows detecting and quantifying vertical ground surface movements within large areas. The maximal vertical surface displacements noted on human-affected areas

(e.g., recent backfill or soil removal and subsidence in coal-mining areas).

The summer surface subsidence of undisturbed soil cover is fragmentarily presented (Fig. 6, A) at the mining field of the coal-mining company Vorkutau-gol. It was rather considerable in amplitude (>16 cm), but area was small (0.7–1.0 km diameter) in different years. Localities of subsidence sites varied from year to year (Fig. 6, B). The 2012 field studies revealed no visible changes in the moss-lichen cover and structure of plant communities at these sites.

Significant seasonal ground displacements are not inherent to the undisturbed tundra ecosystems (Fig. 7). The largest areas where summer settlement of the soil surface (up to 3 cm) is observed on natural depressions of drainage hollows and downgraded areas between hills. Low (1.5–3.0 cm) and moderate amplitudes (3.0–4.5 cm) of surface subsidence were observed on 30–40 % of the area of swampland ecosystems and large-shrub tundra in the summer of 2007 and 2010. Low heaves of soil surface were reported within 23 % of the area of low-shrub lichen tundra. The dwarf birch (*Betula nana*) moss tundra and grass communities showed no significant changes.

The regional soil surface dynamics has been remarkably affected by quaternary sediments distribution (Fig. 2, A). The ground surface subsidence was maximal in 2010 (1.5–4.5 cm) and less expressed in 2007 in the flat portion of the study area (Fig. 7). The summer surface heaves (1.5–4.5 cm) were noted at rather large areas in the piedmont plains of the Polar

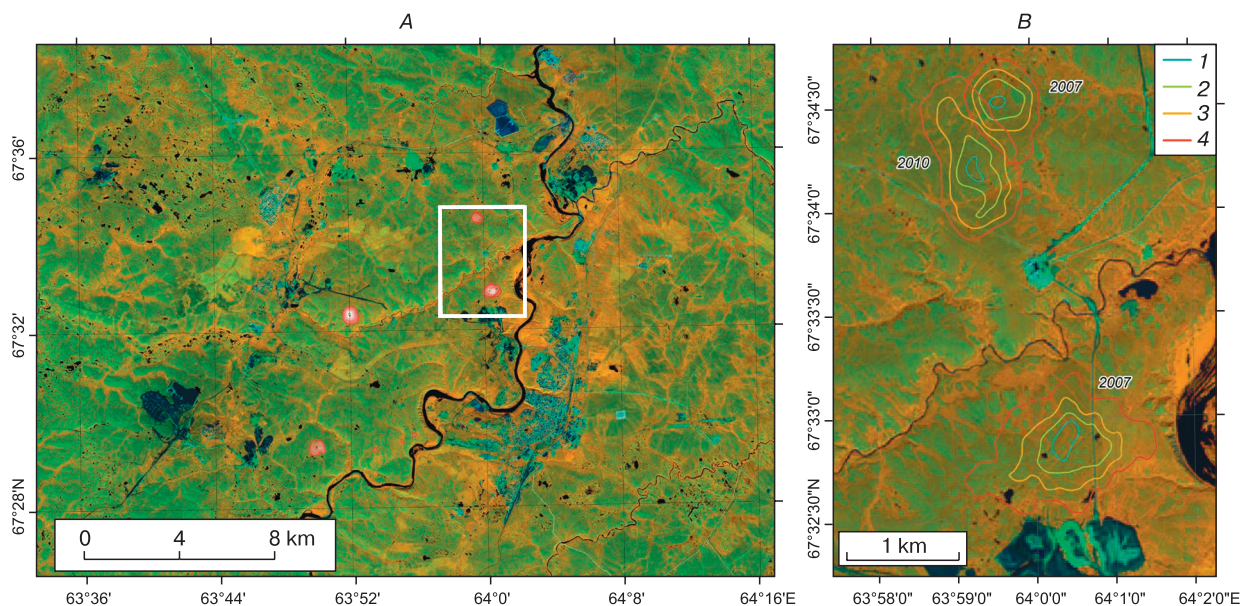


Fig. 6. Subsidence near coal-mines in the vicinity of Vorkuta city in 2007 (A) and 2010 (B). The colored contour lines mark subsidence.

1 – over 16 cm; 2 – over 12 cm; 3 – over 8 cm; 4 – over 4 cm. Background: Sentinel-2 image acquired 25.07.19 (<http://www.glovis.usgs.gov>).

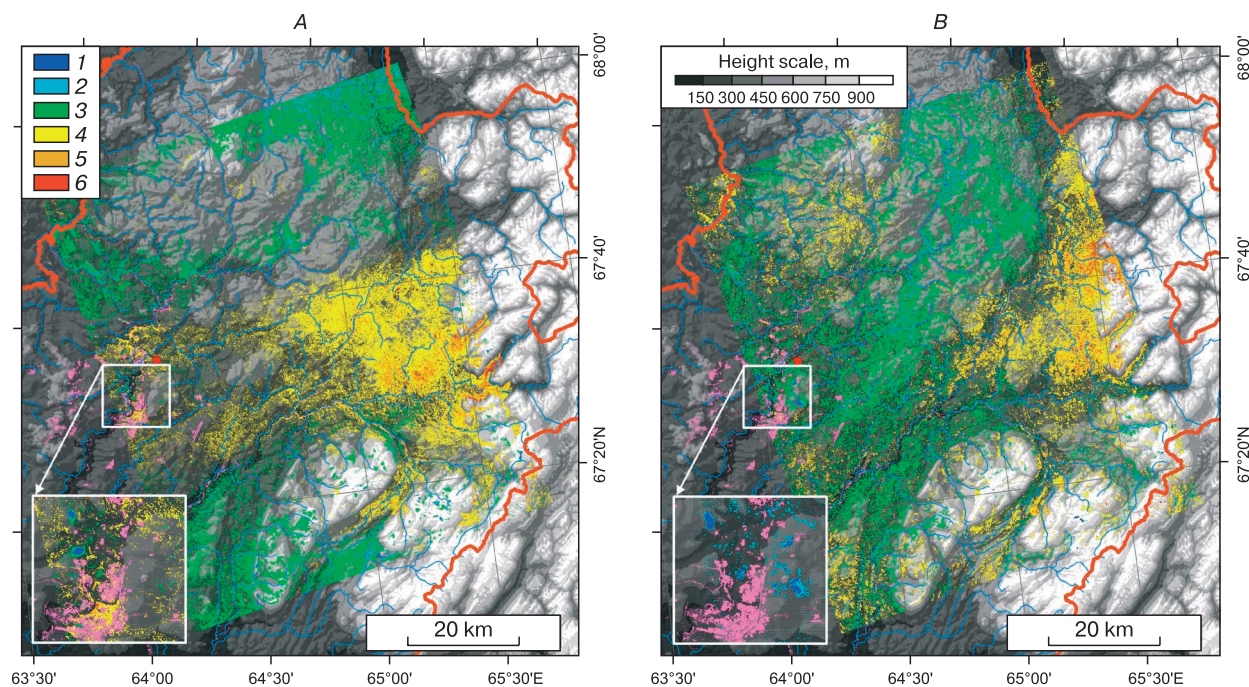


Fig. 7. The ground surface movements on the western slopes of the Polar Urals and Bolshezemelskaya tundra for the periods 15.08–30.09.07 (A) and 08.07–23.08.10 (B) processed from the ALOS PALSAR data.

Colored areas represent movements of the ground surface: 1 – over -4.5 cm; 2 – from -4.5 to -3.0 cm; 3 – from -3.0 to -1.5 cm; 4 – from 1.5 to 3.0 cm; 5 – from 3.0 to 4.5 cm; 6 – over 4.5 cm. Minor changes (from -1.5 to -1.5 cm) are not highlighted in color. Negative values correspond to the ground surface subsidence. SRTM 90 is the background DEM. The inset shows disturbed areas in the vicinity of Vorkuta city (building plots and areas with disturbed vegetation), colored in pink. The values of local subsidence in the coal-mining areas (blue spots) accord with the legend.

Urals (watersheds of the Bolshaya Usa and Malaya Usa rivers). These sites are located on younger glacial moraine complexes of the Late Pleistocene (Khanmei) glaciation [Astakhov *et al.*, 2007; Astakhov, 2011]. The ground surface heave is visible most clearly on the 2010 images.

DISCUSSION

The DInSAR interferometry-derived seasonal vertical movements of the ground surface at the CALM R2 site and the adjacent area are represented by estimates similar to other parts of the Arctic. The subsidence of up to 2 cm was marked within 40 % of the tundra ecosystems in the Lena River delta with TerraSAR-X satellite for 2013–2014 [Antonova *et al.*, 2018]. The average values ranged from (1.7 ± 1.5) cm for the relatively cold 2013 to (4.8 ± 2.0) cm for the warm 2014. The magnitude of ground surface deformation measured with ERS 1/2 satellites for Alaska ecosystems (North Slope) ranged in 1–4 cm interval for summer periods of 1992–2000 [Liu *et al.*, 2010].

The amplitudes of soil surface displacement in the summer season were largely controlled by sediment composition, variations in ground ice content and sedimentary cover thickness according to the

measurements of satellite RADARSAT-2 of ecosystems of the Canadian Arctic Archipelago (Baffin Land) [Short *et al.*, 2014]. The minimum displacement (± 1 cm) was observed for bedrock outcrops and boulder clays [Rudy *et al.*, 2018]. The subsidence of sites with shallow bedrock occurrence demonstrated lower values despite the maximum subsidence features of adjacent areas for warmer summers. The seasonal and interannual low amplitude vertical surface movements with opposite directions were observed in northern Alaska during 1962–2015 [Streletskiy *et al.*, 2016].

Soil surface subsidence in the plain part of the study region at summertime is probably associated with the permafrost thaw. Surface subsidence of large magnitude was observed even in relatively cold years (2010) against the backdrop of higher precipitation.

Ground surface heave is not typical during the summer period, but occasionally was reported for the western foothills of the Polar Urals. This may be explained by increasing amount of summer liquid precipitation [Taskaev, 1997] in the area dominated by loamy gley soils [Shishov, 2000] which are prone to swelling. The heave motion of land-surface in the piedmont landscapes may have been also affected by ground water redistribution, slope processes, seasonal

ice aggradation at the end of vegetation period¹ [Rudy *et al.*, 2018] or a systematic error stemming from the DInSAR results calibration [Antonova *et al.*, 2018]. About 10–13 % of the alpine tundra of the south part of Melville Island (Canada) demonstrated heave of a ground surface (3.0–4.0 cm) in summers 2013 and 2015 according to the DInSAR measurements [Rudy *et al.*, 2018].

The highly mosaic tundra soil-vegetation cover hampers comparability of pointwise *in situ* and DInSAR measurements and obstructs for convergence assessment between them [Short *et al.*, 2011]. However, verification of DInSAR estimates by *in situ* data is a part of the accuracy assessment procedure. The increased number of instrumental measurements per observation site has contributed to improvement to the results agreement.

The highest agreement between the data was achieved for 2007 at the lower part of the hill with 7–8 instrumental measurements taken within one pixel.

CONCLUSIONS

A good agreement between the results of seasonal and interannual variability in ground surface displacements obtained by *in situ* and DInSAR measurements illustrate the effectiveness of the approach combining both field (instrumental) measurements and satellite observations to the studied permafrost-affected ecosystems. It is possible to reduce disagreement between the results obtained by different methods by larger amount of the *in situ* measurements within the same observation time intervals. To improve the accuracy of displacement estimates with remote satellite data, we need to increase the number of SAR images covering all observation periods.

The DInSAR methods allowed us to divide the CALM R2 monitoring site into two sectors (lower and upper parts of the sloping hill), thereby revealing differences in the ground surface elevation dynamics. Results of satellite and instrumental measurements were minimal in the lower part of the slope.

The opposite movements of soil surface during the summer season identified by the DInSAR method can be caused by landscape differences in the study region. Summer subsidence of ground surface (1.5–4.5 cm) was noted in plain tundra in loamy permafrost-affected soils. The ground surface heave (up to 2–3 cm) noted in the piedmont Polar Urals is associated with excess soil moisture in loamy gley soils in the context of enhanced summer precipitation and slope sediment redistribution. The specificity of weather conditions directly affects the ground surface movement in certain years. The amplitude of ground

surface subsidence in summer is generally lower in relatively warm and dry years and higher in cold and wet years.

Satellite imagery allows analyzing ground surface movements on a regional level due to large spatial coverage. By increasing the time coverage of imagery, we can better capture seasonal surface movements and minimize errors in their estimations. A time series of ground surface movements with account of meteorological and landscape parameters can be obtained even for remote and hard-to-reach areas. DInSAR is an actual data source for generating large-scale maps of the ground surface dynamics in permafrost regions.

Acknowledgements. *The research was conducted under the state task to the Institute of Biology of Komi Science Center of Ural Branch of the Russian Academy of Sciences “Revealing general patterns of formation and functioning of peat soils in the Arctic and Subarctic sectors of the European northeast of Russia” (grant AAAA-A17-117122290011-5) and the Circumpolar Active Layer Monitoring (CALM) program. ALOS PALSAR images were obtained under the JAXA RA-6 program (PI 3018).*

References

- Antonova, S., Sudhaus, H., Strozzi, T., *et al.*, 2018. Thaw subsidence of a yedoma landscape in Northern Siberia, measured *in situ* and estimated from TerraSAR-X interferometry. *Remote Sensing* 10 (4), No. 494, 1–27.
- Astakhov, V.I., 2011. The cover formation of the final Pleistocene in the far northeast of European Russia. *Regional Geology and Metallogeny*, No. 47, 12–27.
- Astakhov, V.I., Mangerud, Ya., Svendsen, J.I., 2007. Trans-Uralian correlation of the northern Upper Pleistocene. *Regional Geology and Metallogeny*, No. 30–31, 190–206.
- Baranov, Yu.B., Kiselevskii, E.V., Kantimirov, Yu.I., *et al.*, 2008. DEM Building based on the data derived due to the interferometric processing of ALOS PALSAR radar images. *Geomatics*, No. 1, 37–45.
- Bockheim, J., 2015. *Cryopedology*. Springer, Cham, New York, 177 pp.
- Brown, J., Hinkel, K.M., Nelson, F.E., 2000. The circumpolar active layer monitoring (CALM) program: research designs and initial results. *Polar Geography* 24 (3), 165–258.
- Chen, F., Lin, H., Zhou, W., *et al.*, 2013. Surface deformation detected by ALOS PALSAR small baseline SAR interferometry over permafrost environment of Beiluhe section, Tibet Plateau, China. *Remote Sensing of Environment* 138, 10–18.
- Chimitdorzhiev, T.N., Dagurov, P.N., Zakharov, A.I., *et al.*, 2013. Estimation of seasonal deformations of marshy soil by radar interferometry and geodetic leveling techniques. *Kriosfera Zemli [Earth’s Cryosphere]*, XVII (1), 80–87.
- Dobrovolsky, V.V., 2001. *Geology*. VLADOS, Moscow, 320 pp. (in Russian).

¹ Aggradation of ice does not occur late in the growing season. The mechanism for ice aggradation discussed in [Rudy *et al.*, 2018] is regarded as being a special case of a thaw slump, and is therefore possible only under extremely cold conditions (ground temperatures below –10 °C). – **Ed. note.**

- Druzhinina, O.A., Myalo, E.G., 1990. Protection of Vegetation of the Far North: Problems and Prospects. Agropromizdat, Moscow, 176 pp. (in Russian).
- Elsakov, V.V., 2012. Satellite remote sensing in the environmental monitoring of hydrocarbon production regions. *Current Problems in Remote Sensing of the Earth from Space*, 9 (5), 133–139.
- Elsakov, V.V., 2017. Spatial and interannual heterogeneity of changes in the vegetation cover of Eurasian tundra: Analysis of 2000–2016 MODIS data. *Current Problems in Remote Sensing of the Earth from Space*, 14 (6), 56–72.
- Eпов, M.I., Mironov, V.L., Chimitdorzhiev, T.N., et al., 2012. Observations of Earth's surface subsidence in the area of Kuzbass underground mines based on ALOS PALSAR radar interferometry data. *Earth Observation and Remote Sensing*, No. 4, 26–29.
- Ershov, E.D. (Ed.), 1996. Geocryological Map of the USSR, scale 1: 2 500 000. Gos. kartogr. fabrika, Vinnitsa, 16 pp. (in Russian).
- Evtuyushkin, A.V., Filatov, A.V., 2009. Estimation of Earth surface displacements in area of intensive oil production in Western Siberia by SAR interferometry using ENVISAT\ASAR and ALOS\ PALSAR data. *Current Problems in Remote Sensing of the Earth from Space*, 2 (6), 46–53.
- Geobotanical Zoning of the Non-Chernozem Zone of the European Part of the RSFSR, 1989. Nauka, Leningrad, 64 pp. (in Russian).
- Gorny, V.I., Kritsuk, S.G., Latypov, I.Sh., et al., 2010. Vertical sign-variable movements of ground surface according to satellite remote sensing data (on an example of Saint-Petersburg). *Current Problems in Remote Sensing of the Earth from Space*, 7 (2), 231–332.
- Kachurin, S.P., 1961. Thermokarst on USSR territory. *Izd. AN SSSR*, Moscow, 291 pp. (in Russian).
- Leshkevich, T.V. (Ed.), 2014. The Second Roshydromet Assessment Report on Climate Change and its Consequences in the Russian Federation. Rosgidromet, Moscow, 1009 pp. (in Russian).
- Liu, L., Tingjun, Zhang, T., Wahr, J., 2010. InSAR measurements of surface deformation over permafrost on the North Slope of Alaska. *J. Geophys. Res.* 115, 1–14.
- Mazhitova, G.G., 2008. Soil temperature regimes in the discontinuous permafrost zone in the East European Russian Arctic. *Eurasian Soil Science*, No. 1, 48–62.
- Mazhitova, G.G., Kaverin, D.A., 2007. Thaw depth dynamics and soil surface subsidence at a Circumpolar Active Layer Monitoring (CALM) site, the European North of Russia. *Kriosfera Zemli [Earth's Cryosphere]*, XI (4), 20–30.
- Musikhin, V.V., 2012. The interferometric SAR data processing-based monitoring of ground surface subsidence in areas under extensive mineral mining. Extended abstract of Cand. Sci. (Eng.) Dissertation. Perm, 22 pp. (in Russian).
- Romanovsky, V.E., Marchenko, S.S., Daanen, R.P., 2008. Soil climate and frost heave along the permafrost / Ecological North American Arctic Transect. In: Proc. of the Ninth International Conference on Permafrost (Fairbanks, Alaska, 28 June–3 July 2008). Institute of Northern Engineering, Univ. Alaska Fairbanks, Fairbanks, vol. 2, pp. 1519–1524.
- Rudy, A.C., Lamoureux, S.F., Treitz, P., et al., 2018. Seasonal and multi-year surface displacements measured by DInSAR in a High Arctic permafrost environment. *Intern. J. Appl. Earth Obs. Geoinformation* 64, 51–61.
- Shishkin, M.A., Malykh, O.N., Popov, P.E., Kolesnik, L.S., 2013. The State Geological Map of the Russian Federation, scale 1:200 000, Sheets: Q-41-V, VI (2nd ed.). VSEGEI, Moscow, 262 pp. (in Russian).
- Shishov, L.L. (Ed.), 2000. The State Soil Map of Russia, scale 1:1 000 000, Sheet: Q-41 Vorkuta]. FSGKR, Moscow (in Russian).
- Short, N., Brisco, B., Couture, N., et al., 2011. A comparison of TerraSAR-X, RADARSAT-2 and ALOS-PALSAR interferometry for monitoring permafrost environments, case study from Herschel Island, Canada. *Remote Sensing of Environment*, 115, 3491–3506.
- Short, N., LeBlanc, A.-M., Wendy, S.W., et al., 2014. RADARSAT-2 D-InSAR for ground displacement in permafrost terrain, validation from Iqaluit Airport, Baffin Island, Canada. *Remote Sensing of Environment*, 141, 40–51.
- Streletskiy, D.A., Shiklomanov, N., Jonathon, D., et al., 2016. Thaw subsidence in undisturbed tundra landscapes, Barrow, Alaska, 1962–2015. *Permafrost and Periglacial Processes* 28 (3), 566–572.
- Taskaev, A.I. (Ed.), 1997. Climate and Hydrology Atlas of the Komi Republic. Dik, Moscow, 115 pp. (in Russian).
URL: <http://www.glovis.usgs.gov> (last visited: 18.04.2018).
URL: [http://rp5.ru/Архив_погоды_в_Воркута_\(аэропорт\)](http://rp5.ru/Архив_погоды_в_Воркута_(аэропорт)) (last visited: 18.04.2018).
- URL: <http://www.meteo.ru> (last visited: 30.08.2019).
URL: <https://www.pgc.umn.edu/data/arcticdem> (last visited: 10.02.2020).

Received December 4, 2018

Revised August 22, 2019

Accepted May 28, 2021

Translated by N.N. Mzhelskaya

GROUND-PENETRATING RADAR SOUNDING OF DEPOSITS WITHIN THE LIMITS OF HIGH-CENTERED POLYGONS IN THE ARCTIC

D.E. Edemskiy¹, V.E. Tumskoy², A.N. Ovsyuchenko³

¹ Pushkov Institute of Terrestrial Magnetism, Ionosphere and Radio Wave Propagation, RAS, 4 Kaluzhskoe hwy, Troitsk, Moscow, 108840, Russia; deedemsky@gmail.com

² Melnikov Permafrost Institute, SB RAS, Merzlotnaya str. 36, Yakutsk, 677010, Russia

³ Schmidt Institute of Physics of the Earth, RAS, B. Gruzinskaya str. 10, bld. 1, Moscow, 123242, Russia

This article analyses the results of *Loza-V* georadar sounding of the upper part of the permanently frozen ground section in the area of polygonal patterns development. These investigations took place on the eastern coast of the Taymyr Peninsula and on the western coast of Kotelny Island (New Siberian Islands). The polygonal pattern is at the descend stage of development at both sites, so the ground-penetration radar profiles were scanned across the flat and high-centered central parts of the polygons. The results allowed us to determine some peculiarities of ground-penetrating radar profiles for polygons with different types of surfaces, composed mainly of sand-gravel deposits. Typical ground-penetrating radar complexes corresponding to the central parts of the polygons and deposits overlapping thawed ice wedges were identified. The possibility of using the spectrum of waveforms to interpret results was shown, velocities of electromagnetic wave propagation in the studied deposits were determined. Ice wedges and pseudomorphs after them were not reliably identified, but areas of their possible location were.

Keywords: ground-penetration radar, polygonal pattern, spectrum of waveforms, hodograph diagram, Taymyr Peninsula, Kotelny Island.

INTRODUCTION

In the area of the development of permafrost (the cryolithozone) polygonal forms of microrelief are widely distributed. They are known from the steppes of Zabaikalye in the south to the arctic deserts in the north, being most widely represented in zones from the forest tundra to arctic deserts. In the middle of the 20th century, it was already known that the reason for the formation of a polygonal patterned ground is the process of frost cracking [Dostovalov, 1952; Romanovskii, 1977]. As a result of temperature tensions during winter season narrow vertical cracks form in the top horizons of permafrost. Depending on environmental conditions they can fill with silty and sandy material, leading to the formation of primary-sand or sand-ice wedges, and in more humid conditions the cracks fill with snow meltwater and, with time, ice wedges are formed. During the long-term ice wedge growth, the ground rims, or ramparts, form on the surface of the earth above them. On the surface the ramparts above the ice wedges form a polygonal, most often a tetragonal, network. Water accumulates between the ramparts, and shallow center ponds form (Fig. 1, *a*). The ramparts vary from 0.1 to 0.5 m in height, the depth of the ponds usually constitutes 0.5–1.0 m. The diameter of the polygons changes from 3–5 to 100–150 m, usually within a range of 10–25 m.

When the active layer thickness increases as a result of grow of the mean annual ground surface temperature, the thawing of the top parts of the ice wedges begins, so that the polygonal surface evens out and becomes almost smooth. Upon further thawing, troughs form above the ice wedges, as a result of

which the initial low-centered ice-wedge polygons transform into a polygonal flat-centered (intermediate-centered) peatland with troughs above ice wedges, so the topography becomes inverse (Fig. 1, *b*). If ice wedge-containing deposits thaw more slowly but have a high ice content, cone-like mounds (thermokarst mounds, or baidzharakhs) with a height of 2–4 m appear between the thawing wedges (Fig. 1, *c*). As a result of total thawing of ice wedges, wedge-shaped or concaved thaw structures called pseudomorphs remain in their place in the outcrop around the perimeter of the polygons [Kaplina, Romanovskii, 1960].

The main features of a polygonal pattern are the polygons' configuration on the surface, their diameter, defined as the distance between the axes of parallel ice wedges, and the width of ice wedges. The solution of many scientific and practical problems requires knowledge of the composition of deposits and the peculiarities of the inner structure of the central parts of the polygons, which are usually called ground columns. These features can by far not always be quickly obtained using geological methods, so the more effective utilization of geophysical methods is of significant interest.

The ground-penetrating radar sounding method can be used to determine some features of a polygonal network (the peculiarities of its inner structure, the width of its ice wedges, the diameter of its polygons) and to more specifically define its areal distribution. The fields of application of GPR sounding are wide: geology, construction, archaeology, ecology, etc. [Finkelstein et al., 1986; Vladov, Starovoytov, 2004; Buzin

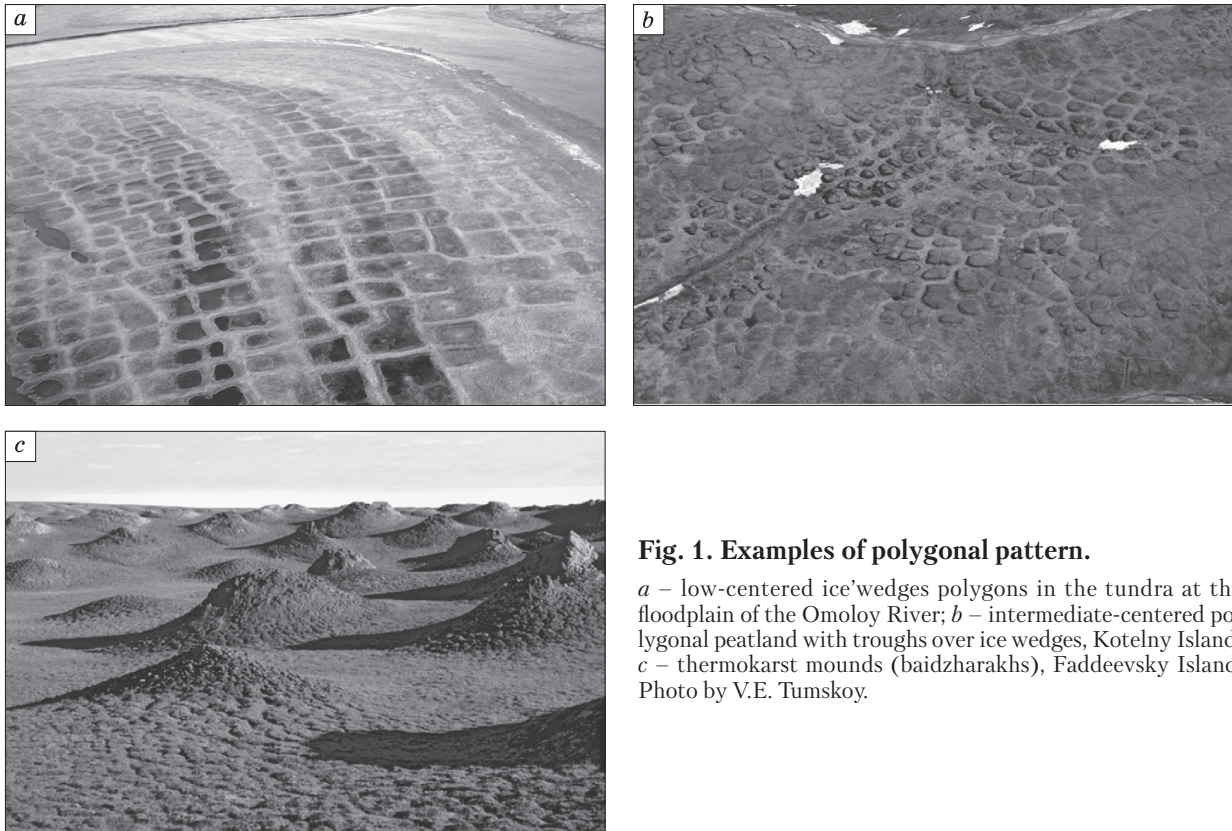


Fig. 1. Examples of polygonal pattern.

a – low-centered ice-wedges polygons in the tundra at the floodplain of the Omoloy River; *b* – intermediate-centered polygonal peatland with troughs over ice wedges, Kotelny Island; *c* – thermokarst mounds (baidzharakhs), Faddeevsky Island. Photo by V.E. Tumskoy.

et al., 2017; Edemskiy *et al.*, 2019]. In permafrost zone it is also widely used for the solution of geological-geophysical and engineering problems, as well as soil research [Voronin, 2015; Léger *et al.*, 2017; Sudakova *et al.*, 2017].

The article presents some results of studies of the structure of ground columns under the polygonal flat-centered peat mounds in the Arctic, which were obtained during the Complex Expedition of the Northern Fleet with the participation of the Russian Geographical Society “Franz Josef Land Archipelago – 2020” in August–October 2020.

EQUIPMENT AND METHODS OF FIELD WORK

The high-power *Loza-V* GPR [Kopeikin *et al.*, 1996; OOO “VNIISMI”, 2021], which has been used to solve various practical problems over the course of the past 10 years [Kopeikin *et al.*, 2012; Voronin, 2015; Edemskiy *et al.*, 2018, 2019], was used in this field research. As a result, tremendous positive experience both in conducting field work and in GPR data processing and interpretation techniques has been acquired.

The *Loza-V* GPR included transceiver antennas with a center frequency of 100 MHz (A100) and 150 MHz (A150), which provided an opportunity to

sound at a depth interval from several dozens of centimeters to 10–15 m, depending on the electromagnetic properties of the medium. GPR sounding was completed by the profile, with location registration at each scanning point, for which a Garmin CX60 GPS receiver was used.

To achieve correct interpretation of the obtained GPR profiles and for the reconstruction of the geological section based on these profiles the sounding was performed based on the common depth point (CDP) method with a subsequent (0.1 m interval) increase of the distance between the “transmitter – receiver” antennas from 0.2 m to 6 m [Vladov, Starovoytov, 2004; Edemskiy *et al.*, 2010]. This method allows for determining electromagnetic wave velocity in each layer of the GPR section and transforming the section from a scale of time to a scale of depth without using *a priori* information.

Standard processing modes were used to process data: appropriate values of increasing signal strength, brightness and contrast were chosen, bandpass filtering of signals and averaging functions were applied. On the final stage of processing and analysis a digital elevation model of the area was superimposed on the GPR profile.

Spectral analysis of GPR sounding results was applied during source data analysis. In accordance

with the theory of wave distribution [Finkelstein, 1986; Vladov, Starovoytov, 2004], the spectrum of the temporal signal form presents as a derivative of the spectrum of the source sounding signal and frequency characteristic of the media:

$$S(\omega) = S_0(\omega) \cdot K(\omega),$$

where $S(\omega)$ is the spectrum of the temporal signal form, $S_0(\omega)$ is the spectrum of the sounding signal, and $K(\omega)$ is the frequency characteristic of the media which presents as a characteristic of a filter of low frequencies, the parameters of which are determined by the properties of the media and are related to the structure of the section, the presence and properties of various reflecting boundaries and objects. Lately, the temporal spectral analysis was used to solve problems such as determining the percentage content of clay, mapping the soil moisture distribution, determining the boundaries of geological layers, ground ice conditions in permafrost, etc. [Benedetto, Tosti, 2013; Anbazhagan et al., 2014; Yongshuai et al., 2019; Neradovskii, Fedorova, 2020].

Because of a significant difference between the velocity of electromagnetic wave propagation in different layers of the GPR section and changing depths of layer boundary location along the profile, understanding GPR profile depth in terms of meters is very difficult. All GPR profiles are presented using axes: x – profile step, in meters, y – double wave travel time, in nanoseconds.

To interpret the obtained data we used descriptions of surface topography at research points and shallow (no deeper than 0.5 m) trial pits within the active layer for describing deposit composition.

RESULTS OF GROUND-PENETRATING RADAR SOUNDING OF DEPOSITS

GPR sounding of the central parts of polygons was conducted in two areas (Fig. 2). The first one is located on the western coast of Maria Pronchishcheva Bay at eastern Taymyr, the second one – on the sea coast southwest of Nerpalakh Laguna (Kotelny Island, New Siberian Islands archipelago). Quite severe permafrost conditions with a mean annual ground temperature of about -11 °C and ongoing thermal contraction cracking even in coarse grain deposits is typical for these areas. The thickness of the active layer rarely exceeds 0.5 m.

Maria Pronchishcheva Bay, eastern Taymyr

Maria Pronchishcheva Bay is located on the eastern coast of Taymyr Peninsula and is approximately 50 km long. From the southwest the bay is limited by the spurs of the Byrranga Mountains divided by river valleys. The rivers exit at foothill plain 0.5–2.5 km wide, forming a series of terraces. At the mountain edge where a young tectonic scarp and a series of low (up to 30 m) young anticline ridges stretch, the terraces decline to the level of the floodplain. From the west, the scarp and ridges limit the coastal lowland with numerous lagoons which fully flood during wind surges up to 1.5–2.0 m high. The study area was located near the mouth of the Yuzhnaya River (Fig. 3, a), the coordinates of the area are $75^{\circ}38'33.61''$ N, $112^{\circ}49'25.76''$ E.

The near-surface part of the section is composed of marine (alluvial-marine?) deposits, the thickness of which increases towards the coast of the bay from

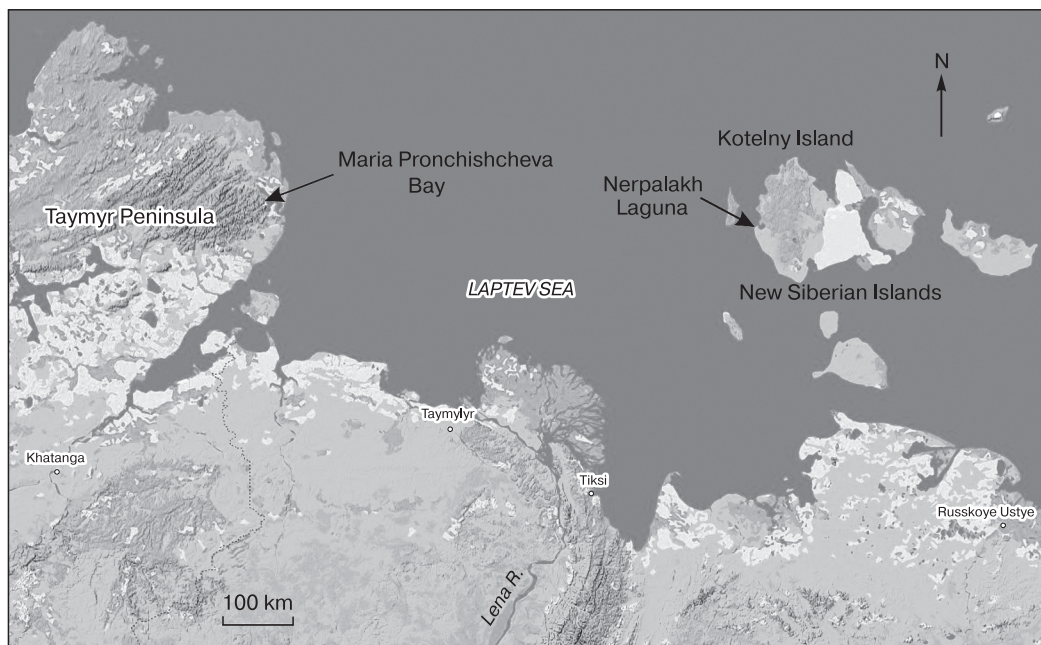


Fig. 2. Location of work sites.

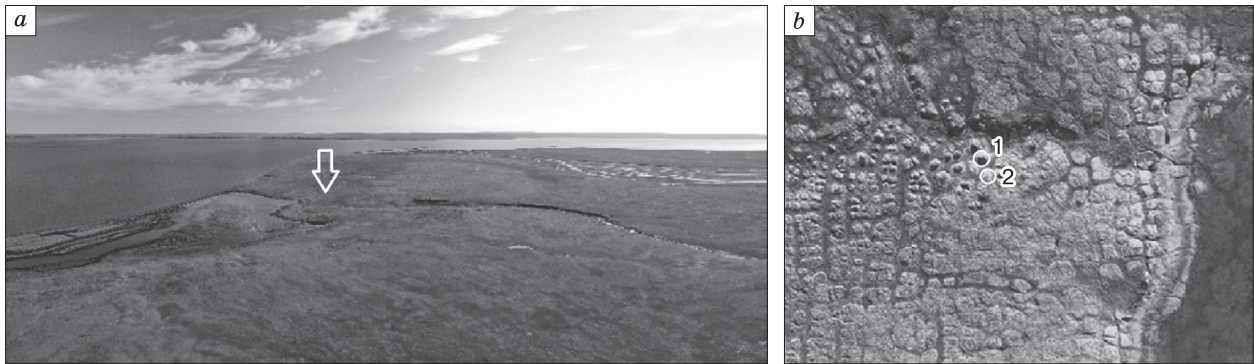


Fig. 3. Study site on the western coast of M. Pronchishcheva Bay.

a – general view of the bay coast (the arrow shows the position of sounding site); *b* – studied polygons (1 – high-centered, 2 – flat-centered). Photo by R.A. Zhostkov.

3 to 6–8 m. The deposits present as gravel-pebble material with interlayers of fine-grained sands and organogenic silts, the section of which is exposed in the bank outcrop of the stream. A peat layer covers the sand-gravel deposits, its thickness varies from 0.3 m to 0.5 m in its eastern part, where GPR sounding was completed.

A polygonal patterned ground, represented predominantly by flat polygons divided by troughs above the ice wedges, is widely distributed on the surface of the coastal plain (Fig. 3, *b*). The polygons have a tetragonal shape, most often square or rectangular. The diameter of the polygons is 12–15 m, less often up to 20 m, and increases to 50–60 m near the coastline on low-lying young terraces. All this indicates different ages and conditions of polygonal patterns formation in the lower reaches of the Yuzhnaya River. Almost all the polygons are divided into smaller ones by cracks of a higher generation. Near erosional downcuts filled with sandy-loamy deposits the flat-cen-

tered polygons transform into the high-centered ones owing to intense slumping of their slopes, resembling thermokarst mounds. Their height reaches 2 m, their diameter reaches 8 m. The depth of thaw was 0.45–0.50 m at the time of the studies.

Two polygons were studied during the course of the work – a high-centered (Fig. 4, *a*) and a flat-centered one (Fig. 4, *b*).

During the GPR sounding of the *high-centered polygon* two perpendicular profiles oriented south to north and east to west were drawn through it. The interval between the sounding points was 0.1 m. A100 antennas were used for layer-by-layer analysis of the top part of the section (TPS), and A150 with a higher resolution was used for detailed research. The obtained GPR profiles with topography taken into consideration are shown in Fig. 5.

During processing the GPR section was dissected into several GPR complexes (GC) [Vladov, Starovoytov, 2004] differing from one another in structure.



Fig. 4. Maria Pronchishcheva Bay.

Polygons: *a* – high-centered, *b* – flat-centered. Photo by D.E. Edemskiy.

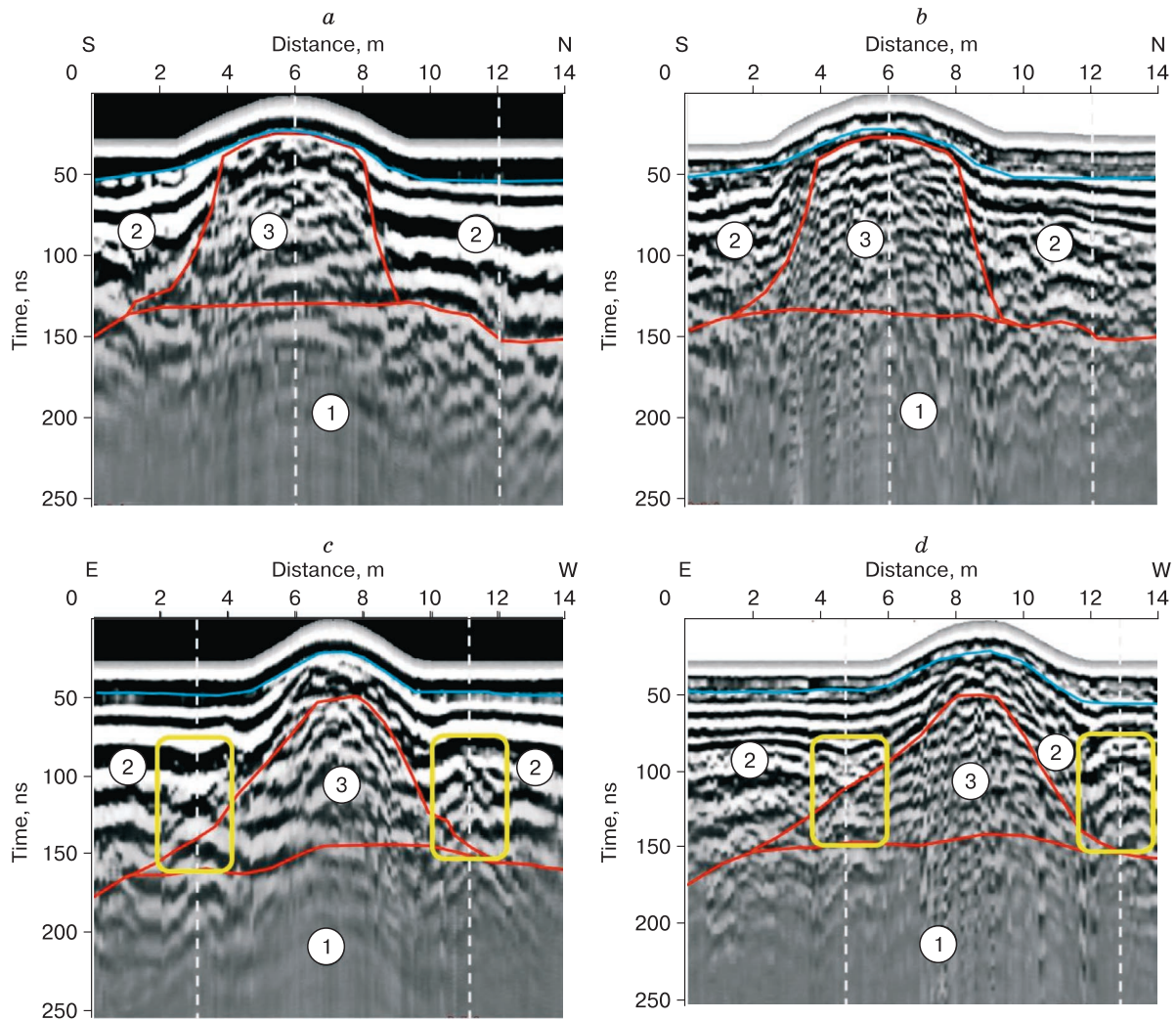


Fig. 5. Georadar profiles across a high-centered polygon.

a, b – meridional profile, A100 (*a*) and A150 (*b*) antennae; *c, d* – latitudinal profile, A100 (*c*) and A150 (*d*) antennas. 1–3 are the numbers of GPR complexes, the red lines show the boundaries between them, the blue line is the base of seasonally thawed layer. Heterogeneities are marked with yellow rectangles (see text).

The interfaces of the complexes are established based on intense reflecting horizons which match either layers of deposits of different composition or boundaries of unconformities.

The GPR complex GC1 is identified at the bottom of the studied part of the section, its top is located approximately at the 150 ns marks (4.5–5.5 m). GC3 matches the central part of the high-centered polygon (ground column) composed of sand-gravel deposits. A significant disturbance in phase axes before the 100–120 ns marks or approximately to depths of 3.0–4.4 m at an average electromagnetic wave velocity of 6.0–7.4 cm/ns is typical for GC3 (Table 1). GC2 matches troughs between the polygons. Its upper part (1.5–2.0 m thick) has a fairly clear parallel stratification along the whole length of

the profile. On the slopes of the high-centered polygon, near the contact point with GC3, it is significantly deformed and inclined with a shift in the spatial position of in phase axes, local change in the re-

Table 1. Results of processing of data collected using the common depth point method (M. Pronchishcheva Bay)

Layer	Time, ns	Layer bottom depth, m	Average velocity, cm/ns	Thickness, m	Velocity, cm/ns	Relative dielectric permittivity
1	22.7	0.54	4.78	0.54	4.78	53.91
2	72.2	2.71	7.50	2.17	8.80	11.62
3	91.2	4.44	9.74	1.73	18.2	2.72
4	116.2	6.08	10.48	1.64	13.2	5.17

flected waves and a damping of their amplitude. The geological section GC2 is represented by peat and peaty sands.

Figure 5, *c* shows that in the lower parts of GC3 on the eastern and western sides (3 and 11 m marks), local heterogeneities are seen with peaks at 75–80 ns, identified on the image using yellow rectangles. The heterogeneity on mark 11 presents as semi-parallel inclined reflections which match the heterogeneity of the vertical ice wedge [Elkarmoty et al., 2017]. Near the 5 m mark (Fig. 5, *d*), beginning at 75 ns, a V-shaped structure is formed with corresponding curves of in phase axes of lower layers to the 120 ns mark, which can be interpreted as an ice-wedge pseudo-morph.

During sounding of a polygonal patterns the primary reflection hyperbola which forms from the top of the wedge-shaped ice wedge, as well as the reflection from the bottom of the active layer, are usually difficult to distinguish on radargrams [De Pascale et al., 2007; Munroe et al., 2007]. This is related to their location at a small depth, where these signals are masked by the sounding impulse, air signals and are warped by reflections from near-surface layers and tears between blocks of the sod layer on the surface of the polygons.

Waveform spectrums obtained using the A100 antenna for the 6 m and 12 m marks (Fig. 5, *a, b*) are shown on Fig. 6, *a, b*. The amplitudes of the spectrum components for mark 6 in the center of the high-centered polygon are 25 % lower than the amplitudes for the 12 m mark, presumably owing to a disturbance of the surface layer by tears in sod. A change in the frequency of the spectrum of the received signal, seen in the appearance of two resonances at 85 and 102 MHz, should also be noted, which, together with the pattern of the reflected signal, can be interpreted as a result of a disturbance of the plane-layered media and the formation of randomly located reflection planes of distinct sizes.

During sounding of the *flat-centered polygon* similar GPR complexes were identified, but such significant changes are not seen in the reflection waveform. The subhorizontal structure in the near-surface layer GC2 is not disrupted overall up to 70–80 ns (Fig. 7). Nonetheless, changes are seen in both the near-surface layer (1.5–2.0 m thick) and in lower layers of sand-pebble deposits (GC1). There is no significant decrease in the signal level in the central part of the polygon at the 7 m mark also when analyzing the spectrum of the signal waveform (Fig. 8). The range of the high-frequency part of the spectrum for the central part of the polygon is limited by 80 MHz (Fig. 8, *a*) and 130 MHz (Fig. 8, *b*), while for the 12 m mark it is 130 MHz and 220 MHz, respectively. Apparently, this is result of structural changes in the upper layers (up to the mark near 65 ns) of the central part of the flat-centered polygon (GC3).

To determine the speed of electromagnetic wave propagation in the media and estimate the depth of GPR boundary location we used the CDP method with an interval of 0.1 m with a mutual relative antennas movement of a distance from 0.2 m to 6.0 m (Fig. 9). The GPR profile is drawn out three meters east of the high-centered polygon. The average electromagnetic wave propagation velocity has a general tendency to increase with depth from 4.78 cm/ns to 10.48 cm/ns and a respective change in dielectric permittivity from 53.91 to 2.72 (Table 1).

The obtained velocity propagation model consists of four layers. The top layer, up to 0.54 m thick and with an electromagnetic wave propagation velocity within the layer of $v = 4.78$ cm/ns, presents an active layer, while the lower layers present as layers of deposits of different granulometric compositions and, possibly, ice content, having electromagnetic wave propagation velocities in an interval of 8.8–18.2 cm/ns.

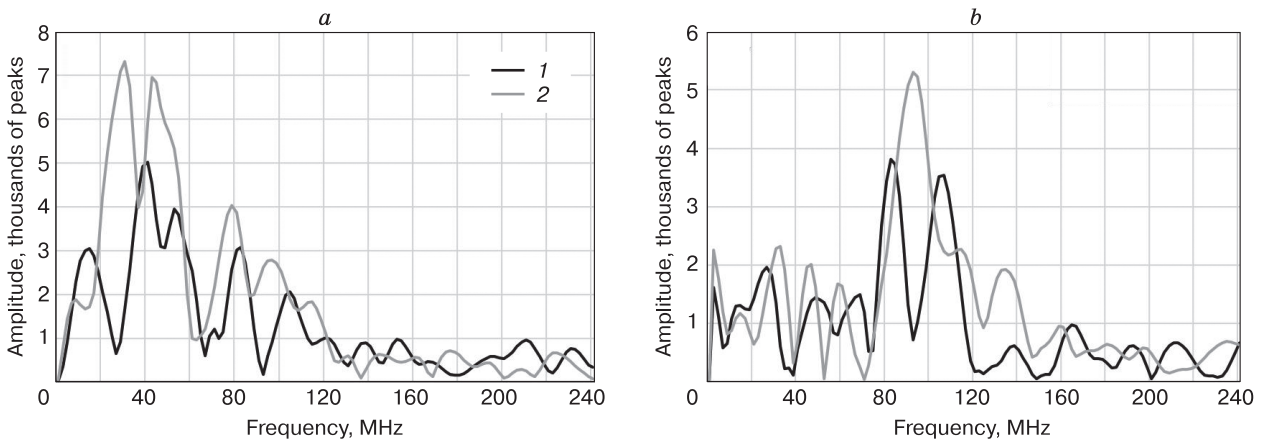


Fig. 6. Waveform spectrums for a high-centered polygon.

a – A100 antenna; *b* – A150 antenna; 1 – 6 m mark; 2 – 12 m mark. Position of marks see in Fig. 5, *a, b*.

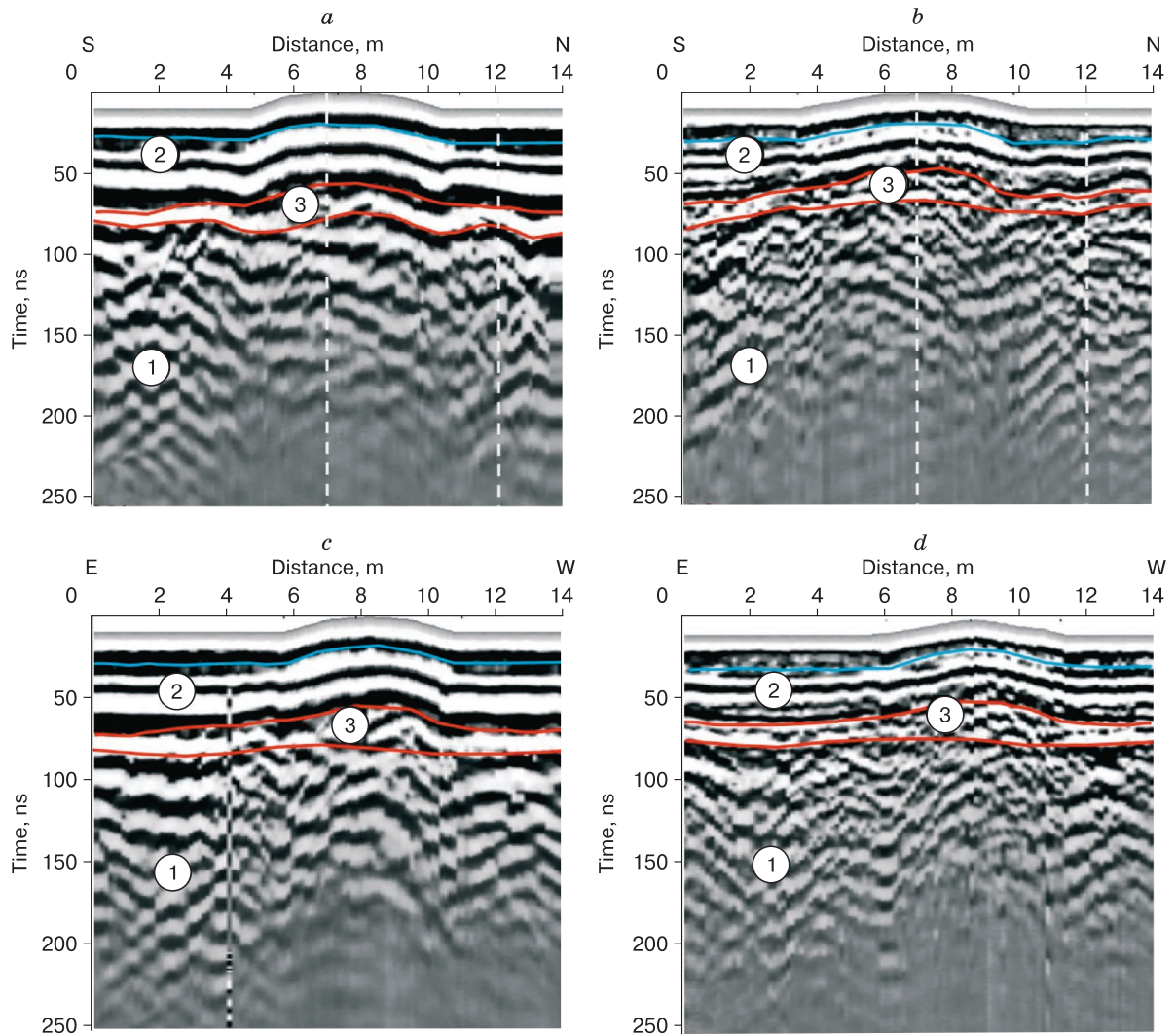


Fig. 7. Georadar profiles across a flat-centered polygon.

a, b – meridional profile, A100 (*a*) and A150 (*b*) antennas; *c, d* – latitudinal profile, A100 (*c*) and A150 (*d*) antennas. For other symbols see Fig. 5.

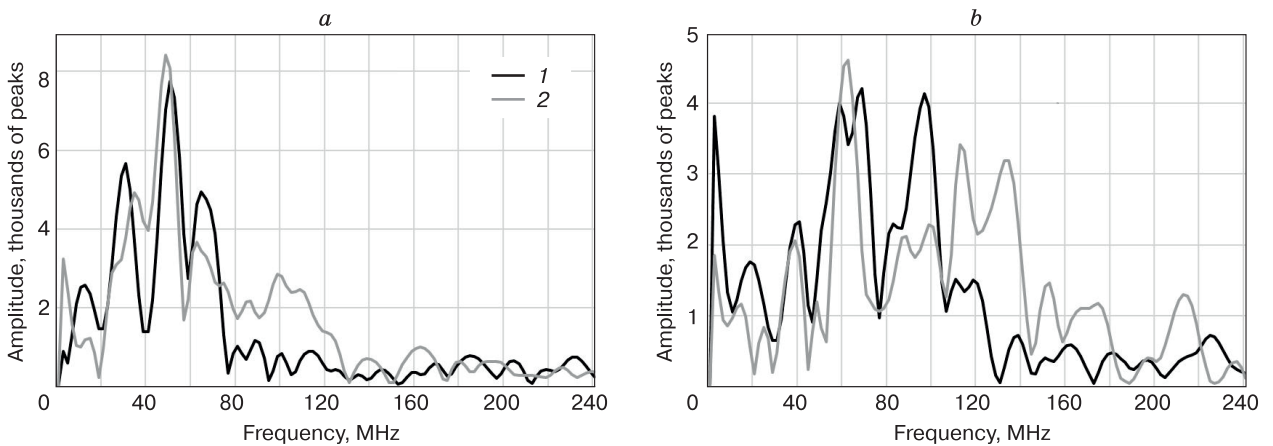


Fig. 8. Waveform spectrums for a flat-centered polygon.

a – A100 antenna; *b* – A150 antenna; 1 – 7 m mark; 2 – 12 m mark. Position of marks see in Fig. 7, *a, b*.

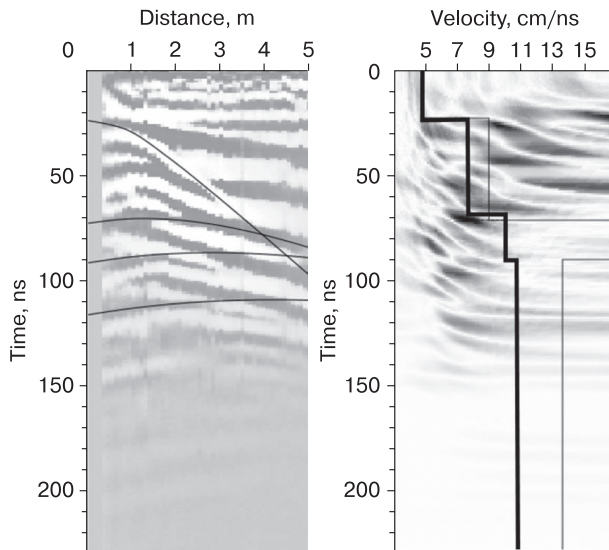


Fig. 9. The results of determining the speed of electromagnetic wave propagation (M. Pronchishcheva Bay).

Kotelny Island, Nerpalakh Laguna area

The second research area is located on the sea coast southwest of Nerpalakh Laguna ($75^{\circ}22'4.61''$ N, $137^{\circ}5'19.29''$ E). Here the coast forms a sheer cliff up to 25 m high in which layers of lithified Paleozoic carbonate-terrigenous sedimentary rocks are exposed. The surface of the high part of the coast is dissected by multiple hollows. Between and throughout them, a degrading polygonal network which forms low- and intermediate-centered polygons about 15–20 m large is distributed (Fig. 10). Morphologically they are in many ways similar to the polygons near M. Pronchishcheva Bay. The central part of the polygons is in many cases represented by flat-topped mounds up to 2 m high and up to 10 m in diameter. The vegetation is represented by moss and lichen, and by grasses at the tops and forms a thick sod cover which is ripped into separate blocks in most instances (Fig. 11).

In this site, the key point for the analysis of the structure is the depth of rock base. The rocks are represented by alternating layers of black carbonized schists, siltstone, fine grain sandstones and limestones which all have a dip of 45° with an inclination toward the northeast. At their top, in the bottom of disperse deposits cover, an eluvial horizon of varying thickness represented by debris of varied grain sizes is located.

As in the vicinity of M. Pronchishcheva Bay, two types of polygons can be identified here: high-centered polygons up to 2.0–2.5 m in height (Fig. 11, *a*) and flat-centered polygons up to 1 m high (Fig. 11, *b*). They are all 4 to 8 m in diameter and are located on a gentle slope descending towards the sea. The depth of thaw during the survey was 0.40–0.45 m.

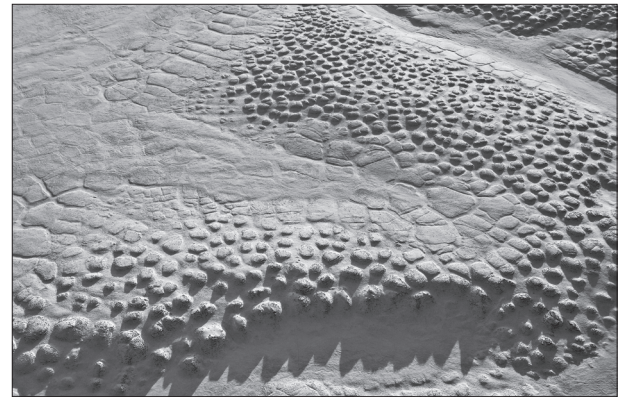


Fig. 10. Polygonal patterns in the research area southwest of Cape Walter, near the Nerpalakh Lagoon (Kotelny Island).

Photo by R.A. Zhostkov.

A GPR profile through a high-centered polygon about 2 m high and 6 m in diameter is presented in Fig. 12. Its surface is covered with separate sod hummocks, predominantly round, with a diameter of 30–40 cm and no taller than 10–15 cm. The measurements were obtained using an A150 antenna with the 15-cm interval along the profile.

Rock base GC1 is identified in the bottom of the GPR section. Its geological structure was studied in the coastal ledge up to 20 m high, located at a 150 m distance from the profile. The upper part of the GPR section (GC2), represented by peaty loamy sand deposits, has a rather clear subhorizontal stratification. It is most likely linked to the cover layer of disperse deposits 1.5–2.0 m thick. Between GC1 and GC2, the GC3 is identified based on different nature of the signal. We associate it with a layer of disperse deposits and products of rock base destruction, in other words, eluvium (GC3) up to 1 m thick.

Homogenous deposits are seen in the GPR profile in GC1 and GC2, and no signs of ice wedges or pseudomorphs are registered. The lower part of the GPR profile of the high-centered polygon is identified as an area with a low electromagnetic wave amplitude and a blurred wave patterns (area 4 on Fig. 12). Signal attenuation is apparently caused by scattering of the sounding signal in disperse deposits of GC3, which form the central part of the polygon.

The wave spectrum for the central part of the polygon (mark 11) has a smoother shape compared to the 4 m mark (Fig. 13). Additionally, the formation of a main spectral maximum at a frequency of 78 MHz and two with a lower amplitude at frequencies of 46 and 115 MHz are typical for it. This can be interpreted as a result of changes in the layered structure of disperse deposits cover (GC3) with a formation of



Fig. 11. Kotelny Island.

Polygons: *a* – high-centered, *b* – flat-centered. Photo by D.E. Edemskiy.

contrasting boundaries which contribute to the formation of spectral maxima at these frequencies.

The width of the signal spectrum at the 0.5 level of its maximum amplitude (mark 11) is more than two times less than that of mark 4 m, where frequencies from 90 to 170 MHz prevail. This may be related to weakening of the sounding signal in GC2 and GC3 and a smaller contribution of signals reflected from heterogeneities in the rock base to the resulting spectrum (GC1).

A GPR profile drawn through two high-centered polygons 0.8 and 1.2 m high, 4 and 6 m in diameter, respectively, is presented in Fig. 14. The polygons are located on a gentle northeastern slope of the upland. As in the previous example, GC1 composes a rock

base with an eluvial horizon on top (GC3). The upper part of GPR section GC2 has a fairly clear subhorizontal layering.

Signals are registered in Fig. 14 within GC3 (radiolocational images of local objects) which may be large fragments of underlying bedrock. The presence of these heterogeneities leads to additional signal attenuation, as a result of which areas with lower wave amplitude (area 4 on Fig. 14) and significant weakening of equiphasic lines in GC1 form on the profile. The area of signal attenuation captures not the entire area of the polygon, but only a part of it, under local heterogeneities.

Among the spectra demonstrated in Fig. 15 it can be seen that the main maxima for two marks

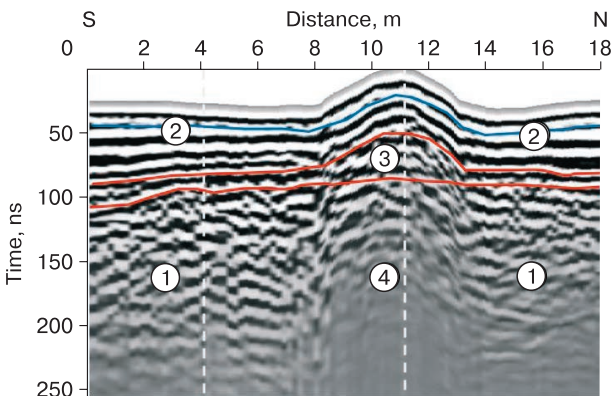


Fig. 12. Georadar profile across a high-centered polygon, A150 antenna.

1–3 – numbers of GPR complexes, 4 – area of signal attenuation. The red lines show the boundaries between the GPR complexes, the blue line is the bottom of the seasonally thawed layer, the white dashed lines are the marks for which the spectral analysis was carried out.

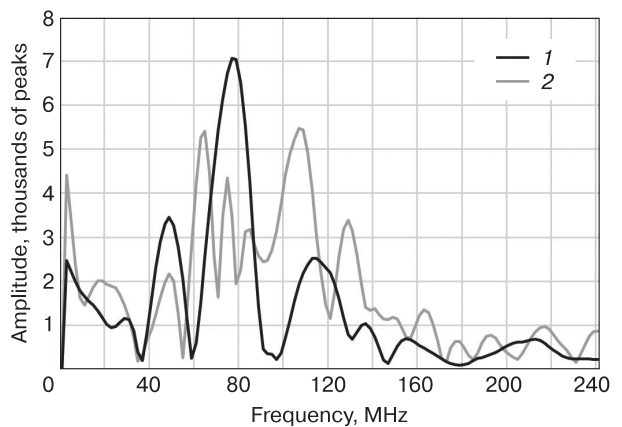


Fig. 13. Waveform spectrums for a high-centered polygon, A150 antenna.

1 – 4 m mark; 2 – 11 m mark. Position of marks see in Fig. 12.

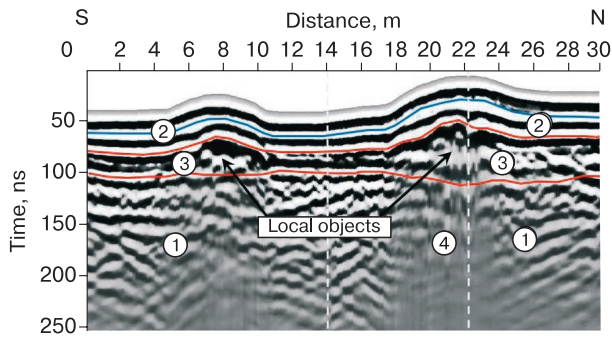


Fig. 14. Georadar profile across two high-centered polygons, A100 antenna.

For symbols see Fig. 12.

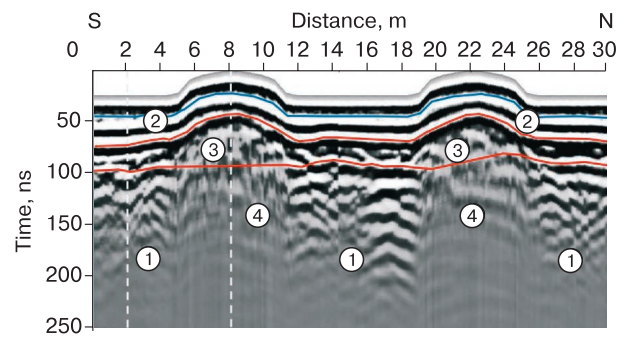


Fig. 16. Georadar profile across two flat-centered polygons, A100 antenna.

For symbols see Fig. 12.

(14 m and 22 m) are located at 60 MHz, however, the amplitude of the spectral component is 38 % lower for the central part of the polygon than for the 14 m mark, which is supposedly caused by structural peculiarities of GC3, positioned between the bottom of the subhorizontal sedimentary deposits and the top of the bedrock. Damping of the amplitude of the spectral component and the formation of a smoother spectrum shape may indicate a propagation process of the signal in GC3, which can also be interpreted as a change in the structure of the top layers of the section and the appearance of new boundaries or interlayers up to approximately 100 ns marks in the central part of the high-centered polygon [Schennen et al., 2016].

Further down the slope, towards the coast, the relative height of the polygons decreases to 1 m, and their surface becomes more flat and less destroyed. Figure 16 shows a GPR profile drawn through two flat-centered polygons 7 and 8 m in diameter and 1.0–1.1 m high.

Overall, the GPR profile structure is identical to the previous ones (Figs. 12, 14). The thickness of the active layer is 0.40–0.45 m (measured by a dipstick), the water content of the deposits in the active layer is uneven. The top horizon of disperse deposits (GC2) forms a specific structure with parallel subhorizontal stratification, the thickness of which is comparable to the analogous GC on Fig. 12 and 14. The bottom of GC2 in the body of the flat-centered polygon is located at the 50–65 ns mark (1.5–2.0 m at an average electromagnetic wave velocity of 6 cm/ns). The body of the polygon is identified on the profile as an area with significant amplitude attenuation of the sounding signal (GC4) and, as a result, an absence of in phase components in lower layers of the profile.

In the spectral region (Fig. 17) the left polygon differs from the previously discussed one in its shift into the low-frequency region of the spectrum maximum for a 50 MHz interpolygonal trough, which is possibly related to the bedrock structure of the GC1.

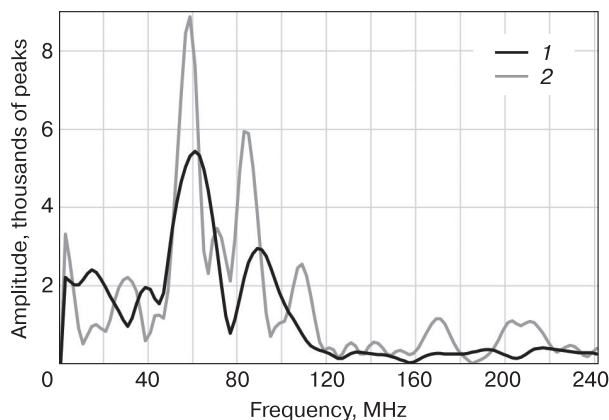


Fig. 15. Waveform spectrums for a high-centered polygon, A100 antenna.

1 – 14 m mark; 2 – 22 m mark. Position of marks see in Fig. 14.

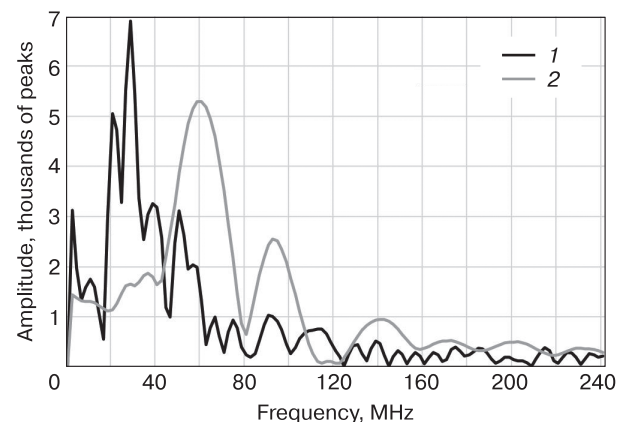


Fig. 17. Waveform spectrums for a flat-centered polygon, A100 antenna.

1 – 2 m mark; 2 – 8 m mark. Position of marks see in Fig. 16.

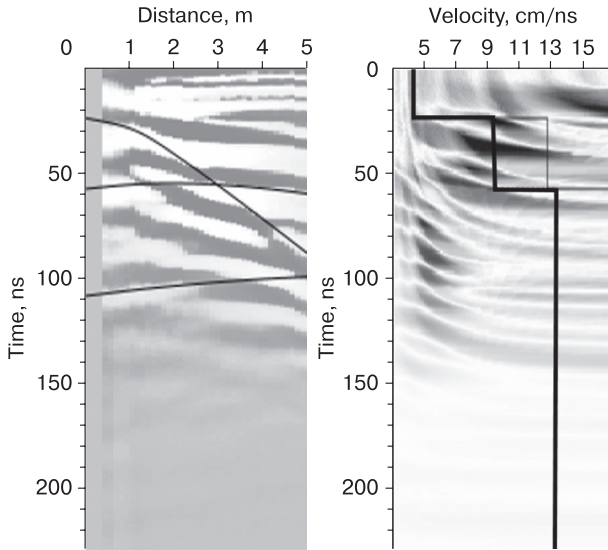


Fig. 18. The results of determining the speed of electromagnetic wave propagation (Kotelny Island).

Table 2. Results of processing of data collected using the common depth point method (Kotelny Island)

Layer	Time, ns	Layer bottom depth, m	Average velocity, cm/ns	Thickness, m	Velocity, cm/ns	Relative dielectric permittivity
1	23.6	0.50	4.26	0.50	4.26	49.76
2	58.1	2.65	9.14	2.15	12.4	5.85
3	109.8	7.06	12.83	4.41	17.0	3.11

ing the CDP method with an interval of 0.1 m and a distance from 0.2 m to 4.6 m between antennae (Fig. 18). The CDP profile is located in close proximity to the high-centered polygon. According to sounding data, electromagnetic wave propagation velocity increases with depth from 4.26 cm/ns to 12.83 cm/ns, and dielectric permittivity increases from 49.76 to 3.11 (Table 2).

The obtained model of propagation velocity consists of three layers. The top layer up to the 23.6 ns mark and with an electromagnetic wave propagation velocity of 4.26 cm/ns presents an active layer 0.5 m thick. The lower layers are deposits of different granulometric composition and, possibly, ice content, having a wave propagation velocity in the range of 9.14–12.83 cm/ns.

DISCUSSION

All the studied polygons, both in Maria Pronchishcheva Bay and on the western coast of Kotelny Island, were formed during a process of long-term frost cracking and the formation of ice wedges. Similarity in the deposits in which they formed is typical for them: in all cases they were developed in relatively coarse deposits represented by sands and sands

The spectrum for the central part of the polygon (8 m mark) is almost identical in its parameters (central frequency, amplitude) to the spectrum for the polygon in Fig. 14. The smoothed shape of the signal spectrum and almost total absence of signals from the bedrock (GC1) may indicate only a scatter process in GC3, between the bottom of the disperse deposits horizon and the top of the bedrock. The nature of the changes and the reasons leading to them require additional research and interpretation.

To determine the velocity of the sounding impulse propagation and to estimate the depths of separate layers of the section, studies were completed us-

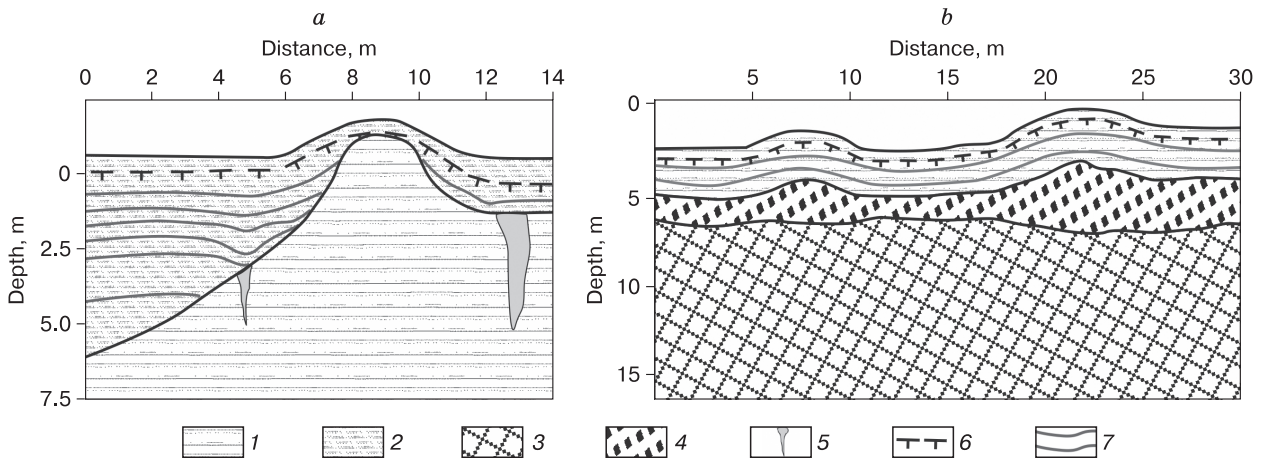


Fig. 19. Geological sections built based on the interpretation of typical GPR profiles.

a – the profile across the high-centered polygon in the M. Pronchishcheva Bay (see Fig. 5, *d*); *b* – the profile across two high-centered polygons at Kotelny Island (see Fig. 14). 1 – sand and gravel deposits; 2 – sandy and sandy loamy deposits, varying in peat amount; 3 – bedrock; 4 – eluvium with fragments of bedrock; 5 – ice wedges; 6 – seasonally thawed layer base; 7 – layering in disperse deposits.

with gravel, overlapped by peaty deposits or peat. Currently the polygonal pattern is in a stage of degradation in both regions: the ice wedges are partially or totally thawed, depressions have formed above them and ground columns have transformed into high or flat-topped mounds. Owing to solifluction processes on their slopes, these mounds gradually decrease in diameter and height, the width of the troughs between them increases. Thawed material moves into the troughs between the mounds and then slowly travels down the slope, forming a thin cover of deluvial-solifluctional deposits with parallel layering in troughs above what was previously ice wedges. The supposed geological sections of the deposits constructed from the results of GPR studies of two typical profiles are shown in Fig. 19.

GPR studies did not show a presence of ice wedges in depressions, with the exception of one area near a high-centered polygon in M. Pronchishcheva Bay (Fig. 5). Ice wedges either melted completely or were preserved as a thin lower part which does not get registered by the GPR. Deluvial-solifluctional deposits lie more or less parallel to the surface. At their base, structures resembling pseudomorphs are found only in M. Pronchishcheva Bay. Most likely, the ice wedges on Kotelny Island penetrated into relatively coarse bedrock eluvium, which does not cause significant subsidence when thawing.

In all cases the inner structure of the polygons showed the presence of heterogeneities most likely related to ground ice content distribution. For GPR profiles in M. Pronchishcheva Bay weak signal attenuation and general conformity of the radargram to the topography are typical: within the more high-centered mound a larger rise in in-phase lines is seen compared to the flat-centered polygon. On Kotelny Island the situation is similar, but here the peculiarities of the structure of the eluvial horizon on the boundary of bedrock and disperse deposits apparently play an important role.

RESULTS

Georadiolocational research of a polygonal pattern at the degradation stage, which exists in modern severe permafrost conditions, was conducted on the eastern coast of Taymyr Peninsula and on the western coast of Kotelny Island. As a result of thawing of the polygonal surface, the ground columns are represented by slightly high-centered or flat-centered forms. They are composed predominantly of sandy material.

The results of the studies allowed us to see the inner structure of the high-centered polygon, its boundaries, to establish an almost total degradation of ice wedges and the possible presence of pseudomorphs in the M. Pronchishcheva Bay area. A poor expression of the pseudomorphs is attributed to the deposit composition (frost-stable sands) and the close proximity of the bedrock on Kotelny Island.

In the present work a method based on joint frequency-time analysis of GPR data was used for a more precise qualitative estimate of changes occurring in the geological media. It was shown that the peak part of the spectrum is unique in different conditions and for different structural changes in frozen ground horizons, which indicates an ability of spectral analysis for the differentiation of heterogeneities under the polygonal patterns.

According to sounding data based on the CDP method, the electromagnetic wave propagation velocity in the section increases with depth from 4.26 cm/ns to 18.2 cm/ns, and dielectric permittivity changes within the range from 53.91 to 2.72.

Overall, the conducted GPR sounding of several polygons in similar geocryological conditions raised more questions than provided answers.

GPR should be considered among the main tools for permafrost studies. Compared to other geological and geophysical methods, GPR allows to determine in detail the inner structure of an object, the shape of geological boundaries, the structure of a section. Further field work in areas with different permafrost structure and polygonal patterns is necessary for verification of the results of GPR sounding.

Acknowledgments. *The authors thank the Russian Geographical Society for assistance in the organization and completion of this research.*

References

- Anbazhagan, P., Chandran, D., Burman, S., 2014. Subsurface imaging and interpretation using Ground Penetrating Radar (GPR) and Fast Fourier Transformation (FFT). *Advances in Soil Mechanics and Geotechnical Engineering*, vol. 3, 254–259.
- Benedetto, F., Tosti, F., 2013. GPR spectral analysis for clay content evaluation by the frequency shift method. *J. Appl. Geophys.*, No. 97, 89–96.
- Buzin, V., Edemskiy, D., Gudoshnikov, S., et al., 2017. Search for Chelyabinsk meteorite fragments in Chebarkul Lake bottom (GPR and Magnetic Data). *J. Telecommun. and Information Technol.*, No. 21, 69–78.
- De Pascale, G.P., Pollard, W.H., Williams, K.K., 2007. Geophysical mapping of ground ice using a combination of capacitive coupled resistivity and ground-penetrating radar, Northwest Territories, Canada. *J. Geophys. Res.* 113 (2), F02S90.
- Dostovalov, B.N., 1952. On the physical conditions for the formation of frost cracks and the development of fissured ice in disperse rocks. *Issledovaniya vechnoy merzloty v Yakutskoy respublike* [Permafrost Investigations in Republic of Yakutia], iss. 3, 162–194 (in Russian).
- Edemskiy, D.E., Edemskiy, F.D., Morozov, P.A., 2010. Profiling and determination of media parameters during GPR surveys. *Elektromagnitnye volny i elektronnye sistemy* [Electromagnetic Waves and Electronic Systems], 15 (9), 57–63 (in Russian).
- Edemskiy, D.E., Popov, A.V., Prokopovich, I.V., et al., 2018. Ground penetrating radars application for soil-pyroclastic cover survey of the south-eastern zone of Matua Island, the

- Kurile Islands. Vestnik Kamchatskoy regional'noy assotsiatsii "Uchebno-nauchnyy tsentr". Seriya: Nauki o Zemle [Bulletin of Kamchatka Regional Association "Educational-Scientific Center". Earth Sciences], iss. 40 (4), 69–81 (in Russian).
- Edemskiy, D.E., Popov, A.V., Prokopovich, I.V., et al., 2019. Application of geophysical methods in the survey of the periphery of the Tunnug-1 mound. Intern. J. Appl. and Basic Res., No. 11, 40–48.
- Elkarmoty, M., Colla, C., Gabrielli, E., et al., 2017. Mapping and modelling fractures using ground-penetrating radar for ornamental stone assessment and recovery optimization: Two case studies. The Mining-Geology-Petroleum Engineering Bulletin, 32 (4), 63–76.
- Finkelstein, M.I., Kutev, V.A., Zolotarev, V.P., 1986. Application of Radar Subsurface Sounding in Engineering Geology. Nedra, Moscow, 128 pp. (in Russian).
- Kaplina, T.N., Romanovskii, N.N., 1960. About ice-wedge casts. In: Periglacial Forms on the USSR Territory. Moscow, pp. 47–59 (in Russian).
- Kopeikin, V.V., Edemskiy, D.E., Garbatsevich, V.A., et al., 1996. Enhanced power ground penetrating radars. In: Proc. of the 14th Intern. Conference on Ground Penetrating Radar, Sendai, Japan, pp. 152–154.
- Kopeikin, V.V., Morozov, P.A., Edemskiy, F.D., Edemskiy, D.E., et al., 2012. Experience of GPR application in oil-and-gas industry. In: Proc. of the 14th International Conference on Ground Penetrating Radar, Shanghai, China, vol. 3, pp. 817–819.
- Léger, E., Dafflon, B., Soom, F., et al., 2017. Quantification of Arctic soil and permafrost properties using ground-penetrating radar and electrical resistivity tomography datasets. In: IEEE J. Selected Topics in Appl. Earth Observations and Remote Sens., No. 10, 4348–4359.
- Munroe, J.S., Doolittle, J.A., Kanevskiy, M.Z., et al., 2007. Application of ground-penetrating radar imagery for three-dimensional visualization of near-surface structures in ice-rich permafrost, Barrow, Alaska. Permafrost and Periglacial Processes 18, 309–321.
- Neradovskii, L.G., Fedorova, L.L., 2020. Experience in studying the nature of the periodicity of GPR signals using spectral analysis methods. Uspekhi sovremennogo estestvoznaniya [Advances in Modern Natural Science], No. 6, 95–106 (in Russian).
- OOO "VNIISMI Company" [Web]. – URL: <http://www.georadar.ru/> (last visited: 05.03.2021) (Russian and English).
- Romanovskii, N.N., 1977. Formation of Polygonal-wedge Structures. Nauka, Novosibirsk, 1977, 213 pp. (in Russian).
- Schennen, S., Tronicke, J., Wetterich, S., et al., 2016. 3D ground-penetrating radar imaging of ice complex deposits in northern East Siberia. Geophysics 81 (1), wa185–wa192.
- Sudakova, M.S., Sadurtdinov, M.R., Malkova, G.V., Skvortsov, A.G., Tsarev, A.M., 2017. Ground penetrating radar applications to permafrost investigations. Earth's Cryosphere XXI (3), 62–74.
- Vladov, M.L., Starovoytov, A.V., 2004. Introduction to Ground Penetrating Radar. Izd-vo MGU, Moscow, 2004, 153 pp. (in Russian).
- Voronin, A.Ya., 2015. Criteria for identifying the structure and functional properties of the soil profile in GPR studies using the "LOZA-V" GPR. In: Byulleten Pochvennogo instituta im. V.V. Dokuchaeva [Dokuchaev Soil Bulletin], No. 80, pp. 106–128 (in Russian).
- Yongshuai, Y., Yajing, Y., Guizhang, Z., 2019. Estimation of sand water content using GPR combined time-frequency analysis in the Ordos Basin, China. Open Physics 17, 999–1007.

Received March 29, 2021

Revised April 15, 2021

Accepted June 1, 2021

Translated by M.A. Korkka